Studying Young Massive Clusters using High-Resolution Wide-Field Imaging

A DISSERTATION SUBMITTED TO THE GRADUATE DIVISION OF THE UNIVERSITY OF HAWAIʻI IN PARTIAL FULFILLMENT OF THE REQUIREMENTS FOR THE DEGREE OF

DOCTOR OF PHILOSOPHY

IN

ASTRONOMY

Dec 2019

By
Maxwell Service

Dissertation Committee:

M. Chun, Chairperson
J.R. Lu, Chairperson
C. Baranec
S. Bussinger
E. Magnier
B. Reipurth

# Abstract

The aim of this thesis was to advance the instrumentation and techniques necessary to study Young Massive Clusters. These clusters offer ideal laboratories for the study of star formation as they contain a single metalicity, single age population that is well sampled across the entire stellar mass range. These objects are generally highly obscured by dust, are extended on the sky and contain dense stellar cores where observations are limited by crowding. Infrared, wide-field high-resolution imaging capability with ground layer adaptive optics can address all of those concerns. Proper motions determined from precision astrometry can be used to separate cluster sources form contaminating objects using proper motions. Infrared imaging mitigates the effects of extinction and wide field imaging allows programs to be carried out efficiently.

This thesis summarizes progress towards this goal along a few avenues. First, analysis techniques are developed and applied to existing archival data of the cluster Westerlund 2 to evaluate kinematic cluster membership and measure the kinematic substructure of the cluster. Second, work on accurately calibrating optical distortion in order to enable precise astrometric measurements for existing systems is presented. Finally, work on the integration and commissioning of the GLAO pathfinder instrument 'imaka are presented as progress towards demonstrating accurate astrometric measurements over $\sim$ 18 arcminute fields of view at Maunakea.

## 0.1 Introduction

Many science cases uniquely benefit from wide-field high-resolution imaging. One important one is the study of Young Massive Clusters (age $< 5$ Myr amd mass $> 10^4$ $M_\odot$). These cluster offer the unique opportunity to study star formation in its natural environment, particularly for measurements of the initial mass function for rare high mass stars. The structure and dynamics in clusters at these young ages constrain the models for the initial cluster formation.

Detailed measurements of cluster properties requires accurate selection of cluster members from field stars. This is particularly critical for young massive clusters which are located in the galactic plane which can have a large number of contaminants depending on the geometry. An ideal method for selecting cluster members is based on the common motions of the stars, as the cluster stars will be moving with a common speed which does not match the foreground or background sources. Proper motion studies are well suited for this work, as they can reach the desired depth to measure both the low mass and high mass cluster sources for the entire field (e.g. Anderson et al. 2008; Stolte et al. 2008; Hosek et al. 2015). This approach requires high resolution imaging to combat crowding and sufficient field of view to efficiently image the cluster. Current experiments have used Hubble Space Telescope imaging which has a field of view of $160'' \times 160''$, however some interesting clusters are too large to be efficiently imaged with this system, for example, the Red Super Giant Clusters have diameters that are $> 6$ arcminutes. An instrument with a larger field of view opens up more potential targets and the fact that these young massive clusters typically have large extinction makes IR imaging more desirable.

This work focuses on demonstrating the power of ground layer adaptive optics (GLAO) as a way to address this science case in future instrumentation. GLAO is designed to take advantage of the the fact that the lowest layers of the atmosphere can contribute as much as 70% of the total turbulence power at sites like Maunakea (Chun et al. 2009, 2014). As these layers are close to the ground, their distortion is common to a larger viewing angle,

so if a system only corrects these distortions it can deliver a much larger corrected field as compared to traditional single beacon, single conjugate AO systems. Its worth noting that the actual relative strength of the ground layer to the rest of the atmosphere depends sensitively on both the site and telescope, as dome seeing can be a large contribution. One way to view these systems is as a way to improve the seeing quality , where poor seeing conditions are transformed into median nights and median nights become excellent nights. This delivered image quality provides a large enough field of view to efficiently image clusters which can be several arcminutes on the sky (e.g. Red Super Giant Clusters) while still providing high resolution imaging to mitigate crowding in the dense central regions. Additionally, GLAO systems will provide excellent correction in the near-infrared which is useful for overcoming the large differential extinction due to dust and gas in these young clusters. Another advanced adaptive optics technique which could address these issues is multi-conjugate adaptive optics. These systems work similarly to GLAO systems in the sense that they measure the input wavefront along multiple lines of sight, however, instead of simply correcting the lowest atmospheric layers using a single correcting element MCAO system reconstruct the turbulence profile and apply a correction using multiple corrective elements (deformable mirrors) conjugated to different heights. The Gemini South telescope has demonstrated this technique over an $85'' \times 85''$ field of view (Rigaut et al. 2014; Neichel et al. 2014). This type of system offers performance improvements over a GLAO system at the cost of greater complexity and a smaller field of view. We chose to focus on GLAO technology advancement in order to access the widest fields of view an to demonstrate the gains for a simpler approach.

Uncorrected systematic errors in astrometric measurements are much larger than the random errors sources. Larger fields of views immediately help one problem, which is the number of reference sources. Reference sources are used to account for the distortion variation between between individual frames, so more reference sources allow for a more accurate higher order correction of those changes. Optical Distortion calibration is critical generally, as it the static component is often >1000 times larger than the required

precision.for high precision applications. Aside from calibrating the static component, the variable distortion component also has to be calibrated as it can contribute significantly to the measurement errors (Neichel et al. 2014). The degree of this issue varies based on the specifics of the design, for example, the NIRC2 camera which is mounted on a Nasymyth platform experiences no measurable distortion variation (Service et al. 2016), while GSAOI which is mounted at a Cassegrain focus experiences significant variation on short time scales (Neichel et al. 2014).

In a practical sense, this means that distortion calibration is essential for astrometric science cases of any imaging system. In the context of larger fields, this is further exacerbated by design considerations in the optics of an AO relay. In any optical design, there are tradeoffs between many considerations including complexity, field of view and amount of optical geometric distortion. In the past, these tradeoffs have led to accepting high levels of geometric optical distortion (1-2%) to optimize the image quality across a larger field view, as compared to traditional SCAO instruments with their 10-30 arcsecond fields of view. The results of these decisions is that even though ground based wide field AO technologies are ideally suited for studying young massive clusters, it is absolutely necessary that these instruments calibrate the complete optical distortion (both static and variable). This thesis presents a combination of work which has made progress towards enabling YMC science using future GLAO instrumentation. There are three distinct parts of this effort: (1) commissioning of the 'imaka pathfinder instrument to demonstrate GLAO at Maunakea, (2) demonstration of optical distortion calibration techniques, and (3) analysis of Westerlund 2 to demonstrate an example of a specific case of the type of science one could accomplish utilizing a future GLAO system.

# References


Anderson, J., Sarajedini, A., Bedin, L. R., King, I. R., Piotto, G., Reid, I. N., Siegel, M., Majewski, S. R., Paust, N. E. Q., Aparicio, A., Milone, A. P., Chaboyer, B., & Rosenberg, A. 2008, AJ, 135, 2055

Chun, M., Wilson, R., Avila, R., Butterley, T., Aviles, J.-L., Wier, D., & Benigni, S. 2009, MNRAS, 394, 1121

Chun, M. R., Lai, O., Toomey, D., Lu, J. R., Baranec, C., Thibault, S., Brousseau, D., Zhang, H., Hayano, Y., & Oya, S. 2014, in Society of Photo-Optical Instrumentation Engineers (SPIE) Conference Series, Vol. 9148, Proc. SPIE, 91481K

Hosek, Jr., M. W., Lu, J. R., Anderson, J., Ghez, A. M., Morris, M. R., & Clarkson, W. I. 2015, ApJ, 813, 27

Neichel, B., Lu, J. R., Rigaut, F., Ammons, S. M., Carrasco, E. R., & Lassalle, E. 2014, MNRAS, 445, 500

Rigaut, F., Neichel, B., Boccas, M., D'Orgeville, C., Vidal, F., van Dam, M. A., Arriagada, G., Fesquet, V., Galvez, R. L., Gausachs, G., Cavedoni, C., Ebbers, A. W., Karewicz, S., James, E., Lührs, J., Montes, V., Perez, G., Rambold, W. N., Rojas, R., Walker, S., Bec, M., Trancho, G., Sheehan, M., Irarrazaval, B., Boyer, C., Ellerbroek, B. L., Flicker, R., Gratadour, D., Garcia-Rissmann, A., & Daruich, F. 2014, MNRAS, 437, 2361

Service, M., Lu, J. R., Campbell, R., Sitarski, B. N., Ghez, A. M., & Anderson, J. 2016, Publications of the Astronomical Society of the Pacific, 128, 095004

Stolte, A., Ghez, A. M., Morris, M., Lu, J. R., Brandner, W., & Matthews, K. 2008, ApJ, 675, 1278

# Chapter 1

# Internal Kinematic Substructure of Westerlund 2 using proper motions

Note: This chapter will be submitted to a AAS journal with co-authors Jessica Lu, Mark Chun, Matt Hosek, Peter Boyle and Jay Anderson.

## 1.1 abstract

We use archival HST imaging to measure the proper motion of 6385 sources in a 180″ diameter field of view. Likely cluster members are identified by fitting the kinematic distribution with two elliptical Gaussians. We find significant proper motion differences which are correlated with the previously noted spatial substructure in this cluster. The two clumps are found to be approaching each other at a speed of $3.2 \pm 0.6$ km s$^{-1}$, projected on the plain of the sky. We combine these results with radial velocity measurements from the literature to estimate a lower limit on the required mass to gravitationally bind the system of $3.4 \pm 1.0 \times 10^4$ M$_\odot$, which is consistent with literature measurements of the total stellar mass in the cluster from star counts.. By comparing virial masses with estimates of the stellar mass for each individual sub-clump we find that the velocity dispersion in the main clump is consistent with the clump being in virial equilibrium The same comparison for the less massive Northern clump finds that it is not virialized as the estimated virial mass is much greater than the stellar mass.

## 1.2 Introduction

Young massive clusters offer an opportunity to study star formation in a controlled manner as clusters are a single age, single metallicity population with all stars formed in a common environment. Their youth ($< 10$ Myr) means that the observed stellar population is directly representative of the initial stellar population, and the high cluster mass ($> 10^4 M_\odot$) means that the high end of the stellar mass function is well sampled. Studies of the Arches and Quintuplet cluster in the Galactic Center environment have given insight into cluster formation (Espinoza et al. 2009; Hosek et al. 2015; Rui et al. 2019); however, these studies need a counterpoint in a different environment more representative of the Galactic disk. Westerlund 2 (Wd2) is of comparable age and mass to the Arches cluster (Clarkson et al. 2012), and is in the disk of the Galaxy instead of the Galactic center. Wd2 is at a distance of $4.16 \pm 0.07$ (random) $+0.26$ (systematic) kpc from Earth, has an age of $\lesssim 1 - 3$ Myr (Alvarez et al. 2013; Carraro et al. 2013; Zeidler et al. 2015), and has a mass of $\sim 10^4 M_\odot$ (Ascenso et al. 2007). Ultimately, joint studies of Wd2, Arches and Quintuplet cluster will allow for unique tests of the impact of environment on the star cluster formation process.

Previous work on Wd2 has suffered from contamination of the cluster measurements due to other stars along the line of sight, as the cluster membership was based solely on photometry (Ascenso et al. 2007; Zeidler et al. 2015; Hur et al. 2015). Simple cuts in the color magnitude diagram were used to identify likely cluster members. This is reasonably effective for Wd2 in part because the cluster is highly extincted which acts to separate the foreground sources from cluster members. However, Wd2 is coincident with the HII region RCW 49 (Rodgers et al. 1960), and has significant differential reddening (E(B-V) $\sim 1.87$) (Ascenso et al. 2007; Zeidler et al. 2015). This induces extra scatter in the CMD sequence of the cluster, which leads to errors in assigning cluster membership when cuts are made in the CMD. Using proper motions to measure membership would be a significant improvement, as it avoids introducing mass- and brightness-dependent biases into the selected stellar population and it can correctly eliminate background sources with a similar extinction.

However, a proper motion catalog for Wd 2 does not yet exist and most of the cluster members are too optically faint to be detected in Gaia.

Accurate cluster membership is essential for measurements of basic cluster parameters such as the distance, which is still debated (Ascenso et al. 2007; Rauw et al. 2011; Carraro et al. 2013; Alvarez et al. 2013; Hur et al. 2015), and age. Measuring precise cluster membership will enable a measurement of the projected spatial distribution of the stellar content and may allow for measurement of the projected kinematic structure. Previous works (Alvarez et al. 2013; Hur et al. 2015; Zeidler et al. 2015) have found evidence for a secondary clump of stars north of the main cluster which appears to be the same age. In addition, Zeidler et al. (2018) found that there is a bimodal distribution in the line-of-sight velocities with an offset between the peaks of 17 km/s; however, due to a small field of view they were unable to correlate the kinematic substructure with the spatial structure. Understanding the details of the kinematic and spatial sub-structure gives insight into the original matter distribution in material that the star formation occurred in, as the star formation is quite recent. These insights are particularly valuable in the sense that constraining models of the cluster formation helps determine if present day properties like mass segregation are primordial or due to dynamical evolution of the cluster. We present the first proper motion measurements of sources in the Westerlund 2 field which we used to test whether a similar offset exists in the plane of the sky and our coverage allows us to test if the kinematic differences are correlated with the spatial structure in the plane of the sky.

## 1.3 Observations

Westerlund 2 has been observed with the *Hubble Space Telescope* (HST) using the WFC3-UVIS, WFC3-IR and ACS-WFC cameras a total of 14 distinct times between 2013 and 2018 using the F814W filter (0.814 $\mu$m) as well as the F125W (1.25$\mu$m) and F160W (1.60$\mu$m) filters in 2013 during the following programs: 13038 and 14807 (Table 4.1). The ACS-WFC

Table 1.1. HST Observations

| Camera | Year | Filter | $N_{images}$ | $T_{exp}$(s) | PA (deg) | $\sigma_{pos}$ (mas) |
|---|---|---|---|---|---|---|
| WFC3-IR | 2013.68 | F160W | 16 | 250 | 11.0 | 0.53 |
| WFC3-IR | 2013.68 | F125W | 16 | 250 | 11.0 | 0.87 |
| ACS/WFC | 2013.68 | F814W | 4 | 350 | 6.4 | 0.65 |
| WFC3/UVIS | 2016.83 | F814W | 6 | 350 | 70.8 | 0.20 |
| WFC3/UVIS | 2016.97 | F814W | 6 | 350 | 122.1 | 0.20 |
| WFC3/UVIS | 2017.11 | F814W | 6 | 350 | 168.0 | 0.20 |
| WFC3/UVIS | 2017.25 | F814W | 6 | 350 | 225.0 | 0.20 |
| WFC3/UVIS | 2017.39 | F814W | 6 | 350 | 277 | 0.21 |
| WFC3/UVIS | 2017.58 | F814W | 6 | 350 | 336.7 | 0.24 |
| WFC3/UVIS | 2017.90 | F814W | 6 | 350 | 98.2 | 0.21 |
| WFC3/UVIS | 2018.18 | F814W | 6 | 350 | 194.6 | 0.25 |
| WFC3/UVIS | 2018.30 | F814W | 6 | 350 | 241.0 | 0.22 |
| WFC3/UVIS | 2018.37 | F814W | 6 | 350 | 267.9 | 0.22 |
| WFC3/UVIS | 2018.43 | F814W | 6 | 350 | 301.0 | 0.21 |
| WFC3/UVIS | 2018.51 | F814W | 6 | 350 | 313.5 | 0.21 |
| WFC3/UVIS | 2018.75 | F814W | 6 | 350 | 35.0 | 0.24 |

Note. — $T_{exp}$ refers to the exposure time per image. $\sigma_{pos}$ is the median error on the mean for sources in the catalog for that epoch.

and WFC-IR imaging (Program 13038) have been published in Zeidler et al. (2015). The *flt* images were used for this analysis and were downloaded on 2018 Oct 24. The observations were taken with many different angles, positions, and dither patterns; however, the most restricted field of view is set by the WFC3-UVIS observations centered on $\alpha$(J2000) = 10h 24m 01s, $\delta$(J2000) = -57° 45′ 13″ (Proposal ID:14807) with a 160" × 160" field of view and position angles of the camera rotating through almost two full rotations. The WFC3-IR observations are a mosaic of 4 pointings that cover the entire UVIS field of view, each consisting of 4 images that have a slight overlap so that the catalogs could be combined. Each of the UVIS observations consists of 6 × 350s exposures with 0.2" dithers between each frame. The observations are limited by the depth of the UVIS optical imaging, as the IR data go significantly deeper while still including the brightest sources in the optical imaging.

## 1.4 Data Reduction

### 1.4.1 Source Extraction

Initially we extract source catalogs from each image using using *hst1pass* (Anderson 2007). These catalogs are only used to extract matches between an arbitrary reference frame and each of the images. These matches are then used as the input for a more thorough source extraction which achieves greater depth by looking for sources that can only be detected by simultaneously searching in the stack of images.

For the intra-epoch alignment we use *hst1pass* (Anderson 2007) to extract preliminary catalogs from each image. These catalogs are then matched and transformed into the coordinate system of the first image in each epoch using a full first-order transformation. The transformed catalogs are then averaged to create a new master catalog for that epoch, which is used as the reference in a second pass of the matching and transformation process. This initial alignment is used as input to the source extraction to follow, as we need a set of matched coordinates between each individual image and a common reference frame as input for KS2. For the 2013 epoch, we use the optical F814W data as the initial reference catalog for the IR data.

The photometry and astrometry is re-extracted from the images using the KS2 reduction routine developed by J. Anderson (Anderson et al. 2008). KS2 identifies sources across multiple exposures and filters and estimates the brightness and position across all frames using an estimate of the point spread function that varies over the field of view. Source detection is performed iterativly, starting with the bright sources which are then subtracted from the stack in order to identify fainter stars. For the final iteration, we use the following quality cut inputs for the program (HMIN=1, SSIG=1.00, QMIN=99, QSEL=9.00, QSEP=0.75, DMIN=99, DSEP=0.50, PMIN=10, PSEP=1.25, OPRX=1.50, OPRV=2.5, RSIZ=0.25, see Anderson et al. (2008) for details on these parameters). These values were selected based on past experience reducing similar data sets. This procedure is applied to every epoch and produces catalogs with positional uncertainties as shown in

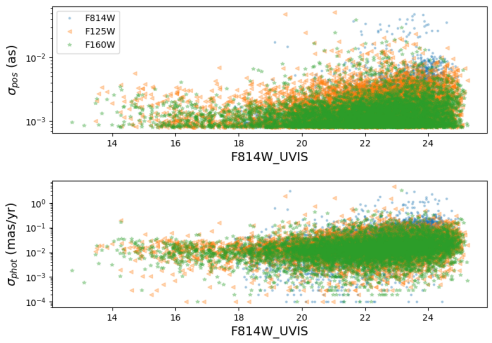


Figure 1.1 *Top:* Positional errors as a function of the F814W brightness of the source for each catalog. The F814W data is from a single UVIS epoch, which is typical for all sources. *Bottom*: Photometric errors in the individual catalogs as a function of magnitude.

Table 4.1. For the UVIS data, 6000-7000 stars are detected per epoch while in comparison, the 2013 WFC-IR catalogs contain 19356 stars and the 2013 ACS catalog contains 21154 stars; thus the 2016-2018 UVIS data is the most shallow.

In order to photometrically calibrate all catalogs, we perform a zeropoint correction. The published HST zeropoints only apply to aperture photometry. So, in order to calibrate the UVIS date we perform aperture photometry on the 2016.83 epoch and apply the known zeropoint. We then compare to the aperture photometry to the KS2 photometry and estimate the appropriate zeropoint to be applied to KS2 data. For the UVIS data we find a zeropoint of $\mathrm{ZP}_{KS2,UVIS} = 24.54 \pm 0.04$ mag. For the other filters we use the zeropoints calculated previously using the same general methodology; the details can be found in Hosek et al. (2018). The final catalog errors for the positions and the photometry are shown in Figure 1.1

### 1.4.2 Cross-Epoch Alignment

A precise cross epoch alignment of stellar catalogs is required to measure proper motions with sufficient accuracy for this work. Performing this alignment is an iterative process, where we alternate between aligning the observed catalogs to the current reference frame and then fitting proper motions for all sources. For this purpose, we start our by using the 426

Gaia DR2 catalog sources that are within our field of view (Lindegren et al. 2018). The Wd 2 Gaia catalog is projected onto a tangent plane at the center of the cluster at $\alpha = 156.0°$, $\delta = -57.76°$ and the celestial coordinates are converted to units of arcseconds offset from the center. The initial alignment uses a linear parameter transformation to transform each catalog from detector coordinates into the Gaia reference frame while taking into account the measured proper motions of the Gaia catalog. The non-Gaia stars from each epoch are then added to the reference table for subsequent iterations. Every time a new catalog is added, it is first matched to the current reference table positions (accounting for the proper motions), then sources not detected in the current reference table are added, and finally new proper motions are fit for all sources.

This proper motion fitting process is iterative, in the sense that, after the transformation coefficients are fit, we fit each stars' proper motion and then refit the transformation coefficients. This is process is repeated 3 times, and for the final alignment we only use sources that meet the following criteria to build the reference frame: First the stars with measured proper motions greater than $\pm$ 0.75 mas/year are eliminated. Then stellar position measurements with errors larger than 0.6 mas are also eliminated. In addition to the cuts on the reference frame, we also eliminate anomalous sources on a per frame basis by sigma-clipping stars with large residuals between the observed position and the expected position. For the first alignment pass we use a 5-$\sigma$ outlier threshold and then change to a 3-$\sigma$ outlier threshold for the final two iterations. In addition to the outlier rejection, we also decrease the matching radius in each subsequent iteration from 0.2 as to 0.1 as to 0.05 as. Finally, we use progressively higher-order polynomial transformations in this process starting from linear to $2^{nd}$ order to $3^{rd}$ order. Note that we fit our linear motion in the right ascension axis including the tangential projection using $\mu_{\alpha*} = \mu_\alpha \cos(\delta)$ where $\delta$ is the mean declination of our field. For the remainder of the paper we present our results as $\mu_{\alpha*}$.

We would typically only use bright sources in the final alignment to avoid introducing additional noise into the transformation process. However, this is problematic for the UVIS imaging due to uncorrected residual charge transfer efficiency effects on the chip, which

cause systematic position offsets that are a function of source brightness and position on the chip. To correct this issue, the input UVIS catalogs are first split based on the brightness of the source before aligning them to a common reference frame. This allows for different transformation coefficients for each split catalog which can correct for the common optical distortion and the magnitude dependent residuals. We split the sources into 6 bins with the breaks at using the average F814W magnitudes for each source and bin edges of 18.5, 20, 21, 22 and 23. Using the average brightness ensures that each source is always in the same bin. This additional correction has an important impact on the final astrometric catalog, as typically the distortion polynomials are only derived using the sources with the lowest astrometric error. Splitting the data in this fashion has the potential to create offsets in the reference frame between the different magnitude bins, however, the requirement that all sources are measured in one of the 2013 epochs ensures that the all share a common reference frame. The residuals in the final transformations range from 0.7 to 3.0 mas RMS for the sources used in the transformations. The largest residuals are in the faintest magnitude bin for the UVIS data with typical values over 3 mas; for the rest of the data the typical residual after transformation is 1.4 mas. These values are larger than expected from the estimate of the positional errors in the individual catalogs (4.1), we attribute this discrepancy to uncorrected (high order) optical distortion variation between the different observation epochs.

The final catalog has a total of 6385 sources with median proper motion errors of 0.2 mas/yr where the errors are estimated based on the fitting error in the linear models. The measured proper motions for all sources are shown in Figure 1.3as well as the associated errors (Figure 1.2.

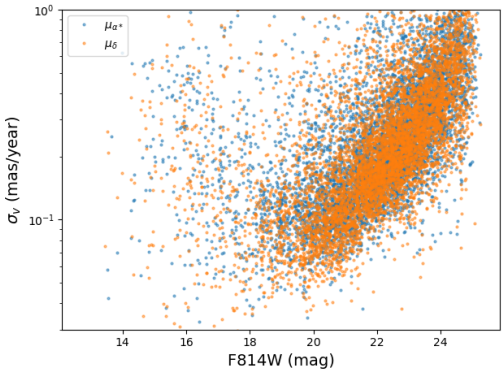


Figure 1.2 Measured proper motion errors in the final catalog. The $\mu_\delta$ errors are shown in orange while the $\mu_{\alpha*}$ errors are shown or orange. Errors increase for bright stars due to our use of shallow, short exposure data, which cannot be corrected for the magnitude-dependent distortions. As a result the alignment for bright stars is much less accurate.

## 1.5 Analysis

### 1.5.1 Kinematic Membership

We use the measured proper motions of the stars to identify likely cluster members. Proper motion-based cluster membership is independent of the brightness or color of the stars; however, it does rest on the assumption that the stars in the cluster move together while other stars along the line-of-sight do not. In order to characterize the velocity structure in the observed stars we use a 2 Gaussian model; one for the cluster sources and one for the background. To fit the model we follow the fitting process used in previous works (Stolte et al. 2014; Hosek et al. 2015; Rui et al. 2019). In this case we set $K = 2$, where one Gaussian is the cluster sources and the other accounts for the field population. We use elliptical Gaussians for both distributions, which is necessary to match the observed kinematic structure in the cluster members. We apply this framework to the problem of fitting the observed velocity distribution in this field. For this fitting, we adopt uniform priors for the model parameters of the Gaussians for both the field and the cluster; this includes the rotation angle ($\theta$), semi-major standard deviation ($\sigma$), ratio between the semi-minor and semi-major standard deviation ($f$), mean proper motion in both axes ($\mu$) and the fraction of stars in each Gaussian ($\pi$).

Table 1.2. Kinematic Fit

| Quantity | Cluster | Field |
|---|---|---|
| $\theta$(radians) | 2.220±0.068 | 2.584±0.044 |
| $f$ | 0.733±0.034 | 0.646±0.025 |
| $\sigma$(mas yr$^{-1}$) | .312±0.011 | 2.45+0.074−0.067 |
| $\mu_{\alpha*}$(mas yr$^{-1}$) | 0.117±0.009 | 0.65±0.025 |
| $\mu_{\alpha*,\mathrm{gaiadr2}}$(mas yr$^{-1}$) | -4.73±0.009 ± 0.16 | -4.19±0.025 ± 0.16 |
| $\mu_{\delta}$(mas yr$^{-1}$) | -0.052±0.009 | -0.612±0.088 |
| $\mu_{\delta,\mathrm{gaiadr2}}$(mas yr$^{-1}$) | 2.778±0.009 ± 0.13 | 2.218±0.009 ± 0.13 |
| $\pi$ | 0.733±0.011 | 0.267±0.011 |

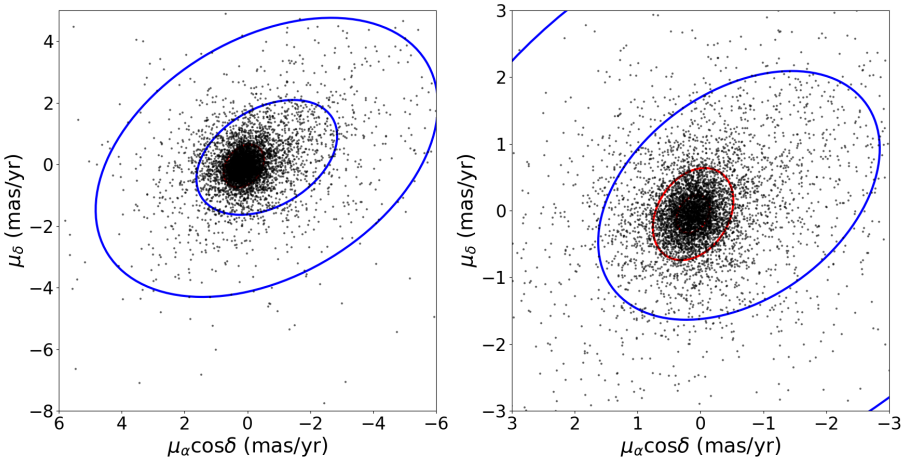


Figure 1.3 Vector point diagram for all sources in the final catalog. The 1-$\sigma$ and 3-$\sigma$ contours of the best fit Gaussian model are shown for both the cluster (red) and field (blue).

*Multinest* is then used to estimate the posterior probability distribution (Feroz et al. 2009). This software implements an alternative approach to Markov chain Monte Carlo algorithm, which identifies peaks in the posterior distribution and restricts future sampling to those regions until the output distribution is well sampled. The best fit parameters are shown in Table 1.2. We use the mean measurement of the cluster Gaussian as the estimate of the bulk motion of the cluster To estimate the absolute proper motion of the cluster, we estimate the proper motion of the field using sources with proper motion errors less than 0.7

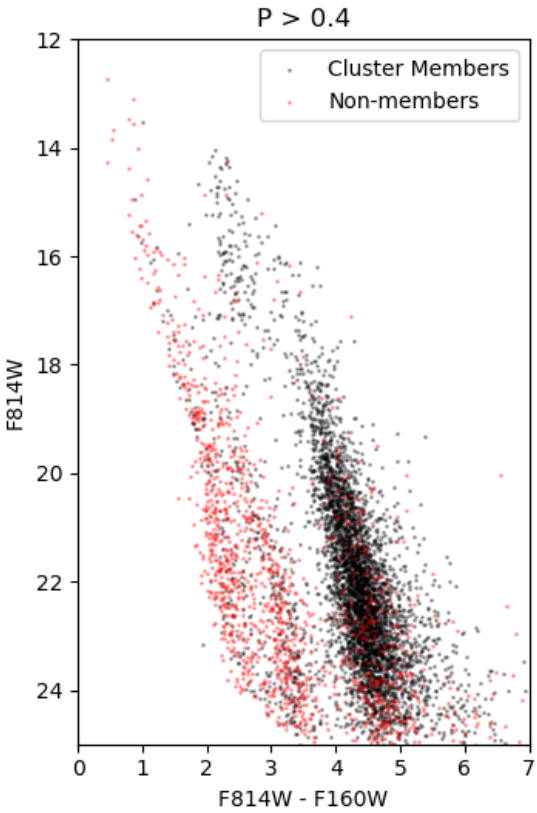


Figure 1.4 Optical CMD with cluster members shown in black. Stars with kinematic membership probability less than 0.4 are shown in red.

mas/yr with brightness between 17 and 18 in F814W. This gives on offset for the reference frame of 4.84 ± 0.16 mas/yr and 2.83 ± 0.13 mas/yr for $\mu_{\alpha*}$ and $\mu_\delta$ respectively.

### 1.5.2 Sub-Cluster Fitting

$$\mathcal{L} = \prod_{i=1}^{N} \mathcal{L}_i \tag{1.1}$$

$$\mathcal{L}_i = F_1 \mathcal{L}_{1,i} + (1 - F_1)\mathcal{L}_{2,i}$$

Where the likelihood for the individual ($i$) stars on the first sub-cluster is defined as:

$$\mathcal{L}_{i,1} = \mathcal{G}_{pos,1,i} \cdot \mathcal{G}_{vel,1,i} \tag{1.2}$$

$$\mathcal{G}_{vel,1,i} = \frac{1}{2\pi|\Sigma_{vel,1,i}|^{1/2}} exp\left(-\frac{1}{2}(\mu_i - \bar{\mu_1})^T \Sigma^{-1}_{vel,1,i}(\mu_i - \bar{\mu_1})\right) \tag{1.3}$$

$$\mathcal{G}_{pos,1,i} = \frac{1}{2\pi|\Sigma_{pos,1,i}|^{1/2}} exp\left(-\frac{1}{2}(x_i - \bar{x_1})^T \Sigma^{-1}_{pos,1,i}(x_i - \bar{x_1})\right) \tag{1.4}$$

where $\Sigma_{vel,1,i} = S_{vel,i} + Z_{vel,1}$ where $S_{vel,i}$ is the velocity covariance of the $i$th star and $Z_{vel,1}$ is the covariance matrix of the velocity distribution for the first sub cluster, $\mu_i$ is the proper motion of the $i$th star and $\bar{\mu_1}$ is the mean proper motion of the first Gaussian. Correspondingly, $\Sigma_{pos,1,i} = S_{pos,i} + Z_{pos,1}$ where $S_{pos,i}$ is the positional covariance of the $i$th star and $Z_{pos,1}$ is the covariance matrix of the positional distribution for the 1st sub cluster, $\bar{x_1}$ is the mean position of the first sub cluster, and $x_i$ are the positions of the $i$th star. $F_1$ gives the relative amplitude of the first sub cluster, where it is bound between 0 and 1.

Previous studies have noted the two peaks in the spatial distribution of stars in this field, and this model allows us to see if there is velocity structure associated with the spatial structure. When we fit this model, we trim sources with kinematic membership probability less than 0.3, sources with proper motion errors larger than 0.4 mas/year in either axis and all sources that are more than 30 arcseconds from both of the density peaks (see Figure 1.5 for the relevant regions). This is done to mitigate the effects of other structures in the field of view, such as contaminating field sources with a uniform spatial distribution. These cuts

leave a total of 1556 stars which we fit the sub-clumps model to with best fit parameters as shown in Table 1.3.

## 1.6 Results

### 1.6.1 Bulk Cluster Properties

The absolute proper motion of the total cluster is -4.84 ± 0.16 mas/yr and 2.83 ± 0.13 mas/yr for $\mu_{\alpha*}$ and $\mu_{\delta}$ respectively in the Gaia DR2 reference frame (Lindegren et al. 2018). In Galactic coordinates this is converts to $\mu_{l*}$ = -5.60 ± 0.07 mas/yr (-111 km/s) and $\mu_b$ -0.2± 0.2 mas/yr (3.9), which is consistent with the expectation that star formation is confined to the Galactic plane. Previous studies of Westerlund 2 have identified substructure in the cluster in the form of two local density peaks (Hur et al. 2015; Zeidler et al. 2015, 2017). We find the same spatial structure in our new analysis using kinematic membership. Our measured spatial distributions is weighted by the kinematic membership probability plotted in Figure 1.5. One possible concern is that this spatial distribution could be due to a band of extinction between the two local density peaks, masking out the light from the true peak. We rule this out as previous works which estimated the differential extinction across the field found the same did not find evidence for a larger extinction band in that location (Zeidler et al. 2015). The luminosity function for each sub-clumps and the total cluster are shown in Figure 1.6. These results are consistent with the results of similar analysis from Zeidler et al. (2017). The relative dearth of faint stars in the center is primarily due to crowding reducing the completeness in this region.

### 1.6.2 Cluster Sub-Groups

The resulting best fit models are shown in Figure 1.8 and Table 1.3. For clarity, Figure 1.7 shows the 2d model and data collapsed along one axis to show how the data compares with the model. The notable result of this fit is the two sub-clumps are moving towards each other along the declination axis at a rate of 0.164 ± 0.060 mas $yr^{-1}$ (3.2 ± 1.2 km $s^{-1}$)

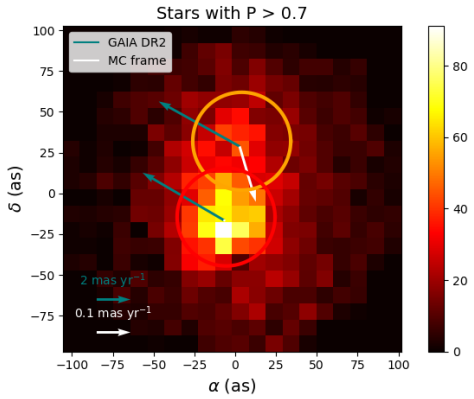


Figure 1.5 Shown here is the density map of cluster members weighted by their cluster membership probability. The orange and red circles show the total region used to estimate the substructure. The teal arrows teal show the motion in the GAIA DR2 reference frame while the white arrow shows the relative motion of the northern clump with respect to the main clump. The white arrow is magnified 20× with respect to the absolute motion. The absolute motion is parallel to the galactic plane with not statistically significant motion out of the plane.

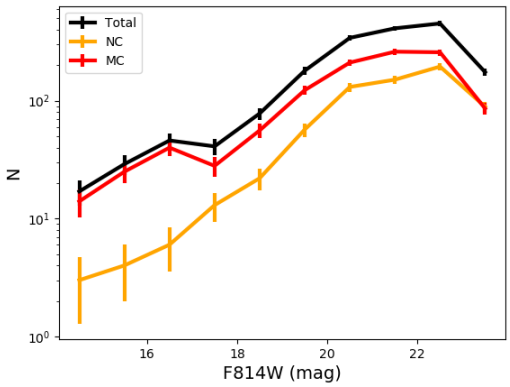


Figure 1.6 Luminosity function for the region considered in the sub-clumps model fit. Only stars within 30 as of one of the density peaks with proper motion errors less than 0.4 mas/year are included. For each sub-clumps, stars with a probability $> .7$ to be in that association are included. Note that the dearth of fainter sources in the Main cluster is likely due to incompleteness due to crowding in the cluster core.

where we assume a distance of 4.16 ± 0.33 kpc (Zeidler et al. 2015). Note that we include the line of sight distance error in the error propagation for the physical velocities and masses in the subsequent analysis. We can combine the proper motion velocity differences with the measured radial velocity of cluster members from the literature; Zeidler et al. (2018) found a bimodal radial velocity distribution in 72 likely cluster members centered in the northern part of the field. It is a reasonable assumption that the two peaks in their distribution is due to contributions from the tail of the main clump sources as well as some northern clump sources, however, we cannot identify the correspondence between the peaks in the proper motion and radial velocity distributions. Despite that ambiguity, we can still estimate the total 3d velocity difference between the two clumps by combining this velocity offset with the previously measured radial velocity offset of 17.3 ± 2.2 km $s^{-1}$ (Zeidler et al. 2018), we estimate a total velocity difference of 17.60 ± 2.5 km $s^{-1}$. We can assume that the two sub-clumps are bound, and further that the main clump is significantly more massive than the northern clump, such that the center of mass is the centroid of the main cluster. We use the projected distance in the plane of the sky as the distance between the two subclumps (0.93 ± 0.11 pc) These assumptions give a lower limit of $M > 3.4 \pm 1.0 \times 10^4$ $M_\odot$. This assumes that the cluster is bound and that the difference in the line of sight distance to the two sub-clumps is negligible. Note that additional distance between the clumps along the line of sight will only increase the mass estimate. For example, if the two sub-clumps are separated by the same distance along the line of sight as they are in the plane of the sky, then the mass limit is $M > 4.8 \pm 1.4 \times 10^4$ $M_\odot$.

We can also estimate the mass of the individual clusters using the measured velocity dispersions and a virial argument. To do so, we use equation 1.5

$$M_{\rm virial} = \frac{3{\rm HWHM}_{pos}\sigma_{vel}^2}{G} \tag{1.5}$$

where we use the half-width at half maximum ($1.175 \times \sigma_{\rm pos}$) of the positional Gaussian as the characteristic distance between sources and assume that the velocity dispersion in the line

Table 1.3. Kinematic Substructure

| Name | $F$ | $\mu_{\alpha*}$(mas yr$^{-1}$) | $\mu_{\delta}$(mas yr$^{-1}$) | $\sigma_{vel}$(mas yr$^{-1}$) | $\alpha*$(as) | $\delta$ (as) | $\sigma_{pos}$(as) |
|---|---|---|---|---|---|---|---|
| Main Clump | 0.617±0.038 | -0.065±0.041 | 0.078±0.041 | 0.27±0.03 | 5.57±1.4 | -16.5±2.36 | 13.5±1.0 |
| Northern Clump | 0.381±0.056 | -0.017±0.040 | -0.086±0.043 | 0.22±0.03 | -2.7±1.7 | 28.8±2.3 | 14.9±1.7 |

Note. — Here the velocities are presented in the cluster rest frame.

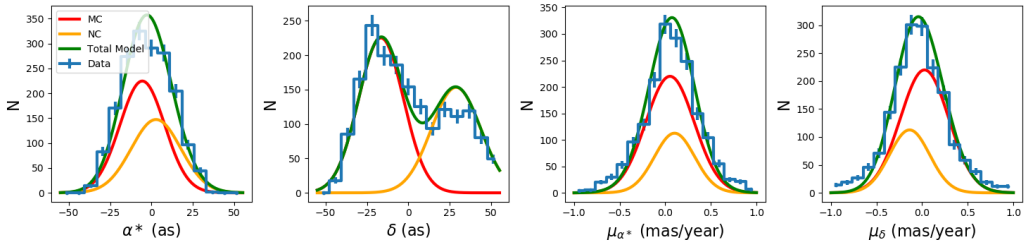


Figure 1.7 Marginalized histograms of the stellar positions and velocities for the kinematic members with the subcluster model overplotted. Only sources with velocity errors $< 0.4$ mas/year, kinematic membership probability $> 0.3$ and within 30 arcseconds of the center of one of the peaks are considered. We note that the Gaussian model does not perfectly match the level of spatial substructure present in the data, however, it is an approximation which allows us to see that the two peaks have distinct mean velocities.

of sight is the same as in the plane of the sky. This approach gives a mass of $2.6 \pm 0.7 \times 10^4$ $M_{\odot}$ for the main clump and $1.9 \pm 0.5 \times 10^4$ $M_{\odot}$. Thus we estimate a total virial mass of $4.5 \pm 0.8 \times 10^4$ $M_{\odot}$which is sufficient to imply that the system is bound.

### 1.6.3 Fast Moving Cluster Members

It is worth investigating whether there is evidence for rapidly moving cluster sources ejected from the cluster via 3-body interactions. To search for these sources we select sources with low kinematic cluster membership ($< 0.3$) who's photometry lies along the cluster color sequence. In addition we trim out sources with proper motion errors $> 0.25$ mas yr$^{-1}$ and fainter than 21 mag in F814W. This leaves 12 sources, however, the specific cause of these sources is not entirely clear. 11 of the 12 sources lie between the 3 and 4 $\sigma$ contours of the

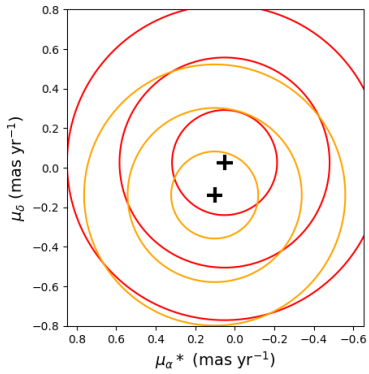


Figure 1.8 Here is the model fit to the Proper Motion for stars in the two regions plotted in the cluster reference frame. The northern clump is plotted in orange and the central clump is plotted in red. The average $v_y$ is offset by 0.16 mas/yr (3.2 km/s), and the mean velocities for each fit are shown as the black points. The contours for each model are at the 1,2 and 3-$\sigma$ levels.

cluster velocity Gaussian's. The final source is potentially more interesting, however some more study is merited to understand its most likely source.

## 1.7 Discussion

To convert from angular units to physical quantities we assume a distance of 4.16 ± 0.33 kpc to the cluster and include the distance error in the estimate of the physical quantities (Zeidler et al. 2015). The first important point is that as expected the cluster is moving along the galactic plane with no measurable out of the plane component in the proper motions ($\mu_b = 3.9 \pm 3.9$ km s$^{-1}$. We can also compare the velocity dispersions measured for the two sub-clumps to the the velocity dispersions found in the radial velocity structure and we see that the values agree within 1-$\sigma$ (Zeidler et al. 2018). The bi-modal radial velocity distribution has dispersions of 4.52 ± 1.78 km s$^{-1}$ and 3.46 ± 1.29 km s$^{-1}$ while the proper motion dispersions for the two sub-clumps are 5.3 ± 0.6 km/s and 4.3 ± 0.6 km/s. Although we do not know how the velocity structure corresponds between the proper motion and kinematic space, they all agree within the associated errors.

Table 1.4. Results

| Quantity | Main Clump | Northern Clump | Total Cluster |
|---|---|---|---|
| $\mu_{\alpha*}$ (km/s) | 1.28±0.8 | 0.34±0.8 | |
| $\mu_{\delta}$ (km/s) | 0.5±0.8 | -2.7±0.8 | |
| $\sigma_v$ (km/s) | 5.3±0.7 | 4.3±0.7 | |
| $\sigma_{pos}$ (pc) | 0.27±0.03 | 0.30±0.04 | |
| $M_{virial}$ ($10^4$ $M_\odot$) | 2.6±0.7 | 1.9 ± 0.5 | |
| $M_{binding}$ ($10^4$ $M_\odot$) | | | >3.4±1.0 |
| $M_{Stellar}$ ($10^4$ $M_\odot$) | 2.3±0.2 | 0.3±0.03 | 3.6±0.3 |

Note. — $M_{Stellar}$ are mass estimates derived for the stellar content from Zeidler et al. (2017). The velocities in The proper motions in this table are presented in km/s assuming a distance of 4.16 kpc. The proper motions are not in an absolute frame, the offsets to match to an absolute reference frame are -4.84 ± 0.16 mas/yr and 2.83 ± 0.13 mas/yr for $\mu_{\alpha*}$ and $\mu_{\delta}$ respectively.

The total mass for the cluster found from counting stars is 3.6 $\times 10^4 \pm$ 0.3 $M_\odot$. (Zeidler et al. 2018). This mass estimate for the cluster is consistent with the two sub-clumps being gravitationally bound. The same authors found a mass of 2.3 ± 0.2 $\times 10^4$ $M_\odot$ for the main clump and 0.3 ± 0.03 $\times 10^4$ $M_\odot$ for the northern clump. For the main clump the stellar mass is consistent with the virial mass, which suggests that this sub-clump is virialized. This agreement adds kinematic confirmation of the measurement of the present day mass function with a slope of $\Lambda = -1.65 \pm 0.06$ (Zeidler et al. 2017). The same is not true for the northern clump, where the virial mass is much greater than the measured stellar mass, which implies that the cluster is may be dissolving and that is not in virial equilibrium. Its worth noting that the stellar mass estimates use a cluster sample selected using color cuts and that the results might change for a sample selected based on proper motions. The results for the various regions of interest are summarized in Table 1.4.

## 1.8 Conclusions

We provide the first proper motion measurements for stars in the young massive cluster Westerlund 2. This enabled quantitative cluster membership estimation using kinematic

information instead of photometry. By comparing the measured proper motions in the distinct spatial clumps we find that the spatial substructure is correlated with the kinematic distribution. Additionally, we find that the two clumps are moving towards each other at a rate of 3.2 $\pm$ 1.2 km/s, which means they will be coincident on the sky within $\sim$ 0.3 Myr. Furthermore, the confirmation that the spatial structure has associated kinematic differences makes Westerlund 2 another example of a young massive cluster showing significant clumpy substructure (Kuhn et al. 2014). By combining our measurements with radial velocity measurements in the literature and assuming that the two distinct populations are bound, we estimate a lower limit of the cluster mass of 3.4 $\pm$ 1.0 $10^4$ $M_\odot$. This estimate assumes that the two clumps are at the same distance along the line of sight, if this is not true than the required mass for the total system to be bound increases substantially. If we assume that the line of sight distance is the same as the projected distance, the required mass goes up by 41%. We note that the total stellar mass of the cluster was measured to be 3.6 $\pm$ 0.3 $M_\odot$ (Zeidler et al. 2018), which means it is likely that the two subclusters are bound together. The line of sight distance between the two subclusters would have to be 1.2 pc (1.4$\times$ the projected distance) to create a 1-$\sigma$ discrepancy between the binding mass and the total stellar mass. Although the line of sight distance between the sub-clumps is unknown, these results are consistent with the two sub-clumps being gravitationally bound assuming that the line of sight distance is comparable to the projected distance on the sky.

The virial mass estimate for the Main clump is consistent with the literature for the stellar mass, which suggests that it is not expanding, however, this is not true for the Northern Clump. In that sub-clumps, the virial mass estimate is 1.9 $\pm$0.6 $10^4$ $M_\odot$, while the estimate of the stellar mass is 0.3 $\pm$ 0.03 $10^4$ $M_\odot$ which indicates that this sub-clumps is not in virial equilibrium (Zeidler et al. 2017). This suggests that the sub-clump is evaporating possibly due to interactions with the more massive sub-clump, however, given that the line of sight distance is unknown the exact physical scenario is uncertain. The more massive Main clump has a virial mass which is consistent with the stellar mass. The fact that the Main

cluster is in virial equilibrium offers additional support for the theoretical interpretation that star formation is a slow process as compared to the dynamical evolution time scale (Krumholz & Tan 2007).

We also find that our estimates of the velocity dispersion in the each of the sub-clusters matches the velocity dispersion measured in the radial velocity study, assuming the previously published distance of 4.16 kpc (Zeidler et al. 2015, 2018).

Young massive clusters do not consistently show significant substructure, however, there are other examples of "clumpy" clusters where a significant fraction of the stellar sources are found in sub-clumps (e.g. M17, Eagle Nebula Kuhn et al. (2014)). The finding of substructure in this cluster is consistent with other studies of young clusters, which have found a variety of substructure across young stellar clusters (Kuhn et al. 2014).

The catalog of sources, membership probability and proper motions is also supplied which can enable future analyses of the cluster parameters such as the degree of mass segregation and the initial mass function. The proper motion catalog for 6385 stellar sources in this region is a useful tool for future work as it enables more accurate measurements of initial mass function. For the case of Westerlund 2, it will also allow for a detailed kinematic analysis after the publication of the radial velocity catalog mentioned in Zeidler et al. (2019). We leave to future work the additional analysis necessary to produce an initial mass function estimate based on the kinematically selected cluster members.

# References


Alvarez, C. A. V., Kobulnicky, H. A., Bradley, D. R., Kannappan, S. J., Norris, M. A., Cool, R. J., & Miller, B. P. 2013, The Astronomical Journal, 145, 125

Anderson, J. 2007, Variation of the Distortion Solution of the WFC, Tech. rep.

Anderson, J., Sarajedini, A., Bedin, L. R., King, I. R., Piotto, G., Reid, I. N., Siegel, M., Majewski, S. R., Paust, N. E. Q., Aparicio, A., Milone, A. P., Chaboyer, B., & Rosenberg, A. 2008, AJ, 135, 2055

Ascenso, J., Alves, J., Beletsky, Y., & Lago, M. T. V. T. 2007, A&A, 466, 137

Carraro, G., Turner, D., Majaess, D., & Baume, G. 2013, A&A, 555, A50

Clarkson, W. I., Ghez, A. M., Morris, M. R., Lu, J. R., Stolte, A., McCrady, N., Do, T., & Yelda, S. 2012, ApJ, 751, 132

Espinoza, P., Selman, F. J., & Melnick, J. 2009, A&A, 501, 563

Feroz, F., Hobson, M., & Bridges, M. 2009, Monthly Notices of the Royal Astronomical Society, 398, 1601

Hosek, Matthew W., J., Lu, J. R., Anderson, J., Do, T., Schlafly, E. F., Ghez, A. M., Clarkson, W. I., Morris, M. R., & Albers, S. M. 2018, ApJ, 855, 13

Hosek, Jr., M. W., Lu, J. R., Anderson, J., Ghez, A. M., Morris, M. R., & Clarkson, W. I. 2015, ApJ, 813, 27

Hur, H., Park, B.-G., Sung, H., Bessell, M. S., Lim, B., Chun, M.-Y., & Sohn, S. T. 2015, MNRAS, 446, 3797

Krumholz, M. R. & Tan, J. C. 2007, ApJ, 654, 304

Kuhn, M. A., Feigelson, E. D., Getman, K. V., Baddeley, A. J., Broos, P. S., Sills, A., Bate, M. R., Povich, M. S., Luhman, K. L., Busk, H. A., Naylor, T., & King, R. R. 2014, ApJ, 787, 107

Lindegren, L., Hernández, J., Bombrun, A., Klioner, S., Bastian, U., Ramos-Lerate, M., de Torres, A., Steidelmüller, H., Stephenson, C., Hobbs, D., Lammers, U., Biermann, M., Geyer, R., Hilger, T., Michalik, D., Stampa, U., McMillan, P. J., Castañeda, J., Clotet, M., Comoretto, G., Davidson, M., Fabricius, C., Gracia, G., Hambly, N. C., Hutton, A., Mora, A., Portell, J., van Leeuwen, F., Abbas, U., Abreu, A., Altmann, M., Andrei, A., Anglada, E., Balaguer-Núñez, L., Barache, C., Becciani, U., Bertone, S., Bianchi, L., Bouquillon, S., Bourda, G., Brüsemeister, T., Bucciarelli, B., Busonero, D., Buzzi, R., Cancelliere, R., Carlucci, T., Charlot, P., Cheek, N., Crosta, M., Crowley, C., de Bruijne, J., de Felice, F., Drimmel, R., Esquej, P., Fienga, A., Fraile, E., Gai, M., Garralda, N., González-Vidal, J. J., Guerra, R., Hauser, M., Hofmann, W., Holl, B., Jordan, S., Lattanzi, M. G., Lenhardt, H., Liao, S., Licata, E., Lister, T., Löffler, W., Marchant, J., Martin-Fleitas, J.-M., Messineo, R., Mignard, F., Morbidelli, R., Poggio, E., Riva, A., Rowell, N., Salguero, E., Sarasso, M., Sciacca, E., Siddiqui, H., Smart, R. L., Spagna, A., Steele, I., Taris, F., Torra, J., van Elteren, A., van Reeven, W., & Vecchiato, A. 2018, A&A, 616, A2

Rauw, G., Sana, H., & Nazé, Y. 2011, A&A, 535, A40

Rodgers, A. W., Campbell, C. T., & Whiteoak, J. B. 1960, MNRAS, 121, 103

Rui, N. Z., Hosek, Matthew W., J., Lu, J. R., Clarkson, W. I., Anderson, J., Morris, M. R., & Ghez, A. M. 2019, ApJ, 877, 37

Stolte, A., Hußmann, B., Morris, M. R., Ghez, A. M., Brandner, W., Lu, J. R., Clarkson, W. I., Habibi, M., & Matthews, K. 2014, ApJ, 789, 115

Zeidler, P., Nota, A., Grebel, E. K., Sabbi, E., Pasquali, A., Tosi, M., & Christian, C. 2017, AJ, 153, 122

Zeidler, P., Nota, A., Sabbi, E., Luljak, P., McLeod, A. F., Grebel, E. K., Pasquali, A., & Tosi, M. 2019, arXiv e-prints, arXiv:1909.08143

Zeidler, P., Sabbi, E., Nota, A., Grebel, E. K., Tosi, M., Bonanos, A. Z., Pasquali, A., Christian, C., de Mink, S. E., & Ubeda, L. 2015, AJ, 150, 78

Zeidler, P., Sabbi, E., Nota, A., Pasquali, A., Grebel, E. K., McLeod, A. F., Kamann, S., Tosi, M., Cignoni, M., & Ramsay, S. 2018, AJ, 156, 211

# Chapter 2

# A New Distortion Solution for NIRC2 on the Keck II Telescope

Note this paper first appeared as Service et al. (2016) with co-authors: J. R. Lu, R. Campbell, B. N. Sitarski, A. M. Ghez, J. Anderson

## 2.1 Abstract

We present a new geometric distortion model for the narrow field mode of the near infrared camera (NIRC2) fed by the adaptive optics system on the W. M. Keck II telescope. The adaptive optics system and NIRC2 camera were realigned on April 13, 2015. Observations of the crowded globular cluster, M53, were obtained before and after the re-alignment to characterize the geometric field distortion. The distorted NIRC2 positions of M53 stars were compared with precise astrometry of this cluster from Hubble Space Telescope observations. The resulting distortion map constructed just before the re-alignment is consistent with the previous solution derived using data from 2007-2009. The distortion map changed significantly after re-alignment by an average of 4.5 mas (75%) and the new distortion model for post-realignment observations have a total accuracy of $\sim$1.1 mas.

## 2.2 Introduction

High-precision astrometry is a powerful tool in astrophysics. Diffraction-limited imaging on 8−10 m class telescopes has been used to study the Galactic center (GC) in detail, including the discovery of the super massive blackhole and studies of its surrounding stellar population (e.g. Eckart & Genzel 1997; Ghez et al. 1998; Genzel et al. 2003; Ghez et al. 2005; Paumard et al. 2006; Stolte et al. 2008; Lu et al. 2009; Bartko et al. 2009; Meyer et al. 2012; Clarkson et al. 2012; Yelda et al. 2014). A wide array of other science has similarly benefited, including measuring masses of stars and brown dwarfs from binary orbits (Konopacky et al. 2007; Liu et al. 2008; Dupuy et al. 2014, e.g.), determining exoplanet orbits (Pueyo et al. 2015; De Rosa et al. 2015, e.g.), measuring masses and densities of small bodies in the solar system (e.g. Grundy et al. 2015), and studying compact objects (e.g. Cameron & Kulkarni 2007b; Rudy et al. 2015). The near-infrared camera, NIRC2, on the W. M. Keck II telescope (PI: K. Matthews has been essential for a large number of these studies thanks to its stable and precise astrometry, yielding positional uncertainties as low as 0.15 milli-arcseconds (Lu 2008; Yelda et al. 2010).

Precise and accurate astrometry requires a thorough understanding of the imaging system used for observations. One limiting factor is knowledge of the geometric optical distortion in the imaging system. For example, uncorrected distortion in Galactic Center imaging of the masers leaves $> 1$ mas scale distortion (Yelda et al. 2010), which is at least a factor of 5-10 greater then the precision achieved with relative astrometry. In general these effects can be mitigated in crowded fields by using a large number of stars to transform individual exposures into a common astrometric reference frame. When the imaging system is stable, it is advantageous to measure the distortion and apply a distortion correction in the image analysis stage. Once distortion is corrected, individual exposures can be stacked to increase sensitivity. Another advantage is that even sparse fields can be distortion corrected.

Distortions in NIRC2 were initially characterized using illuminated pinhole masks (Cameron & Kulkarni 2007a). However, the residual distortion in those solutions was

still large compared to the relative astrometric error. On-sky data of M92 was used in Yelda et al. (2010) to measure the geometric distortion. The primary difference in these two approaches is the degree of systematic errors in the reference positions. In the case of the mask, reference position errors are set by how precisely the mask is manufactured. The on-sky experiment utilized Hubble Space Telescope (HST) data as the distortion-free external reference where the systematic noise is set by the residual distortion in that system. The distortion solution produced from on-sky data is more accurate ($\sim$ 1.1 mas Yelda et al. (2010)) , as the residual distortion in the HST reference is much smaller than the residual distortion in the solutions measured using pinhole masks ($\sim$2-3 mas Cameron & Kulkarni (2007a)). A superior approach to distortion characterization would be to estimate the distortion-free reference positions from the observations themselves and dispense with the need for an external reference frame, as was done when deriving the HST distortion solution (Anderson & King 2006). However, this requires observations with large translations at many orientations to constrain all high-order modes of distortion. The primary advantage of adopting an external reference is that we can measure the distortion of NIRC2 with a much smaller set of on-sky data as compared to the data set used to derive the HST distortion solution (Anderson & King 2006).

Previous work has demonstrated that the distortion of the NIRC2 system is stable over the period from 2007-2010 within the measurement errors for the solution (Yelda et al. 2010, $\sim$ 1.1 mas). However, the Keck II adaptive optics (AO) system that feeds NIRC2 was realigned on April 13, 2015 to improve a long standing issue of point-spread function elongation in 3-4 $\mu$m images. The source of this elongation was identified as the incorrect installation of the dichroic optic used to split between the infrared light passed to NIRC2 and the visible light used by the AO system. After the dichroic was adjusted to the correct orientation, further adjustments were needed to re-align the optical axis while keeping aberrations minimized. A side effect of these improvements is a change in the geometric distortion of the system as seen by the instrument. This change requires new observations to characterize the geometric distortion of the new system.

In this work, we derive a new geometric distortion solution for the near-infrared camera (NIRC2) behind the Keck II adaptive optics (AO) system. We show that the distortion solution has changed by ∼4.5 mas (75%) after April 13, 2015 as a result of realignment work on the optical system. In Section 3.4, we describe NIRC2 and HST observations of the globular cluster, M53, used to derive the new solution. Section 3.5 describes the data reduction and extraction of precise stellar positions. Section 2.5 describes how we use the stellar positions to fit distortion models for NIRC2 both before and after the system re-alignment. In Section 2.6, we derive errors and test both distortion solutions.

## 2.3 Observations

The first step in characterizing the geometric optical distortion in the NIRC2 camera is to measure stellar positions of a reference field. We use the dense globular cluster M53 as our reference field, and derive reference positions using HST/ACS imaging(§2.3.1). The distortion in the HST images has been characterized and can be corrected to $\lesssim$0.5 mas (Anderson & King 2006). We then compare the nearly distortion free reference positions to the distorted positions derived from NIRC2 imaging of the same field (§2.3.2). Our observations and methods mirror the process described in Yelda et al. (2010).

### 2.3.1 HST Observations of M53

M53 was observed with the Hubble Space Telescope on 2006 March 3 with ACS/WFC using the F814W filter. Five long (340 s) and one short (45 s) were taken centered on the M53 ($\alpha = 13^h12^m59^s$, $\delta = 18°10'18"$). The observations were taken with a position angle of -104.2° and plate scale of 49.72 mas/pixel van der Marel et al. (2007). These observations were part of the ACS Survey of Globular Clusters (GO-10775, PI: A. Sarajedini) and previously published in Anderson et al. (2008).

### 2.3.2 NIRC2 Observations of M53

M53 ($\alpha = 13^h12^m55^s$, $\delta = 19°10'8.4$") was observed on 2015 April 2 UT and 2015 May 5 UT using the laser-guide star AO system on the W. M. Keck II 10 m telescope with the facility near infrared camera NIRC2 (PI: K.Matthews). All observations were taken using the narrow field camera (10"×10") and the $K'$ filter ($\lambda_0 = 2.12$ $\mu$m, $\Delta\lambda = 0.35$ $\mu$m). We collected 133 science images in April and 100 science images in May with a total of 68 unique combinations of position angle (PA) and position offsets (Figure 2.1 and Table 2.1). The point spread function delivered to the camera had an average FWHM of 55 mas and Strehl ratio of 0.35. Typical rms variation of the FWHM across a frame was 3.0 mas, and the variation lacked obvious spatial structure across individual images.

To fully map the distortion solution, the scene of stars was dithered on the camera. This was done by dithering 2.5" in a square pattern from the central pointing and observed at two different position angles. This is required to measure the distortion, as we need measurements of the same source at many locations on the detector. Additionally, this mitigates the effect of outlier stars (i.e. high proper motion) on the final solution. We take multiple exposures (2-4) at each pointing so that we can evaluate positional errors for each star prior to aligning the data to a global reference frame. The tip-tilt star used for these observations has R $\sim$ 13.5 and is 24" West and 12" South of the central pointing.

Table 2.1. Summary of M53 images

| Date | P.A. (deg) | $\Delta_x$ (pix) | $\Delta_y$ (pix) | $N_{img}$ | $t_{exp}$ (s) | Coadds | FHMW (mas) | Strehl | $N_{stars}$ | $\sigma_{pos}$ (pixels) |
|---|---|---|---|---|---|---|---|---|---|---|
| 4/2/2015 | 0.0 | 0.0 | 0.0 | 4 | 5.0 | 10 | 64.3 | 0.27 | 76 | 0.072 |
| | 0.0 | -15.9 | -15.1 | 3 | 5.0 | 10 | 54.0 | 0.38 | 71 | 0.064 |
| | 0.0 | 18.1 | 1.6 | 4 | 5.0 | 10 | 69.8 | 0.22 | 62 | 0.064 |
| | 0.0 | -16.0 | 3.9 | 4 | 5.0 | 10 | 53.9 | 0.37 | 117 | 0.086 |
| | 0.0 | -251.6 | -0.1 | 4 | 5.0 | 10 | 55.9 | 0.32 | 117 | 0.081 |
| | 0.0 | -266.8 | -16.8 | 4 | 5.0 | 10 | 64.3 | 0.23 | 88 | 0.081 |
| | 0.0 | -230.4 | 0.4 | 4 | 5.0 | 10 | 60.9 | 0.26 | 98 | 0.086 |
| | 0.0 | -266.7 | 1.5 | 4 | 5.0 | 10 | 60.9 | 0.28 | 95 | 0.074 |
| | 0.0 | -502.6 | -1.8 | 4 | 5.0 | 10 | 55.0 | 0.34 | 114 | 0.082 |
| | 0.0 | -516.2 | -17.9 | 4 | 5.0 | 10 | 57.7 | 0.29 | 105 | 0.086 |
| | 0.0 | -482.7 | 2.6 | 4 | 5.0 | 10 | 53.0 | 0.36 | 123 | 0.091 |
| | 0.0 | -516.2 | 1.7 | 4 | 5.0 | 10 | 56.3 | 0.32 | 86 | 0.090 |
| | 0.0 | -747.6 | -2.7 | 3 | 10.0 | 5 | 71.1 | 0.17 | 60 | 0.086 |
| | 0.0 | -768.2 | -18.6 | 2 | 10.0 | 5 | 56.4 | 0.31 | 131 | 0.060 |
| | 0.0 | -730.6 | 0.0 | 3 | 10.0 | 5 | 56.6 | 0.30 | 133 | 0.067 |
| | 0.0 | 247.6 | 252.7 | 3 | 10.0 | 5 | 51.2 | 0.39 | 131 | 0.074 |
| | 0.0 | 230.7 | 236.4 | 3 | 10.0 | 5 | 50.2 | 0.45 | 148 | 0.083 |
| | 0.0 | 265.4 | 253.7 | 3 | 10.0 | 5 | 57.8 | 0.33 | 96 | 0.071 |
| | 0.0 | -1.1 | 252.7 | 3 | 10.0 | 5 | 49.8 | 0.45 | 171 | 0.067 |
| | 0.0 | -18.8 | 237.5 | 3 | 10.0 | 5 | 48.6 | 0.47 | 156 | 0.081 |
| | 0.0 | 17.1 | 253.8 | 3 | 10.0 | 5 | 52.3 | 0.37 | 152 | 0.073 |
| | 0.0 | -251.3 | 252.2 | 3 | 10.0 | 5 | 52.4 | 0.37 | 160 | 0.071 |
| | 0.0 | -269.0 | 236.0 | 3 | 10.0 | 5 | 54.7 | 0.33 | 138 | 0.070 |
| | 0.0 | -232.0 | 253.7 | 3 | 10.0 | 5 | 50.0 | 0.43 | 178 | 0.065 |
| | 0.0 | -501.5 | 250.7 | 3 | 10.0 | 5 | 55.1 | 0.33 | 114 | 0.067 |
| | 0.0 | -518.4 | 234.8 | 3 | 10.0 | 5 | 52.3 | 0.41 | 175 | 0.077 |

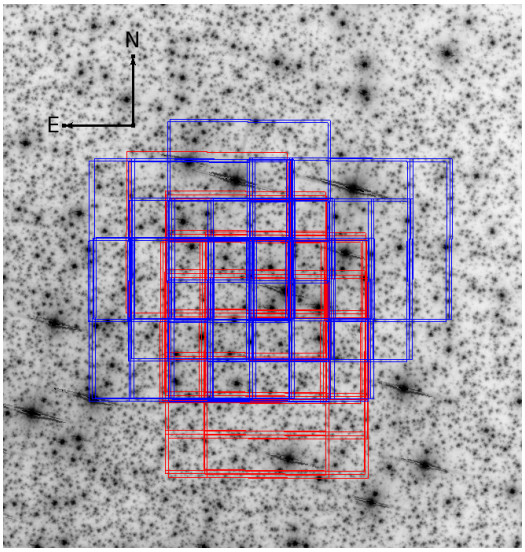


Figure 2.1 HST image of the M53 globular cluster, overlaid with NIRC2 pointings. The HST images were obtained with ACS/WFC in the F814W filter. Red boxes are NIRC2 observations taken in May, 2015. The blue boxes are NIRC2 observations from April, 2015. Each NIRC2 field is 10"×10".

Table 2.1—Continued

| Date | P.A. (deg) | $\Delta_x$ (pix) | $\Delta_y$ (pix) | $N_{img}$ | $t_{exp}$ (s) | Coadds | FHMW (mas) | Strehl | $N_{stars}$ | $\sigma_{pos}$ (pixels) |
|---|---|---|---|---|---|---|---|---|---|---|
| | 0.0 | -485.1 | 252.5 | 3 | 10.0 | 5 | 53.0 | 0.36 | 168 | 0.076 |
| | 0.0 | 498.8 | 505.0 | 2 | 10.0 | 5 | 49.3 | 0.46 | 150 | 0.060 |
| | 0.0 | 480.8 | 490.0 | 2 | 10.0 | 5 | 47.9 | 0.49 | 161 | 0.058 |
| | 0.0 | 517.7 | 508.5 | 3 | 10.0 | 5 | 48.9 | 0.46 | 151 | 0.071 |
| | 0.0 | 246.7 | 506.0 | 2 | 10.0 | 5 | 51.7 | 0.35 | 121 | 0.060 |
| | 0.0 | 230.1 | 490.7 | 3 | 10.0 | 5 | 49.5 | 0.41 | 157 | 0.079 |
| | 0.0 | 264.9 | 508.5 | 3 | 10.0 | 5 | 48.2 | 0.43 | 176 | 0.081 |
| | 0.0 | -505.8 | 501.7 | 3 | 10.0 | 5 | 58.4 | 0.28 | 68 | 0.091 |
| | 0.0 | -524.2 | 485.9 | 3 | 10.0 | 5 | 58.2 | 0.25 | 85 | 0.081 |
| | 0.0 | -486.5 | 504.4 | 3 | 10.0 | 5 | 52.0 | 0.31 | 110 | 0.073 |
| | 0.0 | -775.0 | 485.2 | 2 | 10.0 | 5 | 57.4 | 0.33 | 126 | 0.062 |
| | 0.0 | -738.8 | 502.4 | 3 | 10.0 | 5 | 58.9 | 0.30 | 116 | 0.094 |
| | 0.0 | -258.5 | 752.3 | 3 | 10.0 | 5 | 58.5 | 0.31 | 111 | 0.089 |
| | 0.0 | -274.9 | 736.6 | 3 | 10.0 | 5 | 61.2 | 0.32 | 115 | 0.093 |
| 5/5/2015 | 0.0 | 0.0 | 0.0 | 3 | 10.0 | 5 | 54.2 | 0.38 | 141 | 0.090 |
| | 0.0 | -14.4 | -16.0 | 4 | 10.0 | 5 | 64.9 | 0.23 | 75 | 0.009 |
| | 0.0 | 21.5 | 0.7 | 4 | 10.0 | 5 | 71.6 | 0.19 | 66 | 0.081 |
| | 0.0 | -250.4 | -1.9 | 4 | 10.0 | 5 | 68.6 | 0.19 | 72 | 0.100 |
| | 0.0 | -265.6 | -16.6 | 4 | 10.0 | 5 | 58.7 | 0.29 | 128 | 0.085 |
| | 0.0 | -229.3 | 0.6 | 4 | 10.0 | 5 | 58.7 | 0.28 | 124 | 0.091 |
| | 90.0 | 1040.2 | 24.4 | 4 | 10.0 | 5 | 55.9 | 0.30 | 136 | 0.089 |
| | 90.0 | 1054.4 | 5.5 | 4 | 10.0 | 5 | 53.8 | 0.35 | 169 | 0.098 |
| | 90.0 | 1039.4 | 42.2 | 4 | 10.0 | 5 | 54.0 | 0.33 | 165 | 0.097 |
| | 90.0 | 1036.7 | -224.4 | 3 | 10.0 | 5 | 50.5 | 0.27 | 127 | 0.079 |
| | 90.0 | 1054.3 | -245.4 | 3 | 10.0 | 5 | 49.0 | 0.31 | 140 | 0.085 |
| | 90.0 | 1034.6 | -199.2 | 3 | 10.0 | 5 | 48.2 | 0.31 | 129 | 0.091 |

Table 2.1—Continued

| Date | P.A. (deg) | $\Delta_x$ (pix) | $\Delta_y$ (pix) | $N_{img}$ | $t_{exp}$ (s) | Coadds | FHMW (mas) | Strehl | $N_{stars}$ | $\sigma_{pos}$ (pixels) |
|---|---|---|---|---|---|---|---|---|---|---|
| | 90.0 | 1037.2 | -472.9 | 3 | 10.0 | 5 | 48.7 | 0.33 | 137 | 0.084 |
| | 90.0 | 1055.1 | -495.0 | 3 | 10.0 | 5 | 47.7 | 0.34 | 142 | 0.081 |
| | 90.0 | 1034.5 | -448.6 | 3 | 10.0 | 5 | 49.0 | 0.34 | 143 | 0.090 |
| | 90.0 | 789.1 | 276.2 | 3 | 10.0 | 5 | 53.0 | 0.34 | 155 | 0.087 |
| | 90.0 | 807.9 | 254.7 | 3 | 10.0 | 5 | 52.5 | 0.28 | 138 | 0.076 |
| | 90.0 | 786.2 | 300.6 | 3 | 10.0 | 5 | 51.6 | 0.30 | 153 | 0.077 |
| | 90.0 | 788.4 | 26.2 | 3 | 10.0 | 5 | 54.1 | 0.30 | 160 | 0.082 |
| | 90.0 | 808.5 | 5.8 | 3 | 10.0 | 5 | 55.3 | 0.33 | 129 | 0.072 |
| | 90.0 | 789.2 | 50.1 | 3 | 10.0 | 5 | 58.7 | 0.26 | 119 | 0.33 |
| | 90.0 | 789.3 | -222.5 | 3 | 10.0 | 5 | 59.6 | 0.28 | 122 | 0.088 |
| | 90.0 | 808.0 | -244.2 | 3 | 10.0 | 5 | 64.9 | 0.19 | 79 | 0.068 |
| | 90.0 | 787.3 | -196.6 | 3 | 10.0 | 5 | 59.5 | 0.26 | 129 | 0.085 |
| | 90.0 | 787.0 | -472.7 | 3 | 10.0 | 5 | 51.7 | 0.39 | 153 | 0.089 |
| | 90.0 | 807.0 | -495.3 | 3 | 10.0 | 5 | 55.1 | 0.34 | 134 | 0.090 |
| | 90.0 | 787.0 | -449.5 | 3 | 10.0 | 5 | 61.2 | 0.29 | 106 | 0.090 |
| | 90.0 | 561.7 | 508.2 | 3 | 10.0 | 5 | 63.8 | 0.20 | 60 | 0.070 |
| | 90.0 | 541.3 | 551.8 | 3 | 10.0 | 5 | 65.2 | 0.25 | 78 | 0.088 |

## 2.4 Data Reduction

The five HST images were reduced using the standard reduction pipeline and the resulting $*$_flt.fits files were downloaded 2015 September 5. We note that these images are not yet distortion corrected. The PSF fitting routines developed by J. Anderson (img2xym, xym2mat, xym2bar, see Anderson et al. 2008) were used to extract positions from individual flat fielded images, correct distortion, and then collate the star lists to create a final stellar catalog from the HST images (Anderson 2007; Anderson & King 2006). Only stars detected in at least 3 images are included in the final catalog. We use this stellar catalog as our distortion free reference frame.

The NIRC2 images were reduced and calibrated for high precision astrometry using the methods described in Yelda et al. (2010). This involves background subtracting, flat fielding, cosmic ray cleaning, and bad pixel masking. Typically, distortion would also be corrected at this stage; however, as we are deriving a new distortion solution we do not apply these corrections. We also skip corrections for differential atmospheric refraction (DAR) as

they require knowledge of the distortion solution. We will account for DAR when fitting the distortion model (§2.5). After reducing the images, the point-spread function (PSF) fitting routine, StarFinder (Diolaiti et al. 2000), was used on each exposure. A correlation value of 0.8 was required to identify a stars in the images. *StarFinder* requires a set of PSF reference stars for each image. We selected a set of bright stars using the HST catalog, and then discarded stars that had secondary sources nearby ($\Delta(mag) < 4$ and $\Delta(r) < 0.1$"). Note that this step of source extraction assumes a single PSF for the entire image. A future analysis will combine an atmospheric and instrumental model to create a variable PSF for each image that accounts for anisoplantatism and field-dependent wavefront error, which should significantly improve on the the accuracy of this step. These stars were then visually inspected in the NIRC2 imaging to ensure that they were bright and isolated in the NIRC2 images. For each exposure, a list of stellar positions and brightnesses was generated. Star lists for each dither position were produced by averaging position measurements from all images taken at that pointing (2-4 images). Any stars that did not appear in at least 2 exposures was discarded. The RMS errors from the combined star lists are used as the positional uncertainties (Figure 2.2). This gives us a NIRC2 stellar catalog with positions and errors for each pointing.

## 2.5 New Distortion Model

The NIRC2 narrow-field camera has a geometric distortion that was well characterized and shown to be static from 2007-2009 by Yelda et al. (2010). We have performed a similar analysis on the M53 data from 2015 both before and after the system realignment. Our approach consists of comparing on-sky NIRC2 observations to an external astrometric reference frame defined by high-precision HST observations of the same field. Several advances in the methodology are presented. Specifically, we use bivariate Legendre polynomials as the fitting basis for the model rather than spline surface interpolations. We also use an iterative approach to calculate the distortion correction required to transform

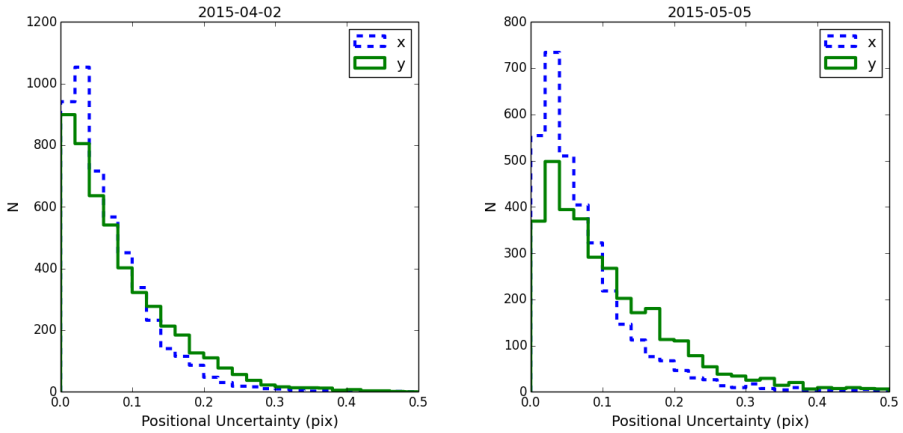


Figure 2.2 Positional uncertainties for all stars detected in the 2015-04-02 (*top*) and 2015-05-05 (*bottom*) data. These are the rms of the positions measured in all images taken at the same pointing. We include all of these stars in the subsequent analysis, and these errors are used to weight the fits of the geometric distortion (figure 2.8)

NIRC2 measurements into a distortion-free reference frame. These methodology changes reduced the impact of proper motions between the NIRC2 and HST observations, which have a larger impact in our data due to the longer time difference between observations (9 years vs. 3 years). The changes also improved convergence when estimating the distortion. More details are presented below in a complete description of the analysis methods.

### 2.5.1 Constructing the Model

Two data sets are needed to fit a distortion model: stellar positions in a distortion-free frame (i.e. HST catalog) and measurements of the same stars at many positions on the NIRC2 detector. Before fitting for the distortion model, two preparatory steps are needed. We need to account for the differential atmospheric refraction (DAR) and transform the distortion free coordinates into the reference frame of the NIRC2 camera. Ground based images are compressed along the zenith direction due to DAR and the amount of compression changes with zenith angle. Fortunately, DAR is predictable with a model of the Earth's atmosphere and measurements of the ground temperature, pressure, and humidity (Gubler & Tytler

1998), which are all readily available from the Mauna Kea Weather Center[1]. Ideally, we would magnify the NIRC2 star lists along the zenith angle to correct for DAR; however, the true positions of the stars are distorted and cannot be directly corrected for DAR until a distortion solution is applied. Instead we apply a compression to the HST positions as was done in (Yelda et al. 2010). This compression is different for every NIRC2 image, thus we produce a DAR-applied HST star list for each NIRC2 star list. We note that we only correct for achromatic DAR, since the effect of chromatic DAR ($< 0.2$ mas, Gubler & Tytler 1998) is smaller than the uncertainties in the HST ACS/WFC distortion solution ($\sim 0.5$ mas) and can be neglected.

The final step before fitting is to transform the HST coordinates into a matched list associated with each NIRC2 catalog. This is accomplished using a 4-parameter fit including plate scale, rotation and positional offsets in two directions. The stars are matched if they are within 3 NIRC2 pixels of each other ($\sim$30 mas). All sources that have more than one match within the search radius are discarded. The NIRC2 and transformed HST positions are differenced to give $\vec{\delta}_{i,e}(x_{\rm NIRC2}, y_{\rm NIRC2})$ for each star, $i$, and each NIRC2 star lists, $e$, at the NIRC2 detector position $(x_{\rm NIRC2}, y_{\rm NIRC2})$. Figure 2.3 shows all the measured positional differences(a total of 4890 measurements in April and 3609 measurements in May). There are more measurements in the April data set because there are more images in it. Large outliers due to mis-matches or confusion are eliminated by clipping all $3\sigma$ outliers in both X and Y in 205$\times$205 pixel bins, similar to Yelda et al. (2010). After clipping, there are 4779 measurements of $\vec{\delta}_{i,e}(x_{\rm NIRC2}, y_{\rm NIRC2})$ in April from 609 unique stars and 3336 measurements of $\vec{\delta}_{i,e}(x_{\rm NIRC2}, y_{\rm NIRC2})$ in May from 394 unique stars. The larger data set in April is simply due to the large set of data used, which also have more sky coverage.

The maps of $\vec{\delta}_{i,e}(x_{\rm NIRC2}, y_{\rm NIRC2})$ are fit with multivariate Legendre polynomials independently for the April and May datasets. We chose this basis set over spline surface interpolations previously used because the Legendre polynomials are an orthogonal basis set, which provide faster and more reliable convergence in our fitting procedure. We also

[1]http://mkwc.ifa.hawaii.edu/archive/wx/cfht/

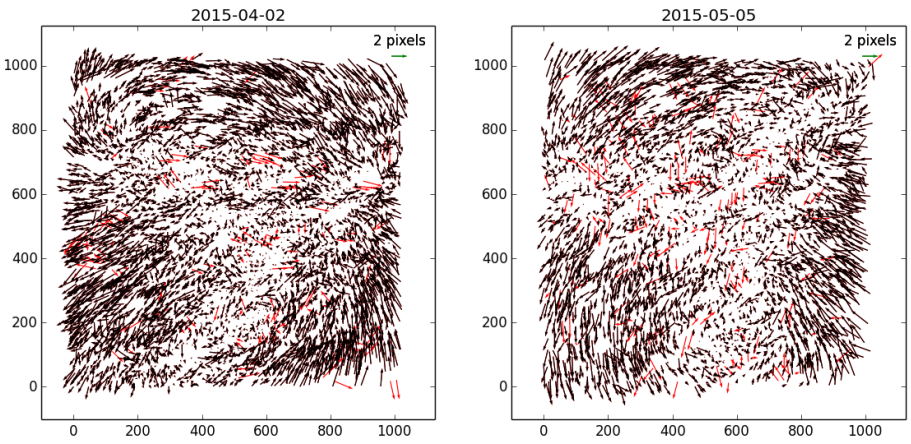


Figure 2.3 Observed positional differences between the HST and NIRC2 positions for the April *(left)* and May *(right)* data. Arrows in *red* are those rejected with sigma clipping. The change in distortion between the two data sets is clearly visible

explored Cartesian polynomials and found that fit residuals were larger than for Legendre polynomials with the same number of free parameters. We fit independent polynomials to the deltas in each axis:

$$\delta x_{i,e} = T_e(x_{HST,i}) - x_{NIRC2,i,e} \tag{2.1}$$

$$\delta x_{i,e} = a_0 \; + \; a_1 L_1(x) L_0(y) \; + \; a_2 L_0(x) L_1(y) \; + \; a_3 L_2(x) L_0(y) \; + \; a_4 L_1(x) L_1(y) \; + \; ... \tag{2.2}$$

where $L_n$ are the $n^{th}$ Legendre polynomials, $x_{NIRC2,i,e}$ are the measured positions on the NIRC2 detector, $T_e(x_{HST,i})$ are the HST positions that were transformed (only rotation, scale, offsets, DAR) into the NIRC2 frame and $[a_n]$ is the set of free-parameters. Equivalent independent coefficients are fit for the Y axis. The fits are weighted by the positional uncertainties in both the HST and NIRC2 data using a least squares minimization of $\chi^2$. We explored fitting with polynomials from third to eighth order. A statistical comparison, using an F-test, shows the significance of improvement gained by going to a successively higher order polynomials (Figure 2.4). A larger F value signifies greater improvement going

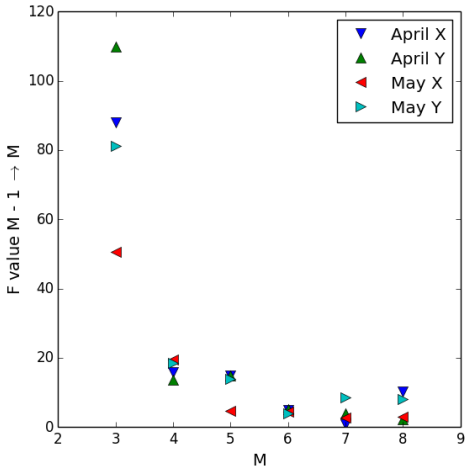


Figure 2.4 F values for all fitting orders tested. A higher value corresponds to a more significant improvement of the fit quality. There is significant improvement from going to at least fourth order, however, beyond that the gains are quite small.

from order M-1→M, which makes it clear that at least a $4^{th}$ order polynomial is needed. We select a $6^{th}$ order for consistency as it most closely matches the Yelda et al. (2010) solution, that is it has the fits have the smallest mean deviation across the entire NIRC2 detector. We note that this first fit does not account for the motion of the stars between 2006 and 2015.

### 2.5.2 Iterative Procedure

We mitigate the effects of proper motion by adopting an iterative approach. Note that the global motion and scale are eliminated by the four parameter transformations (translation, scale, rotation) between the star lists. However, the relative motion will add an offset on a star by star basis. As we expect most of the stars to physically exist in the M53, we can use the velocity dispersion (5.6 km/s Kimmig et al. (2015)) and distance (17.8 kpc Kharchenko et al. (2013)) give a velocity dispersion in the plane of the sky of 0.066 mas/year. This means that we expect offsets due to relative motion to appear at the $\sim$ 0.6 mas level due to the 9 year time baseline. Offsets due to relative motion will only appear between the HST reference and NIRC2 observations, so to mitigate the effects of these offsets we adopt

an iterative scheme that redefines the reference positions based on the NIRC2 data and an initial distortion solution. Note that this process can potentially mitigate other systematic effects due to residual distortion in the HST solution ($\lesssim 0.5$ mas), or any other large residual between the two instruments. We apply the first distortion solution to the NIRC2 catalogs, and then create a new reference frame by averaging all position measurements for each star. In detail, the individual exposures are first distortion-corrected. Then, each exposure is transformed into a common reference frame using a four-parameter fit (i.e. angle, scale, x offset, y offset) of the transformation between the individual NIRC2 catalogs and the HST reference. The distortion-corrected, transformed star lists are then averaged together to make a new reference frame is used in place of the HST measurements as the distortion-free frame. The fitting procedure is then repeated until the residual difference between the derived distortion solutions in successive passes is less than .05 mas (6 iterations). The total change in the distortion solution between the first fit and the final fit shows how the proper motions were affecting the fit (Figure 2.5). The average absolute value of the residual is $< 1.0$ mas, which is at the same level as the total uncertainty in the distortion model. Areas on the detector with the largest change in the iterative process correspond to the areas with the largest fitting errors, especially at the edge of the detector.

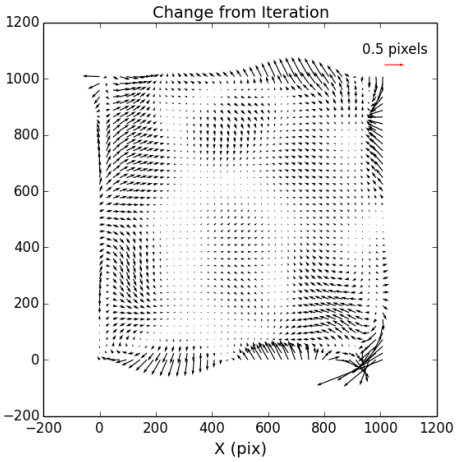


Figure 2.5 Change in the distortion model between the first and the final iteration for the 2015-05-05 data. We note that the average absolute value of the change is less than 0.09 pixels (0.9 mas), which is less than the total error in our solution.

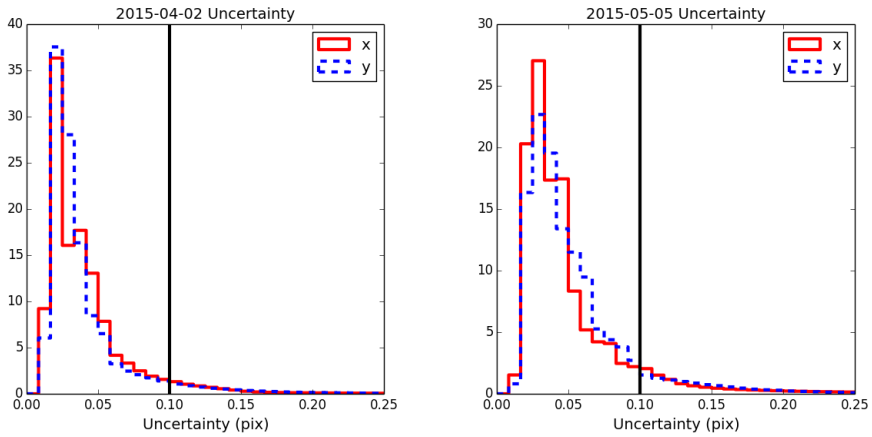


Figure 2.6 Fitting errors in the distortion solutions for 2015-04-02 (*left*) and 2015-05-05 (*right*). The vertical line indicates the residual distortion in the solutions. The distribution of uncertainties for all pixels in the distortion model lookup table yield a mean uncertainty for the 2015-04-02 model of 0.042 pixels in both X and Y. The 2015-05-05 solution has mean uncertainties of 0.53 mas in X and 0.55 mas in Y.

### 2.5.3 Uncertainty in the distortion model

The uncertainty in the distortion model fit is estimated using a half-sample bootstrap method. For each of 100 trials, we randomly sample half of the data with replacement of the measurements and repeat the entire fitting process for both the April and May data. The half-sample is selected prior to the sigma clipping. The fitting procedure (including clipping) produces 100 different distortion lookup tables and we adopt the rms scatter at each pixel as the fitting error in that pixel. Figure 2.7 show the errors for each pixel on the NIRC2 camera. The 2015-05-05 solution has mean fitting errors of 0.53 mas and 0.54 mas in X and Y respectively.

## 2.6 Results

Our main results are the distortion solutions shown in Figure 2.8 and their associated errors (Figures 2.6 and 2.7). These are lookup tables generated by evaluating the fits from the previous section at the center of every pixel on the NIRC2 detector and are the values which should be added to raw NIRC2 positions to shift them to a distortion free frame. We also

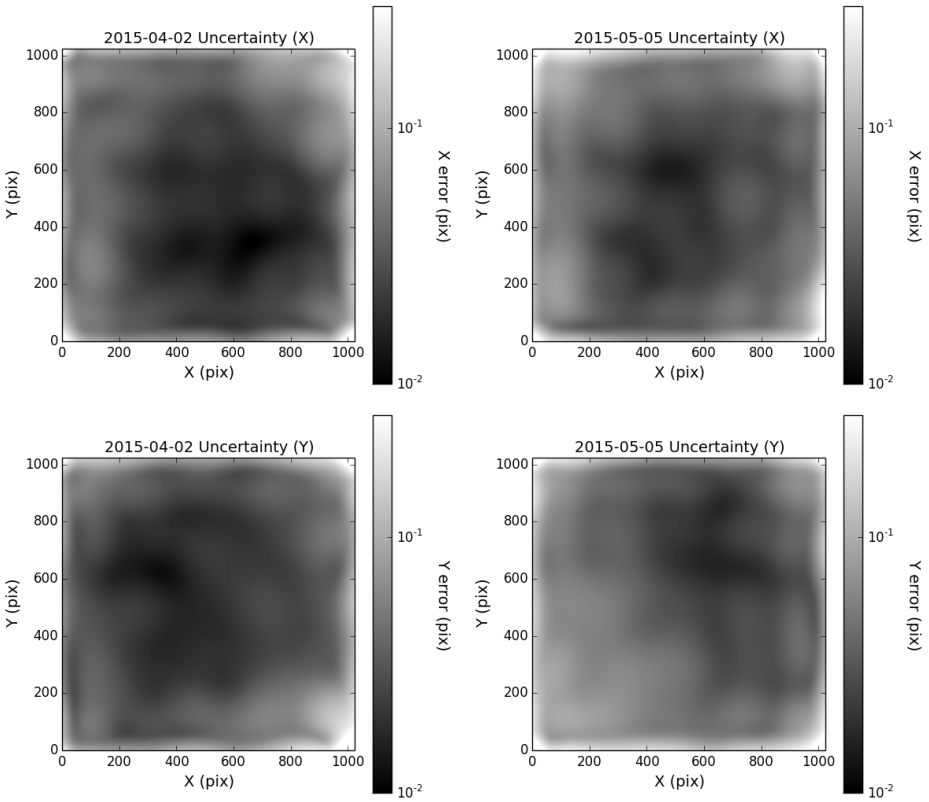


Figure 2.7 Fitting errors in the distortion solutions for 2015-04-02 (*left*) and 2015-05-05 (*right*) shown with log stretch. Spatial maps of the errors are shown for both the X (*top*) and Y (*bottom*) directions. The largest uncertainties are at the corners of the detector. The distribution of uncertainties for all pixels in the distortion model lookup table yield a mean uncertainty for the 2015-04-02 model of 0.42 pixels mas in both X and Y. The 2015-05-05 solution has mean uncertainties of 0.53 mas in X and 0.55 mas in Y. Note that an additional error of 1.0 mas must be added to the 2015-05-05 solution to fully describe the distortion measurement error.

find that the distortion changed by $\sim 0.45$ pixels (4.5 mas) rms due to the re-alignment of the AO bench.

### 2.6.1 Distortion Stability Prior to Realignment in 2015 April

The simplest test of our method is to verify that our April (pre-realignment) solution agrees with the previous solution. Figure 2.9 shows the differences between the solutions divided by the errors summed in quadrature. More than 90 % of the pixels agree within one sigma, therefore we measure no statistically significant differences between the Yelda et al. (2010)

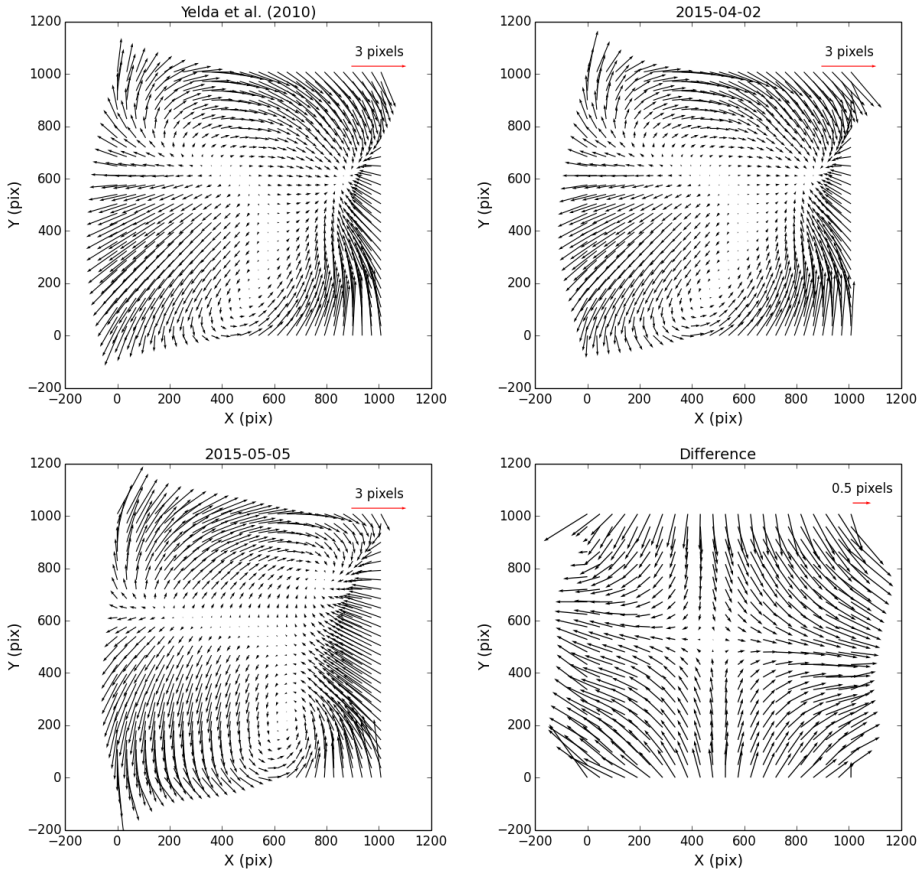


Figure 2.8 Top: Distortion models for the pre-realignment NIRC2 system. Arrows show the X and Y values that must be added to cancel the effects of geometric distortion. Left is the solution previously published in Yelda et al. (2010) and right is the solution derived using the methodology of this work. It is evident that these two are very similar and are, in fact, statistically equivalent. Bottom left: Distortion model derived from the May observations. Bottom right: Change of the optical distortion as a result of the optical realignment. This is the difference between the 2015-05-05 solution and the solution derived in Yelda et al. (2010). The average absolute value of the residual difference is $\sim$4.5 mas.

solution using imaging data from 2007-2009 and our pre-realignment solution. This verifies our method and confirms that the distortion seen by the NIRC2 camera is stable. To

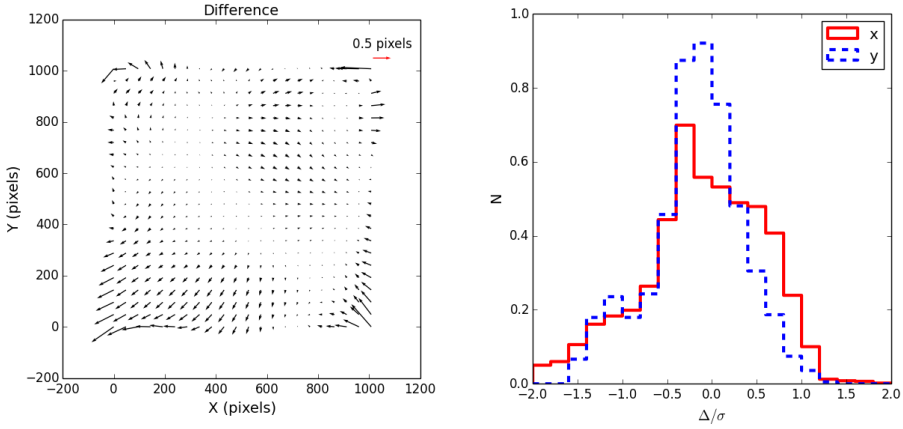


Figure 2.9 Difference between the previous solution (Yelda et al. 2010) and the pre-realignment 2015-04-02 solution from this work. The map of the vector differences (*left*) show the two solutions are consistent within 0.1 pixels over most of the field of view. Larger differences are seen in the corners. The distribution of differences normalized by the errors in each distortion solution is also shown (*right*). Errors include the fitting errors (figure 2.7) and the 1.0 mas additive term describing the residual distortion for both solutions. While the distribution is not exactly gaussian, more than 90% of the differences are within the $1\sigma$ ($\sim$ 1.4 mas) measurement errors.

confirm that the residual distortion in the two solutions are equivalent, we use our new fit to analyze two high precision Galactic center data sets taken on May 17 and May 20 2007. These data sets are of the central field around the Galactic center taken at P.A. of 0° and P.A of 200° at approximately the same central pointing (Yelda et al. (2010) section 3.2). We can use this data to measure the average residual distortion in the solution by comparing the measured positions of a single object at two different locations on the detector. The P.A. of 200° are transformed into the P.A. of 0° reference frame using a four parameter fit and then the average residual distortion is calculated using the differences between the stellar position measurements:

$$\sigma_x = \sqrt{\frac{1}{2}\sum_{i}^{N_{stars}} \frac{(\Delta_{x,i} - \langle\Delta_x\rangle)^2}{(N_{stars}-1)} - \frac{1}{2}(\sigma^2_{pos,0^\circ} + \sigma^2_{pos,200^\circ})} \tag{2.3}$$

Here $N_{stars}$ is the number of stars matched between the two data sets, $\sigma_{pos,0^\circ}$ and $\sigma_{pos,200^\circ}$ are the positional uncertainties for stars brighter than K magnitude of 14.5. We subtract the average positional uncertainties as they also contribute to the scatter ($\sigma_{0^\circ} \sim 0.13$ mas, $\sigma_{0^\circ} \sim 0.17$ mas). This results in an estimate of the average residual distortion in our new pre-realignment solution of 0.12 pixels in X and 0.10 pixels in Y. We can subtract the fitting error to find that our total unaccounted for residual distortion is 0.09 and 0.11 pixels for X and Y respectively in the 04-02-2015 solution. This is comparable to the measured final residual of the Yelda et al. (2010) solution which is 0.11 and 0.10 pixels for X and Y respectively. The extra systematic error is added in quadrature with the bootstrapped fitting errors to produce the final error maps for the new solution.

### 2.6.2 Quality of New 2015 May Distortion Solution

Unfortunately, we lack a similar external two-PA dataset to test the post-realignment solution as was used in Yelda et al. (2010) and the previous section. Instead, we apply our new (2015-05-05) solution to the May M53 NIRC2 imaging data. This is accomplished using *Drizzle* (Fruchter & Hook 2002). We then use *StarFinder* to extract positions from the individual corrected images and create a stack of position measurements for each star from all the available images. A four parameter transformation is used to map the catalogs to the common HST reference so they can be averaged. We adopt the mean scatter in the measured stellar positions as representative of the residual distortion in the solution. The mean rms scatter in the May position measurements for the 60 stars measured in at least 20 individual images is 1.1 mas in both X and Y. This 1.1 mas is the total error due to the combination of individual positional errors (figure 2.2), the fitting errors (figure 2.7) and the residual distortion. We subtract the average positional and fitting errors in quadrature which leaves 1.0 mas of residual distortion in the solution. Note that the total accuracy of the solution is the addition in quadrature of the residual distortion (1.0 mas) and the fitting error which varies across the detector. One source of this systematic error is PSF variability across the images frames, which will be addressed in a future analysis.

Table 2.2. NIRC2 Plate Scale and Orientation

| Data | Plate Scale (mas pixel$^{-1}$) | Orientation (degrees) |
|---|---|---|
| Yelda et al. (2010) | $9.952 \pm 0.002$ | $0.252 \pm 0.009$ |
| M53 - April | $9.954 \pm 0.002 \pm 0.001$ | $0.245 \pm 0.018 \pm 0.002$ |
| M53 - May | $9.971 \pm 0.004 \pm 0.001$ | $0.262 \pm 0.020 \pm 0.002$ |

### 2.6.3 Comparison of M53 positions

As a final consistency check between the two solutions, we can compare the final averaged distortion free positions for the stars in M53 as measured in the April and May data sets. We only include stars detected in at least 3 images in both data sets, which gives a total of 247 stars. We expect that the differences between the two position measurements should be consistent with the addition of the residual distortions from both solutions. The mean rms deviation is 1.1 mas for both x and y which is consistent with the measurement of the internal distortion for the May solution (that is the scatter of the position measurements from the May data). This is actually somewhat smaller than expected if both solutions have independent residual distortions of $\sim 1$ mas.

### 2.6.4 Changes in Plate Scale

The same matching of distortion corrected NIRC2 positions to the HST positions can also be used to to calculate the global plate scale and orientation in each data epoch (Table 2.2), as theses parameters were already fit to transform the coordinates. We estimate the scale and position angle relative to the HST reference frame for each of the distortion corrected NIRC2 image and average the results. This yields a global plate scale $\langle s \rangle = 9.971 \pm .004 \pm .001$ mas pixel$^{-1}$ post realignment and $\langle s \rangle = 9.952 \pm .002 \pm .001$ mas pixel$^{-1}$ pre-realignment. The first error is the rms of the measurements from the individual images and the second are the errors in the HST/ACS absolute reference frame (van der Marel et al. 2007).

### 2.6.5 Using the New Distortion Solution

Both the solutions and their associated errors are publicly available from the NIRC2 webpage[2]. The lookup tables present the distortion at the center of each NIRC2 pixel as well as the associated errors. This can be applied using existing programs (e.g. *Drizzle*) to correct distortion in NIRC2 data taken after April 13 2015.

## 2.7 Summary

We have derived a new model for the geometric distortion in observations obtained with the Keck NIRC2 narrow camera after 2015 April 13, when the optical system was re-aligned. The techniques used build on those of Yelda et al. (2010), with the primary advantage being a more robust basis set when fitting the distortion parameters and improved data quality. We verified that these technical differences do not significantly affect the derived models, and that we can recover the optical distortion of the system, pre-realignment, using the modified technique on a new data set. The Yelda et al. (2010) distortion solution should still be used for all pre-realignment data for the sake of consistency, as the pre-realignment solution from this work is statistically equivalent. The new post-realignment distortion solution (2015-05-05) should be used for all observations taken after 2015 April 13. The 2015-05-05 distortion solution along with associated errors are made publicly available[2], to assist with other astrometric projects using NIRC2. The systematic error in the new solution is dominated by the use of a single PSF for the entire field of view despite the fact it varies due to anisoplantatism and field-dependent wavefront error. This shortcoming will be addressed in future work using this dataset, with the primary advancement being the application of a spatially varying PSF in the position extraction from the individual science frames.

[2]https://www2.keck.hawaii.edu/inst/nirc2/dewarp.html

## 2.8 Acknowledgements

Some of the data presented herein were obtained at the W.M. Keck Observatory, which is operated as a scientific partnership among the California Institute of Technology, the University of California and the National Aeronautics and Space Administration. The Observatory was made possible by the generous financial support of the W.M. Keck Foundation. The authors wish to recognize and acknowledge the very significant cultural role and reverence that the summit of Mauna Kea has always had within the indigenous Hawaiian community. We are most fortunate to have the opportunity to conduct observations from this mountain.

# References


Anderson, J. 2007, Variation of the Distortion Solution of the WFC, Tech. rep.

Anderson, J. & King, I. R. 2006, PSFs, Photometry, and Astronomy for the ACS/WFC, Tech. rep.

Anderson, J., Sarajedini, A., Bedin, L. R., King, I. R., Piotto, G., Reid, I. N., Siegel, M., Majewski, S. R., Paust, N. E. Q., Aparicio, A., Milone, A. P., Chaboyer, B., & Rosenberg, A. 2008, AJ, 135, 2055

Bartko, H., Martins, F., Fritz, T. K., Genzel, R., Levin, Y., Perets, H. B., Paumard, T., Nayakshin, S., Gerhard, O., Alexander, T., Dodds-Eden, K., Eisenhauer, F., Gillessen, S., Mascetti, L., Ott, T., Perrin, G., Pfuhl, O., Reid, M. J., Rouan, D., Sternberg, A., & Trippe, S. 2009, ApJ, 697, 1741

Cameron, P. B. & Kulkarni, S. R. 2007a, in Bulletin of the American Astronomical Society, Vol. 39, American Astronomical Society Meeting Abstracts, 996

Cameron, P. B. & Kulkarni, S. R. 2007b, ApJ, 665, L135

Clarkson, W. I., Ghez, A. M., Morris, M. R., Lu, J. R., Stolte, A., McCrady, N., Do, T., & Yelda, S. 2012, ApJ, 751, 132

De Rosa, R. J., Nielsen, E. L., Blunt, S. C., Graham, J. R., Konopacky, Q. M., Marois, C., Pueyo, L., Rameau, J., Ryan, D. M., Wang, J. J., Bailey, V., Chontos, A., Fabrycky, D. C., Follette, K. B., Macintosh, B., Marchis, F., Ammons, S. M., Arriaga, P., Chilcote,

J. K., Cotten, T. H., Doyon, R., Duchêne, G., Esposito, T. M., Fitzgerald, M. P., Gerard, B., Goodsell, S. J., Greenbaum, A. Z., Hibon, P., Ingraham, P., Johnson-Groh, M., Kalas, P. G., Lafrenière, D., Maire, J., Metchev, S., Millar-Blanchaer, M. A., Morzinski, K. M., Oppenheimer, R., Patel, R. I., Patience, J. L., Perrin, M. D., Rajan, A., Rantakyrö, F. T., Ruffio, J.-B., Schneider, A. C., Sivaramakrishnan, A., Song, I., Tran, D., Vasisht, G., Ward-Duong, K., & Wolff, S. G. 2015, ApJ, 814, L3

Diolaiti, E., Bendinelli, O., Bonaccini, D., Close, L. M., Currie, D. G., & Parmeggiani, G. 2000, StarFinder: A code for stellar field analysis, Astrophysics Source Code Library

Dupuy, T. J., Liu, M. C., & Ireland, M. J. 2014, ApJ, 790, 133

Eckart, A. & Genzel, R. 1997, MNRAS, 284, 576

Fruchter, A. S. & Hook, R. N. 2002, PASP, 114, 144

Genzel, R., Schödel, R., Ott, T., Eisenhauer, F., Hofmann, R., Lehnert, M., Eckart, A., Alexander, T., Sternberg, A., Lenzen, R., Clénet, Y., Lacombe, F., Rouan, D., Renzini, A., & Tacconi-Garman, L. E. 2003, ApJ, 594, 812

Ghez, A. M., Klein, B. L., Morris, M., & Becklin, E. E. 1998, ApJ, 509, 678

Ghez, A. M., Salim, S., Hornstein, S. D., Tanner, A., Lu, J. R., Morris, M., Becklin, E. E., & Duchêne, G. 2005, ApJ, 620, 744

Grundy, W. M., Porter, S. B., Benecchi, S. D., Roe, H. G., Noll, K. S., Trujillo, C. A., Thirouin, A., Stansberry, J. A., Barker, E., & Levison, H. F. 2015, Icarus, 257, 130

Gubler, J. & Tytler, D. 1998, PASP, 110, 738

Kharchenko, N. V., Piskunov, A. E., Schilbach, E., Röser, S., & Scholz, R.-D. 2013, A&A, 558, A53

Kimmig, B., Seth, A., Ivans, I. I., Strader, J., Caldwell, N., Anderton, T., & Gregersen, D. 2015, AJ, 149, 53

Konopacky, Q. M., Ghez, A. M., Duchêne, G., McCabe, C., & Macintosh, B. A. 2007, AJ, 133, 2008

Liu, M. C., Dupuy, T. J., & Ireland, M. J. 2008, ApJ, 689, 436

Lu, J. R. 2008, PhD thesis, UCLA

Lu, J. R., Ghez, A. M., Hornstein, S. D., Morris, M. R., Becklin, E. E., & Matthews, K. 2009, ApJ, 690, 1463

Meyer, L., Ghez, A. M., Schödel, R., Yelda, S., Boehle, A., Lu, J. R., Do, T., Morris, M. R., Becklin, E. E., & Matthews, K. 2012, Science, 338, 84

Paumard, T., Genzel, R., Martins, F., Nayakshin, S., Beloborodov, A. M., Levin, Y., Trippe, S., Eisenhauer, F., Ott, T., Gillessen, S., Abuter, R., Cuadra, J., Alexander, T., & Sternberg, A. 2006, ApJ, 643, 1011

Pueyo, L., Soummer, R., Hoffmann, J., Oppenheimer, R., Graham, J. R., Zimmerman, N., Zhai, C., Wallace, J. K., Vescelus, F., Veicht, A., Vasisht, G., Truong, T., Sivaramakrishnan, A., Shao, M., Roberts, Jr., L. C., Roberts, J. E., Rice, E., Parry, I. R., Nilsson, R., Lockhart, T., Ligon, E. R., King, D., Hinkley, S., Hillenbrand, L., Hale, D., Dekany, R., Crepp, J. R., Cady, E., Burruss, R., Brenner, D., Beichman, C., & Baranec, C. 2015, ApJ, 803, 31

Rudy, A., Horns, D., DeLuca, A., Kolodziejczak, J., Tennant, A., Yuan, Y., Buehler, R., Arons, J., Blandford, R., Caraveo, P., Costa, E., Funk, S., Hays, E., Lobanov, A., Max, C., Mayer, M., Mignani, R., O'Dell, S. L., Romani, R., Tavani, M., & Weisskopf, M. C. 2015, ApJ, 811, 24

Service, M., Lu, J. R., Campbell, R., Sitarski, B. N., Ghez, A. M., & Anderson, J. 2016, Publications of the Astronomical Society of the Pacific, 128, 095004

Stolte, A., Ghez, A. M., Morris, M., Lu, J. R., Brandner, W., & Matthews, K. 2008, ApJ, 675, 1278

van der Marel, R. P., Anderson, J., Cox, C., Kozhurina-Platais, V., Lallo, M., & Nelan, E. 2007, Calibration of ACS/WFC Absolute Scale and Rotation for Use in creation of a JWST Astrometric Reference Field, Tech. rep.

Yelda, S., Ghez, A. M., Lu, J. R., Do, T., Meyer, L., Morris, M. R., & Matthews, K. 2014, ApJ, 783, 131

Yelda, S., Lu, J. R., Ghez, A. M., Clarkson, W., Anderson, J., Do, T., & Matthews, K. 2010, ApJ, 725, 331

# Chapter 3

# Geometric Distortion Calibration with Photo-lithographic Pinhole Masks for High-Precision Astrometry

Note: This chapter was originally published as Service et al. (2019) with coauthors Jessica R. Lu, Mark Chun, Ryuiji Suzuki, Matthias Schoeck, Jenny Atwood, David Andersen and Glen Herriot.

## 3.1 Abstract

Adaptive optics (AO) systems deliver high-resolution images that may be ideal for precisely measuring positions of stars (i.e. astrometry) if the system has stable and well-calibrated geometric optical distortions. A calibration unit, equipped with back-illuminated pinhole mask, can be utilized to measure instrumental optical distortions. AO systems on the largest ground-based telescopes, such as the W. M. Keck Observatory and the Thirty Meter Telescope require pinhole positions known to ∼20 nm to achieve an astrometric precision of 0.001 of a resolution element. In pursuit of that goal, we characterize a photo-lithographic pinhole mask and explore the systematic errors that result from different experimental setups. We characterized the nonlinear geometric distortion of a simple imaging system using the mask; and we measured 857 nm RMS (root mean square) of optical distortion

with a final residual of 39 nm (equivalent to 20 $\mu$as for TMT). We use a sixth order bivariate Legendre polynomial to model the optical distortion and allow the reference positions of the individual pinholes to vary. The nonlinear deviations in the pinhole pattern with respect to the manufacturing design of a square pattern are 47.2 nm $\pm$ 4.5 nm (random) $\pm$ 10.8 nm (systematic) over an area of 1788 mm$^2$. These deviations reflect the additional error induced when assuming the pinhole mask is manufactured perfectly square. We also find that ordered mask distortions are significantly more difficult to characterize than random mask distortions as the ordered distortions can alias into optical camera distortion. Future design simulations for astrometric calibration units should include ordered mask distortions. We conclude that photo-lithographic pinhole masks are $> 10$ times better than the pinhole masks deployed in first generation AO systems and are sufficient to meet the distortion calibration requirements for the upcoming thirty meter class telescopes.

## 3.2 Introduction

Precise astrometric measurements from have enabled scientific results across a variety of fields. This includes studies of stellar clusters that utilized proper motions to identify members and study dynamical structure Massari et al. (2015); Hosek et al. (2015); Platais et al. (2018), orbital measurements of nearby binaries of low mass stars and exoplanets Rodet et al. (2018); Best et al. (2017); Wertz et al. (2017); Konopacky et al. (2016); Dupuy et al. (2018), and orbital measurements of the stars at the Galactic Center Ghez et al. (2008); Lu et al. (2009). These science cases require sub-milliarcsecond precision, which is typically $10-100\times$ smaller than the intrinsic geometric distortion in the instrument so, the distortion must be measured and corrected for each instrument.

The best current distortion calibrations for astronomical instruments use observations of crowded stellar fields to simultaneously solve for the static optical distortions of the imaging system and the intrinsic on-sky positions of each starAnderson & King (2003); Lindegren et al. (2018). This technique, often referred to as the self-calibration method, requires

translating and rotating the pointing of the telescope many times in order to move the stellar cluster across the field of view and constrain all possible distortion modes Anderson & King (2003). Self-calibration can also be applied to a calibration unit using artificial sources as long as the astrometric reference positions can be rotated and translated. A self calibration method that included time variation was adopted for Gaia Data Release 2 (DR2), which delivered an absolute astrometric calibration with uncertainties of $<0.04$ mas for the brightest sources Lindegren et al. (2018). The high precision of the self-calibration method results from the quantity and diversity in the data, which cannot easily be replicated for all astronomical imaging systems as the observing time commitment is too large. Instead, most ground-based instruments adopt an external set of calibrated stellar positions (generally *Hubble Space Telescope* (HST) or Gaia positions) as distortion free and model the distortion as the difference between measured positions and the external catalog Yelda et al. (2010); Service et al. (2016); Maire et al. (2016); Massari et al. (2016). This approach still requires observing time to measure the stellar field, but it is greatly reduced from the requirements of a full self-calibration.

The requirement of using on sky observations for distortion calibration could be eliminated by using an internal astrometric flat field to measure the distortion. A natural candidate for this astrometric flat field is a pinhole mask with a regular grid of holes at precisely known positions. This is not a new idea; however, previous attempts have failed to match the accuracy that can be reached using images of star fields. For example, the first distortion maps for the Near Infrared Camera (NIRC2) instrument at the W.M Keck Observatory were measured using pinhole masks Cameron & Kulkarni (2007); but, these solutions had residual distortion $>2$ mas as compared to 1 mas residuals from solutions derived with globular clusters Yelda et al. (2010); Service et al. (2016).

More recently, the distortion of the Gemini Planet Imager was calibrated using a combination of a pinhole mask with unknown hole positions combined with the self-calibration method Konopacky et al. (2014). They achieved a distortion residual of 0.56 mas over a $2.67'' \times 2.73''$ field of view. The improvement in distortion measurement over

previous attempts was due to the use of the self-calibration method, not improvement in the manufacturing precision of the mask. This approach requires a translation and rotation stage in the calibration unit, which is not always feasible; however it's worth noting that even large manufacturing errors can be mitigated with this method.

The quality of available pinhole masks determines the optimal design for a given instrument calibration unit. If the residual pattern errors (mask distortion) in the mask are less than the required distortion calibration precision, one can adopt the manufactured pattern as the "distortion free" reference and simply accept that there will be residual distortion in the final solution due to the ignored error. This can be achieved either by accurately manufacturing the mask pattern or by measuring the mask distortion before it is installed in the calibration unit. An accurate known astrometric flat field greatly relaxes the functional requirements for the system, as a rotation and translation stage is no longer required. It would also greatly reduce the amount of observing time required to measure the distortion, which is particularly important if the calibration has to be repeated to account for variations in the instrument. One drawback is that distortion solutions measured using an internal mask would be blind to optical distortion in the telescope itself, however the distortion in most high resolution AO fed astronomical cases is dominated by the distortion intrinsic to the instrument. For example, comparison of models and the measured on-sky distortion solution for the Gemini muti-conjugate adaptive optics system (GeMS) demonstrated that the optical distortion is dominated by the AO system.Patti & Fiorentino (2019). This is consistent with the distortion estimates based on the Zemax optical prescription for NIRC2 which shows that the AO relay contributes 10000 times more distortion than the telescope over a 14" $\times$ 14" field of view.

The goal of this work is to understand the error contribution to a final distortion calibration due to manufacturing errors in a reference pinhole mask and the distortion measurements errors induced by the calibration procedure, as this directly informs the design of future calibration units. We specifically focus on potential applications to the first-light Narrow-Field Infrared Adaptive Optics System (NFIRAOS) at the Thirty Meter

Telescope (TMT) Herriot et al. (2014) and the narrow field mode of the infrared camera (NIRC2) at the W. M. Keck Observatory. Using a prototype pinhole mask provided by NRC Herzberg, we quantify the deviation of the pattern of pinholes with respect to a perfect square pattern. For TMT, the final requirement for the total astrometric error budget is less than 10 $\mu$as, which means that the residual distortion must be much smaller. This converts to a physical size of 20 nm at the telescope focal plane inside NFIRAOS. Similarly for Keck NIRC2, the residual distortion due to manufacturing errors must be significantly smaller than current distortion calibration residual of 270 nm or 1.0 mas Service et al. (2016). If the mask pattern is accurate to the 20 nm level, then a calibration unit for either TMT NFIRAOS or Keck NIRC2 could be completely static.

We present results from both a laboratory experiment and simulations that show that the required astrometric calibration precision can be achieved using current pinhole masks and small dithers and rotations. §3.3 describes the experimental setup, §3.4 describes the observations obtained, and §3.5 describes the analysis procedures employed to extract pinhole positions and fit distortions. In §3.6, we present a set of simulations that reproduce the experimental results and are extended to explore the impact of different dithering and rotation schemes during calibration and to show the sensitivity to manufacturing errors in the pinhole mask. Finally, in §3.7, we discuss how our results effect the design of future distortion calibration units.

## 3.3 Experimental Setup

A lab experiment was designed to measure the accuracy of the pinhole mask hole positions and sizes. The lab setup consists of a light source (organic light emitting diode (OLED) cell phone screen) illuminating the pinhole mask, which is then imaged using a low-distortion field lens on to a large-format optical camera as shown in Figure 3.1. The pinhole mask was mounted parallel to the lab bench with a simple three point mount on a rotation stage, and a flat mirror was used to fold the beam into the lens. The lens is an Apo-Ronar process

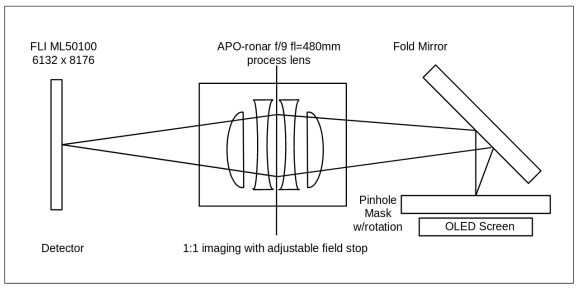


Figure 3.1 Diagram showing the lab setup used to image the pinhole mask.

lens with a 480 mm focal length designed for low distortion 1:1 imaging when used at $f/9$. We used a Finger Lake Imaging (FLI) CCD camera (model ML50100) with a 8176 $\times$ 6132-element detector with 6 $\mu$m pixels (61.2 mm diagonal) and a quantum efficiency (QE) $>$ 30 % from 360 nm to 800 with a peak of 60% at 540 nm.

The pinhole mask is a prototype obtained from NRC-Herzberg and the TMT NFIRAOS project produced by Advance Reproduction using photo-lithographic techniques by Advance Reproduction in chrome on a fused silica wafer. The mask was made on a 125 mm diameter Quartz wafer with a chrome on nickel coating that has an optical depth of 3. In addition there is a coating of *Advance Polyguard*, which is a thin transparent film with anti-wetting, anti-stiction and anti-migration properties. The mask has 4 different pinhole diameters (12, 24, 56 and 120 $\mu$m) situated in a 86$\times$86 square pattern with 1 mm spacing between each pinhole and an expected tolerance on the diameter of $<$ 0.3 $\mu$m. When imaging the small (12$\mu$m and 24 $\mu$m) pinholes, we found that there was a systematic position measurement error of $\sim$ 100 nm, which we attribute to small scale detector defects. As a result we used the 56 micron pinholes for this work; an example image is shown in Figure 3.2 As this experiment is done using visible light, there is background transmission of $\sim$ 1% between the pinholes.

There were 2 different experiments conducted with this setup: (1) obtain multiple images of the pinhole mask without dithering to analyze the measurement precision and stability over time, and (2) dither the pinhole mask to derive the optical distortion and the pinhole positions simultaneously without assuming the pinhole pattern is perfectly square (self-

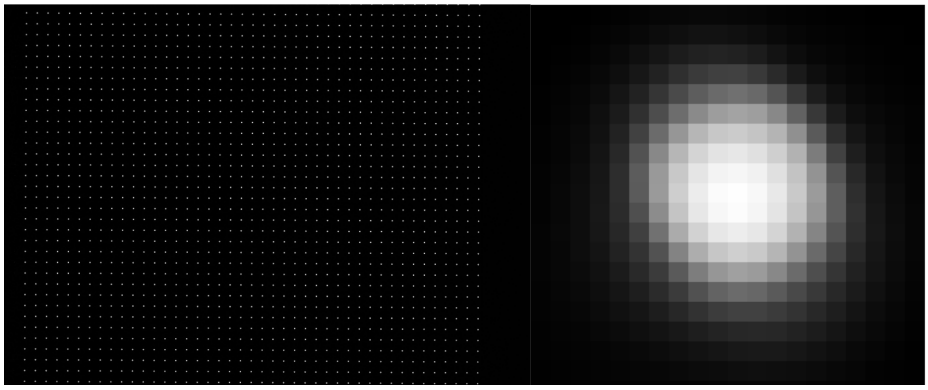

Figure 3.2 *Left:* Example FLI CCD image of the 56 $\mu$m-sized pinholes which were used to measure the optical distortion in this setup. The size of the image on the left is 46 mm $\times$ 35 mm *Right:* The spot shape or PSF empirically determined for this image using *StarFinder* as discussed in section 3. The PSF cutout is 0.12 mm on each side and has a linear intensity stretch.

calibration method). For the second experiment we consider 6 mask positions that are spaced equidistantly around a unit circle. The rotation stage is displaced from the center of the detector by $\sim$3.5mm in both axes, so rotating the mask serves to both rotate and translate the pattern with respect to the detector. We only consider positions from pinholes that are in at least 3 of the 6 locations, which eliminates 61 pinholes leaving a total of 1788 pinholes sources used.

For images at a single mask position, both optical distortions and irregular pinhole positions will manifest as deviations from a regular grid and we cannot distinguish between the two sources. However, the optical distortions are static with respect to the camera; thus, moving the mask with respect to the camera allow us to separate optical distortions from pinhole irregularities. For the final analysis, data is taken after rotating the pinhole grid to separate mask distortion and camera (optical) distortion.

## 3.4 Observations and Data

The observations are summarized in Table 4.1 and consists of 6 stacks of images taken with the mask rotated to a different position for each stack as shown in Figure 3.3. Each rotation

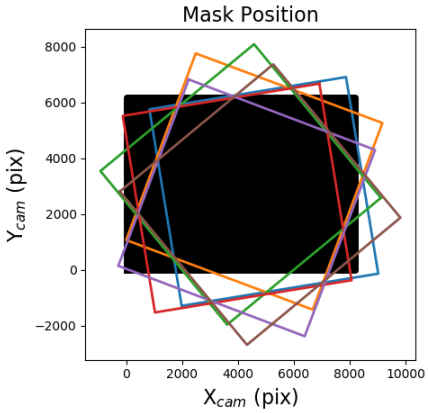


Figure 3.3 Positions of the pinhole pattern with respect to the camera detector. The shaded black region shows the detector and colored squares show the outline of the pinhole pattern for each of the 6 locations the mask was observed. The images were taken with a plate scale of 6 microns per pixel and the axis of rotation of the mask is offset from the center of the detector by 3.5 mm.

position was imaged once with a total of 100×0.3 s exposures. The axis of rotation is offset from the center of the detector by approximately 3.5 mm in both axis.

Raw images were dark subtracted and flat field corrected. The flat field was measured using images taken with the illumination on and pinhole mask removed from the system. Each image was then run through a source extraction procedure to identify the pinhole images and measure their positions and fluxes. The source extraction is performed using the point spread function (PSF) fitting routine, *StarFinder* Diolaiti et al. (2000) with a PSF box size of 20 pixels. The PSF is determined empirically from the data and is the average of all sources in a 2000 pixel box centered on the detector. The output of *StarFinder* is a catalog of pinhole positions and fluxes in raw detector coordinates for each image. These output catalogs will be the input for the averaging and model fitting in the next sections.

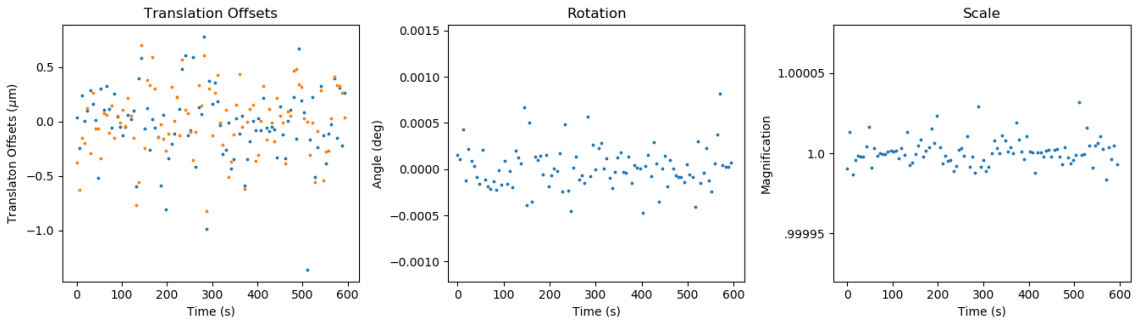


Figure 3.4 Variation in computed 4-parameter transformation coefficients for each of the catalogs derived from the 100 exposures. The translation and rotation drift are consistent with motion in the rotation stage, while the variation in the scale is much smaller and is likely due to instabilities in the optics. The pixel size is 6 $\mu m$ and a rotation of 0.0001 degrees corresponds to a tangential motion of 110 nm at the edge of the rotation stage.

## 3.5 Experimental Analysis

### 3.5.1 Stability

Before trying to separate true optical distortion from possible errors in the mask, we must first understand the stability of the setup at a single mask location. We analyze the variation of the position measurements in a stack of catalogs derived from images taken with the mask at a fixed location. This analysis does not constrain the optical distortion in the system; it only estimates the experimental stability. For this test we use a stack 100 source catalogs with 1493 detected images of the 56 micron pinholes. We test the stability by verifying that the scatter in the measured mean position decreases as a function of the number of frames used in the mean. The stack of catalogs are split into N groups with M catalogs, and the mean position is computed for each group. Then the RMS deviation and the Allan deviation is calculated for the N groups of position measurements. If the scatter in the position measurements is due to random errors, than the scatter should be proportional to $N^{-0.5}$. When this test is performed with only the mean translations eliminated, the RMS deviation does not decrease as a function of N, which implies that there is significant variation in the scale and rotation of the images as seen in Figure 3.4. When we increase

the complexity of the transformation to include the scale, rotation and translations (4 parameters) than the scatter in the measured positions decreases as $N^{-0.5}$.

The four parameter fits are performed iteratively, by first averaging all the catalogs with only translation removed to create the first set of reference coordinates, and then fitting a new four parameter transformation between each catalog and these reference coordinates. The new transformed coordinates are then averaged to create a new reference and the fitting procedure is repeated a final time. The resulting corrected positions show the expected behavior in the scatter as a function of the number of measurements averaged (Figure 3.5). Given these results, we remove the linear parameters and then average over the coordinates in each stack and take the error on the mean as the measurement uncertainty. We produce one stack-catalog per dither and rotation position and use the stack-catalogs going forward.

The averaged positions of the 100 catalogs at each position of the mask will be used to measure the optical distortion of the setup (camera distortion) and the position of the pinholes on the mask (mask distortion) as described in the following sections.

### 3.5.2 Distortion Models

In order to constrain the camera distortion, the mask distortion, and control for experimental instabilities, we fit a 3-component model to the stack-catalogs from all the dither and rotation positions simultaneously. he dither position coordinates are listed in the last 3 columns of Table 4.1. We define two coordinate systems,

$$x_c, y_c \quad \text{camera coordinates}$$

$$x_m, y_m \quad \text{mask coordinates}$$

where we adopt a uniform square grid of pinholes with a pitch of 166.7 camera pixels as our mask coordinate frame. The camera coordinates are an idealized distortion free coordinate frame that is defined with respect to the detector pixels.

The three components of the model include the following. First, there is

$$\begin{aligned} x_c &= D_{x,camera}(x'_c, y'_c) \\ y_c &= D_{y,camera}(x'_c, y'_c) \end{aligned} \tag{3.1}$$

where

$$D_{camera}(d, x'_c, y'_c) = \sum_{i=0}^{R} \sum_{j=0}^{R} d_{ij} L_i(x_c) L_j(y_c) \tag{3.2}$$

which defines is the transformation from distorted camera coordinates$(x'_c, y'_c)$ to distortion free coordinates $(x_c, y_c)$. Here $L_i$ is the $i^{\text{th}}$ normalized Legendre Polynomial and $R$ is the order of the distortion model which is 6 in this work. When this function is evaluated, the arguments are normalized to lie on the interval from -1 to 1. This model does not include the linear parameters $(i + j < 1)$ as those are included in the second component of this model. Second, there is

$$\begin{aligned} x_c &= l(x_m, y_m) = c_0 + c_1 x_m + c_2 y_m \\ y_c &= l(x_m, y_m) = c_3 + c_4 x_m + c_5 y_m \end{aligned} \tag{3.3}$$

which defines a linear transformation to go from the mask coordinate frame ($x_m$,$y_m$) to distortion corrected positions in the camera coordinate frame. As the mask is rotated on the detector, these linear parameters are different for every stacked catalog. Third, there is the mask distortion,

$$\begin{aligned} D_{x,mask}(x_{square}) &= x_m + \delta_x \\ D_{y,mask}(y_{square}) &= y_m + \delta_y \end{aligned} \tag{3.4}$$

where $x_m$ $(y_m)$ are the original uniform grid of pinhole positions, and $\delta_x$ $(\delta_y)$ are the differences between the uniform grid and the true pinhole positions. The correct pinhole

defined as

$$\begin{aligned} x_{pin} &= D_{x,mask}(x_m) \\ y_{pin} &= D_{y,mask}(y_m) \end{aligned} \tag{3.5}$$

where $x_{pin}$ and $y_{pin}$ are the true pinhole positions on the mask. To fit this model, we must specify all three model components. This is done in an iterative fashion, where we start by assuming $\delta_x$ and $\delta_y$ are zero and fitting the first two model components using a Levenberg-Marquardt to simultaneously fit for the $d$ and $c$ coefficients. To do this we use the measured coordinates from each stack catalog as $x'_c$ and $y'_c$ and minimize $\Delta$

$$\begin{aligned} \Delta_x &= \sum_{n=0}^{N-1} [l(c_n, x_{pin}, y_{pin}) - (D_{\mathrm{x,camera}}(d, x'_{c,n}, y'_{c,n}))]^2 \\ \Delta_y &= \sum_{n=0}^{N-1} [l(c_n, x_{pin}, y_{pin}) - (D_{\mathrm{y,camera}}(d, x'_{c,n}, y'_{c,n}))]^2 \end{aligned} \tag{3.6}$$

where N is the total number of catalogs (6) and $n$ denotes the $n^{th}$ catalog. Note that there are separate linear parameters ($c$) for each of the $n$ catalog, which gives a total of 134 free parameters. After the camera distortion and linear parameters have been fit, we update the model of the mask distortion. This is done by applying the current best model of the camera distortion to the measured positions and inverting the linear equations (equation 3.3) to transform those distortion corrected positions into the mask coordinate frame. The mask distortion is then corrected as

$$\begin{aligned} \delta_x &= \bar{x}'_m - x_m \\ \delta_y &= \bar{y}'_m - y_m \end{aligned} \tag{3.7}$$

where $\bar{x}'_m$ and $\bar{y}'_m$ are the average of the distortion corrected measured positions in the mask reference frame. After updating the model for the pinhole positions, the camera distortion model and the linear parameters must be fit again. This fitting procedure is then repeated with the new values for $\delta$ for 4 iterations, when the change in the mask distortion model

Table 3.1. Data Summary

| Date | Position | $N_{sources}$ | $N_{exp}$ | $T_{exp}$ (s) | $\sigma_x$(nm) | $\sigma_y$ (nm) | Angle (deg) | $\Delta_x$ (mm) | $\Delta_y$ (mm) |
|---|---|---|---|---|---|---|---|---|---|
| 01-05-2019 | 0 | 1353 | 100 | 0.3 | 9.9 | 10.1 | 10 | 0 | 0 |
| 01-05-2019 | 1 | 1373 | 100 | 0.3 | 11.8 | 12.5 | 70 | 4 | 1.6 |
| 01-05-2019 | 2 | 1346 | 100 | 0.3 | 7.6 | 8.0 | 130 | 4.6 | 5.9 |
| 01-05-2019 | 3 | 1372 | 100 | 0.3 | 7.6 | 8.1 | 190 | 1.3 | 8.5 |
| 01-05-2019 | 4 | 1337 | 100 | 0.3 | 8.0 | 9.7 | 250 | -2.7 | 6.9 |
| 01-05-2019 | 5 | 1312 | 100 | 0.3 | 8.9 | 8.9 | 310 | -3.3 | 2.7 |

is $< 20$ nm. Note that the linear transformations in this model mean that this analysis is entirely blind to linear modes of camera and mask distortion. The linear transformations are required to eliminate the variation seen in the optical system between measurements of the different pinhole mask positions as shown in Figure 3.6.

### 3.5.3 Estimated Distortion Precision

Our best fit has a 5-$\sigma$ clipped RMS residual of 39.5 in X and 38.5 nm in Y. These residuals are a combination of the positional measurement error and the residual optical distortion with order $> 6$. We estimate the residual high order distortion as the total fit residual subtracted by the position measurement errors in quadrature (37.8 nm). Table 2 summarizes the contributions to the total position displacements in the system, which are the optical camera distortion, the mask distortion, the position measurement error and the residual optical distortion. Figure 3.7 shows the best fit models for the camera and mask distortion. The size of the camera distortion is consistent with the manufacturer's specification of less than 0.01% distortion. Mask distortion is estimated to be 47.2 nm RMS, which would limit the accuracy of distortion measurements using this mask if it is not pre-calibrated. This sets the expected floor for distortion measurements carried out using other similar masks assuming the new mask was not independently calibrated. The spatial coherence in the fit residuals seen in Figure 3.8 suggests that the uncorrected high order optical distortion is a significant contributor to the fit residual. High spatial frequency defects in the detector could also be contributing to the remaining residual.

Table 3.2. Deviation Budget

| Source | Size (nm) | Size TMT ($\mu$as) |
|---|---|---|
| Total Nonlinear Deviations | 858 | 429 |
| Optical Distortion $\mathcal{O}$(2-6) | 856 | 300 |
| Pinhole Mask Distortion | 47.2 $\pm$4.5 $\pm$11 | 23.6 |
| Measurement Precision | 9.2 | 4.6 |
| Uncorrected high order distortion $\mathcal{O}$(¿6) | 37.8 | 18.9 |

It is worth noting that environmental instability in the system could contribute to the residual term that we attribute to residual high order distortion. For example, if there is a changing temperature gradient on the pinhole mask during the observations, it would alter the mask distortion pattern between different mask positions. As we assume a static mask distortion, this change would increase the residual in the fit. This is generally true for any instability which changes the mask or camera distortion in a non-linear fashion during the experiment. Note that if the temperature of the entire mask changes then there would be no change in the mask distortion, as the expansion only effects the linear terms in the mask distortion which are eliminated in our model.

## 3.6 Simulations

In order to evaluate the measurement error in the mask distortion we must understand how effective the self-calibration method was in this case. The aim of self-calibration is to correctly identify the deviations due to the mask distortion and the deviations due to the camera distortion. Self calibration approaches have been widely implemented for non-astronomical imaging systems and have been found to have significant degeneracy between the fit parameters. For example, Strum et. al. studied the degenerate solutions in a model of the 5 intrinsic camera parameters and discovered a certain class of camera moves where there are multiple solutions for the focal length. The same problem applies for the more complicated models of optical distortion, where there are multiple combinations of mask distortion and optical distortion which fit the data equally wellSturm (2000). This

is a general problem for camera self calibration techniques, that has been explored in the specific case of radial distortion Brito et al. (2013); Wu (2014). As our model includes both radial and tangential optical distortion their results only reflect a subset of the degenerate cases that could be present in our system. Brito et. al. note that pure translation in the XY plane fails to accurately recover the radial distortionBrito et al. (2013), which is consistent with the simulated results in this section and others have found a number of other possible motions with more than one valid distortion solution.Wu (2014) Another important case those authors notes is that rotation about the optical axis is degenerate, however, rotation about any other point is not. As the cases in the literature differ substantially from our setup, and the size of the error depends on the strength of the distortion, we choose to simulate our optical setup to estimate the systematic errors in the measured mask distortion.

The simulations presented here use two distinct starting points (1) a realistic set of inputs which match the best fit measurements for the mask and camera distortion from the real data (Figure 3.9) and (2) a worst case scenario where the optical distortion is set to zero while the total distortion in the system is applied as mask distortion (Figure 3.10). The second set of inputs is not realistic, however it maximizes the error in recovery because if a given deviation can be fit as either mask distortion or camera distortion it will be measured as camera distortion. We use the first simulation to estimate the random errors in the mask distortion and the second simulation to estimate the systematic error due to mask deviations being incorrectly characterized as optical distortion.

### 3.6.1 Accuracy of the Measured Mask Distortion

Using those two sets of inputs, we first create a simulation to replicate the actual lab experiment using simulated catalogs instead of the real data to estimate the error in the mask distortion measurement. To create the simulated observations the best fit mask distortion is applied to a perfectly square grid of points to create a set of simulated mask coordinates. We then use the same linear parameters from the best fit to transform the simulated mask coordinates into the camera coordinate frame, apply the best fit model of

the distortion as a function of the camera coordinates and add Gaussian noise consistent with the measurement errors in Table 4.1. This gives 6 simulated measured catalogs of the pinhole mask that match the 6 real observations in the lab. The simulated data is then fit with the same model described in Section 3.5, and the mask deviation is recovered with an accuracy of 4.5 nm RMS as shown in Figure 3.9. We adopt this value as the random component of the error in the measurement of the mask distortion.

Now we repeat that simulation and analysis; however, instead of using the realistic inputs for both the camera and mask distortion, we instead apply only a mask distortion with an amplitude equal to 858 nm, which is equivalent to the combined mask+camera distortion in the previous simulation. We derive a suitable model for mask-only distortion by first fitting a $6^{\text{th}}$ order Legendre Polynomial to the difference between the measured catalog positions at mask position 0 and a regular square grid. The resulting input mask-only distortion pattern is plotted in the middle panel of Figure 3.10, and it is worth emphasizing that this input does not match expectations for our optical system as the lens is specified to have $\sim$1000 nm of optical distortion over this field. However, as a conservative constraint, we use this simulation to estimate the level of systematic error due to misidentifying some of the mask distortion as camera distortion. The recovery error is influenced by the outlier points in the lower right corner, so we apply a $5\sigma$ clip to the residuals before calculating statistics. This results in a systematic mask distortion recovery error of 200 nm when the input mask distortion had a total size of 858 nm RMS. Note that there is an even larger mistake in the recovery of the camera distortion, which should be zero, for this simulation, as seen in the PSD of the deviations shown in Figure 3.10.

Based on the results from this simulation, we estimate a fractional error of 23% on the mask distortion, which we adopt as the systematic error for the measurement of the mask distortion. This corresponds to an additional 10.8 nm of error in the measurement of the mask distortion pattern.

This estimate of the systematic error assumes that the total deviations represent the maximum distortion on the mask or in the camera. However, there is one case that this

approach does not account for. Specifically, as we chose to only rotate the pinhole mask, radial modes of optical distortion that are centered on our axis of rotation can be modeled as either mask or optical distortion. In the case that there is both a large radial mode of camera distortion centered on the axis of rotation and the opposite mode in the mask distortion they would cancel and not appear in the total deviations, which would lead to an underestimation of the systematic error. An ideal calibration unit should have both a rotation and translation stage in order to correctly constrain all modes of distortion.

### 3.6.2 Accuracy of the Self-calibration Method

We can extend this simulation approach to a wider variety of mask dither patterns in the calibration procedure. This is useful as it demonstrates a few simple cases of how the effectiveness of the self calibration approach depends sensitively on how the pinhole mask is moved. For these simulations we adopt a 150 nm RMS of mask distortion and 858 nm RMS of camera distortion as shown in Figures 3.7 and 3.11. Then we simulate a variety of dither patterns of the mask. Here we rotate the mask about the center of the detector and translate the mask in a $N_{step}$ by $N_{step}$ square pattern at each of the $N_{rot}$ rotation angles, such that there are $N_{step}^2$ measured catalogs for each rotation position. The translation step size is the spacing between each one of the translation positions of the mask. These simulations do not include random measurement errors of any kind.

The results for different mask dither patterns are shown in Table 3.6.2, cases 1-5. Column 7 lists the RMS difference between the input mask distortion and the mask distortion recovered by the full fit, which corresponds to the systematic error in the mask distortion measurement due to the chosen dither pattern of the pinhole mask. Column 8 lists the residual distortion after the full model is fit. Simulation cases 3-5 shows that translation-only dithers mis-identify 95% of the input mask distortion as camera distortion.

This degeneracy between mask distortion and camera distortion occurs when the scale between each data set is allowed to vary, which causes aliasing of the mask distortion into camera distortion space. Appendix 1 demonstrates this effect in detail using a 1D example.

In principle, if the scale is known to be very stable, then it can be fixed in the model, breaking this degeneracy. To test the effect of scale variation in the system when scale variation is not allowed in the model, we run a final simulation. We use the same inputs as simulation case 3, except we add in scale variation for each of the 9 measured catalogs drawn from a normal distribution centered on a scale of 1.0 with a standard deviation of $10^{-5}$. When we fit this simulation with a model that assumes a fixed scale (allowing for rotation and translation for alignment), we find mask distortion recovery errors and model fit residuals ranging from 20-48 nm RMS in 10 trials. In contrast, we have an error of only 4.8 nm RMS when there is no input scale variation and a fixed-scale model is used. We conclude that using a fixed scale model eliminates the problem of misidentifying mask distortion as camera distortion; however, errors due to the true scale variation in the data can still prevent a precise distortion calibration. As a final note, scale variations at the $> 10^{-5}$ level are commonly seen in astronomical imaging systems and it would take significant additional effort to eliminate them. Some previous work Rodeghiero et al. (2019) has claimed that translation-only dithers can fully recover mask distortions, in contrast to our finding. However, these previous simulations only included uncorrelated (i.e. random) mask distortions. We simulate this case using 150 nm RMS of uncorrelated mask distortion as the input and find that we can accurately recover the input distortion to 3.8 nm (see Table 3.6.2 case 6). This matches the results of previous simulation effort. However, realistic mask distortions are unlikely to be random as any effect that flexes the pinhole mask (i.e. choice of mount, temperature) and errors in the manufacturing process will produce spatial correlations. This result emphasizes that future simulations must consider the case of spatially correlated errors in the mask distortion.

## 3.7 Discussion

Here we have measured the true deviations from the intended pattern for our pinhole mask to be 47.2 nm RMS to a precision of 4.5 nm with an additional systematic error of 10.8 nm.

Table 3.3. Simulation Results

| Case | Input $D_{Mask}$ (nm) | Input $D_{Cam}$ (nm) | $N_{rot}$ | $N_{step}$ | Translation Step size (mm) | Accuracy: $\Delta D_{Mask}$ (nm)[a] | Precision: Fit Residual (nm) | Comme |
|---|---|---|---|---|---|---|---|---|
| 1 | 150 | 858 | 12 | 2 | 0 | 108 | 5 | rotation |
| 2 | 150 | 858 | 12 | 2 | 6 | 6.5 | 3.1 | translation an |
| 3 | 150 | 858 | 1 | 3 | 3 | 142 | 0.45 | small transla |
| 4 | 150 | 858 | 1 | 6 | 3 | 142 | 0.12 | translatio |
| 5 | 150 | 858 | 1 | 6 | 6 | 142 | .09 | translatio |
| 6 | 150 (random)[b] | 858 | 1 | 3 | 3 | 3.8 | 0.8 | translatio |

Note. — $N_{rot}$ is the number of mask rotation used with them evenly spaced over 360 degrees. $N_{step}$ is the number of trans per rotation angle taken along both the x and y axis for each rotation angle. The step size is the size of each translation step
[a] Input - Output mask distortion.
[b] Ordered mask distortion is used in Simulations 1-5. Simulation 6 uses uncorrelated mask distortion as the input.

This is precise enough that it could offer significant improvement over current distortion measurements for NIRC2 Service et al. (2016). The mask pattern accuracy has important implications for the mechanical design of any distortion calibration unit, and the accuracy of this mask means it could be used a static calibration unit. Additionally, we find that when aligning each catalog with full linear transformations, the mask distortion can easily be mistaken for camera (optical) distortion due to aliasing effects. Self-consistent solutions derived from observations that only translate the mask to generate data diversity fail quite badly, with 95% of the mask distortion misidentified as camera distortion. An accurate self-consistent solution using our model for both the mask and camera distortion is only achieved when we use full rotational freedom and translations of $\sim 15\%$ of the camera field of view (Simulation 2 in Table 3.6.2). The degree of aliasing depends on the specific distortion model and is particularly sensitive to the need to fit scale changes for each measured catalog. Real optical systems generally suffer from some scale variation. For example, the lab experiment described in this paper had relative scale variations of order $10^{-5}$ between measurements and the relative error in the plate scale for NIRC2 is $2 * 10^{-5}$ Yelda et al. (2010); Service et al. (2016).

Regardless of the solution to the aliasing problem, the potential degeneracy between mask and camera distortion means that simulations of distortion calibration units must include spatially correlated mask distortion as these modes prove more challenging for the self-calibration method. It is possible that mask distortion is due to either the manufacturing of the mask or has been introduced via the mount (or both), however, these sources will also be present in realistic distortion calibration units and they influence the requirements for calibration of a given mask. Instead of self calibrating inside the instrument by moving the mask, it is possible to calibrate the mask to accurately measure the pinhole positions to avoid the systematic errors. It is worth emphasizing that the choices around mounting the mask are important as it is possible to introduce additional mask distortion by slightly deforming the pinhole mask.

Even though the intrinsic mask distortion is too large for static use in the most demanding instruments, it is still a substantial improvement for some existing distortion solutions. A distortion solution estimated with only a single position of this pinhole mask would be limited to a systematic precision of 47.2 nm, which corresponds to 23.6 $\mu$as for TMT and 130 $\mu$as for NIRC2. That offers a substantial improvement over the current distortion model for NIRC2 instrument at the W. M. Keck Observatory that has a total residual distortion of $> 1000$ $\mu$as, while a measurement using this mask imaged 1:1 would have a systematic error of 130 $\mu$as, and would allow for continued monitoring of the distortion. It is not intrinsically sufficient for the TMT requirement of 20 nm, but it is possible the pattern errors in the mask could be measured to account for the additional error. Aside from the mask distortion, the nonlinear optical distortion of the system was measured with a residual of 39 nm over an area of 1788 mm$^2$. One of the sources of this residual is optical distortion that is much higher order than our distortion model, which could be mitigated using a different model. This verifies that the approach of using a pinhole mask as an astrometric flat field has the potential to yield excellent results in the most demanding astronomical instruments, assuming that the calibration unit accounts for the mask distortion.

## 3.8 Acknowledgements

We would like to acknowledge the NFIRAOS team and NRC-Herzberg for providing the pinhole mask. This work was supported by the National Science Foundation under Grant No. 1310706. The TMT Project gratefully acknowledges the support of the TMT collaborating institutions. They are the California Institute of Technology, the University of California, the National Astronomical Observatory of Japan, the National Astronomical Observatories of China and their consortium partners, the Department of Science and Technology of India and their supported institutes, and the National Research Council of Canada. This work was supported as well by the Gordon and Betty Moore Foundation, the Canada Foundation for Innovation, the Ontario Ministry of Research and Innovation, the Natural Sciences and Engineering Research Council of Canada, the British Columbia Knowledge Development Fund, the Association of Canadian Universities for Research in Astronomy (ACURA), the Association of Universities for Research in Astronomy (AURA), the U.S. National Science Foundation, the National Institutes of Natural Sciences of Japan, and the Department of Atomic Energy of India.

## 3.9 1D Mask Distortion

Note: In the paper this section appears as an appendix. Here we use a simple 1-dimensional version of the self-calibration problem as an example of how mask distortion can be misidentified as camera distortion. This situation can be visualized as repeatedly imaging a ruler (reference positions) as it is translated over a camera. For this simulation we consider a single row of reference positions spaced every 6 $\mu$m with a total length of 90 mm and a detector that is 70 mm long with 300 nm RMS of mask distortion. To do this, we create an array of evenly spaced reference positions every 6 $\mu$m ($x_{ref}$) and apply a small deviation to each measurement as shown in equation 3.8 to generate $x'_{ref}$ which are the true reference positions.

$$x'_{ref} = x_{ref} + 3 * 10^{-9}(x_{ref} - 45)^2 \tag{3.8}$$

This set of reference positions is then translated over the camera to 10 times with a step of 2.4 mm each time to create 10 sets of simulated measured data ($x_{cam,n}$), where $n$ ranges from 0 to 9 (equation 3.9 and the top panel of figure 3.12).

$$x_{cam,n} = x'_{ref} + 2.4 * n \tag{3.9}$$

Camera distortion could be applied here as a function of the measured camera position ($x_{cam,n}$), however, we do not input any camera distortion in this simulation. An accurate model fit of this simulation will recover 0 nm of optical distortion and 300 nm of mask distortion.

We choose to fit these simulated measurements with a model that only includes camera distortion. For this purpose, we use a Cartesian polynomial up to order 4 as shown in equation 3.10.

$$x_{model,n} = x_{cam,n} + c_1 x^2_{cam,n} + c_2 x^3_{cam,n} + c_3 x^4_{cam,n} \tag{3.10}$$

Here $x_{cam}$ is the measured position on the detector, $x_{model}$ is the distortion corrected position for each of the $N$ catalogs, the $c$ coefficients are the camera distortion model. The model is fit by minimizing $\Delta$ as defined in equation 3.11

$$\Delta = \sum^{N} x_{model,n} - (a_n + b_n x_{ref}) \tag{3.11}$$

Here $x_{model,N}$ are the distortion corrected measured positions, $x_{ref}$ are a set of evenly spaced input coordinates,the $a$ and $b$ coefficients are the linear transformation parameters for each of the $N$ catalogs. These linear transformations account for the scale variation in a real system ($a_n$) and the unknown amount of translation from an imprecise stage ($b_n$). Note that this approach is comparable to a 2D self calibration problem which allows for full linear (6 parameter) transformations between each catalog. As the only input deviations are mask distortion and our model only includes camera distortion, we expect that this model should *not* precisely describe this simulated system. The second panel of Figure 3.12 demonstrates

that the camera distortion model can fit the input deviations with a fit residual of less than 0.002 % of the input distortions. This is the worst case scenario, as the errors in the reference positions have been misinterpreted as camera distortion in the system. One solution to this issue is to rotate the reference positions in order to generate greater data diversity. The other possible solution is to fix the scale in the alignment transformation. As Figure 3.13 shows, the best fit model has errors larger than 1 $\mu$m in the recovery of the translation of the reference positions ($a_n$) as well as scale errors as large as $7 * 10^{-5}$. These inaccuracies point to the another way of solving the degeneracy; if we assume that the magnification of the optical system is the same for each data and only solve for the translation offset between each catalog we accurately recover the mask and camera distortion. This is consistent with the 2D simulation results in the main text.

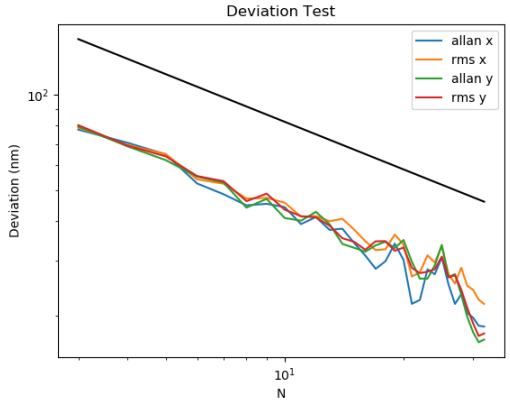


Figure 3.5 Allan deviation and RMS deviation for a sequence of 100 exposures taken at the same mask position. The black line shows the expected $N^{0.5}$ behavior. As expected, the deviations fall as $N^{-0.5}$ (black line). This behavior is only seen after a 4 parameter fit is used to reference the catalogs, due to the instability in the lab setup.

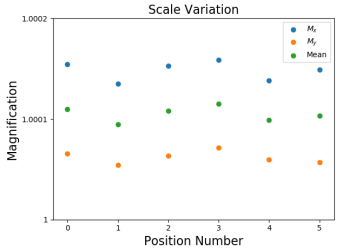


Figure 3.6 The variation in the magnification for each of the 6 positions used to measure the optical distortion of the system as summarized in Table 4.1. The linear scales $M_x$ and $M_y$ are computed as $(c_1^2 + c_2^2)^{0.5}$ where the $c$ coefficients are defined in equation 3.3. A change of 0.0005 in the scale corresponds to a $\Delta_z$ along the optical axis of 240 microns. These variations are eliminated as part of the complete distortion model, however, this means that this analysis is not sensitive to variation in these terms that is intrinsic to the mask. The dominant change is in the global scale with only small variations of the skew (ratio between $M_x$ and $M_y$).

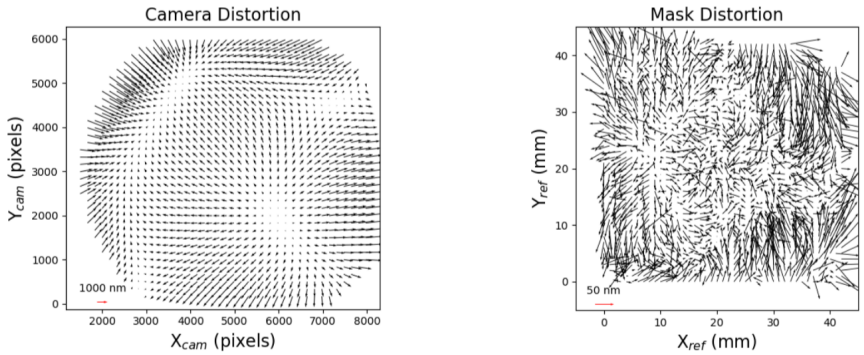


Figure 3.7 Above are the best fit models for the camera and mask distortion. The camera distortion is plotted as a function of the camera pixel (6 $\mu$m pitch) and has an RMS size of 1005 nm and 711 nm in x and y respectively. For plotting purposes, the camera distortion is sampled every 166.7 pixels (1 mm). The mask distortion is plotted in physical mask coordinates, where the pinhole pattern extends 43×43 mm and has an RMS size of 35.6 and 57.9 nm in X and Y respectively. Note that the scale of the arrows is different in the two panels and the camera distortion is ∼16× larger.

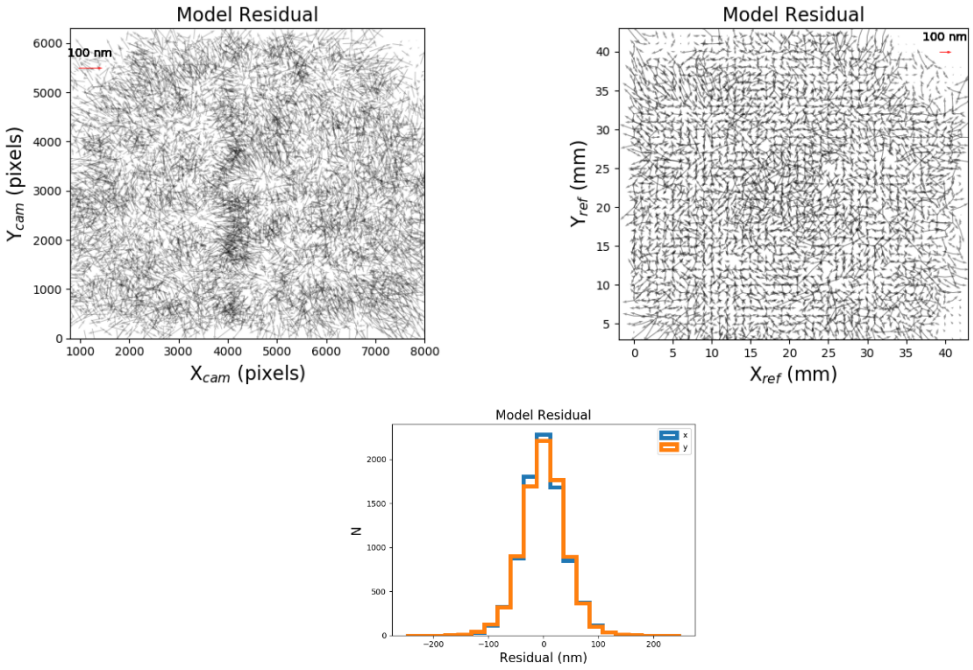


Figure 3.8 The residuals of the complete model that includes camera distortion and mask distortion. The data have been trimmed to only include pinholes measured in at least 3 of the 6 mask positions. *Left*:Residuals plotted with respect to the camera pixels. The spatially correlated residuals are due to high order distortion that cannot be fit by our distortion model.*Right*:Residuals plotted with respect to the pinhole mask. *Bottom*: Histogram of the residuals to the complete model, the RMS scatter is 39.5 nm and 38.5 nm in X and Y respectively.

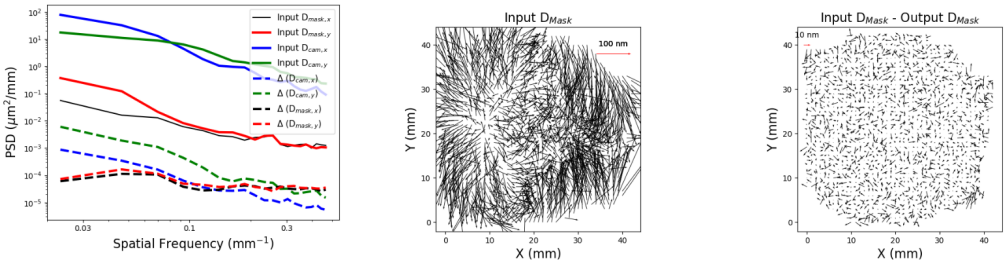


Figure 3.9 Results from the simulation where the inputs match the optical system in the lab. The best fit solutions are used as the input mask and camera distortion and the same reference mask positions are for the 6 simulated data sets. *Left*:Power spectrum distribution for the input mask distortion and the residual between the input and measured mask distortion. The $\Delta$ quantities are the difference between the input distortion and the distortion recovered by the simulation for the mask and camera distortion respectively. Both are evaluated from a square grid of points with 1 mm spacing. *Center*:Input mask distortion for these simulation, this matches the measured mask distortion measured on the lab setup with a size of 46.8 nm RMS. *Right*:Difference between the input and recovered mask distortion. This difference has an RMS size of 4.5 nm. Note that this simulation includes random measurement errors per catalog as reported in Table 4.1.

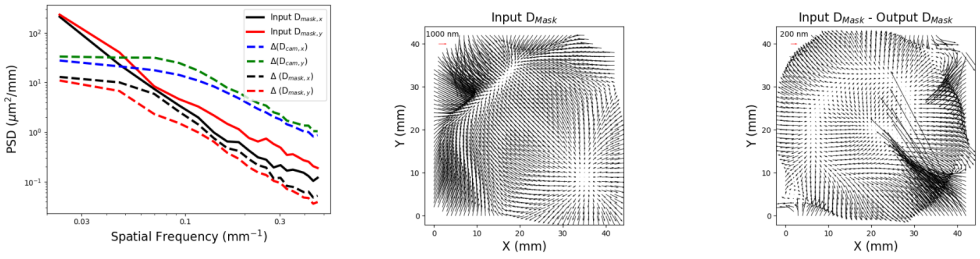


Figure 3.10 Results from the simulation of the worst case scenario where all of the deviations in the system are due to the mask distortion. The large recovery error in the mask distortion is a result of a large portion of the mask distortion being mistaken for optical distortion. The RMS size of the input mask distortion in this simulation is 858 nm, and the size of the recovery error is 198 nm RMS. We adopt that fractional error of 23% as the systematic error in the measurement of the mask distortion.

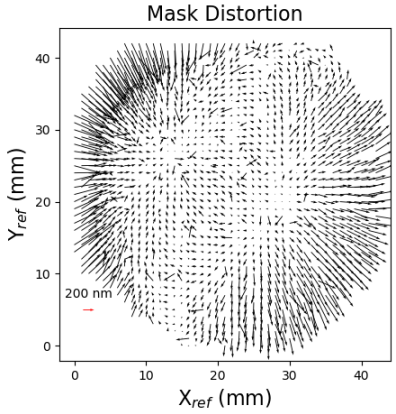


Figure 3.11 Input mask distortion for the simulations summarized in Table 3.6.2. There is a total of 150 nm RMS of deviations from a square pattern in this pattern.

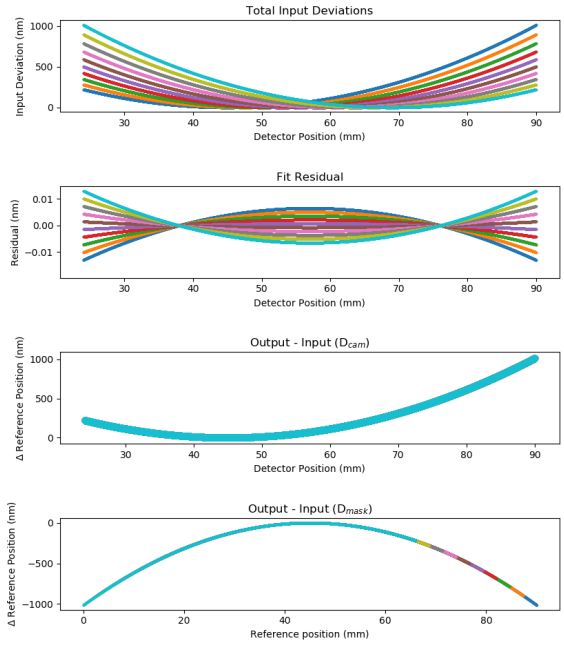


Figure 3.12 Results from a one dimensional example for the distortion self-calibration problem. Here each color corresponds to one of the 10 simulated input catalogs. The detector position is the position on the detector that a source was measured at. For this simulation, there is no input camera distortion and a quadratic term for the mask distortion. We use a model that only includes camera distortion and find that it fits the simulated data with residuals $< 0.1$ nm. This results in large recovery errors for the camera distortion (panel 3) and mask distortion (panel 4), which completely fail to accurately describe the system. This example shows how the model is degenerate, where this a quadratic mode of mask distortion can be fit as either camera distortion or mask distortion.

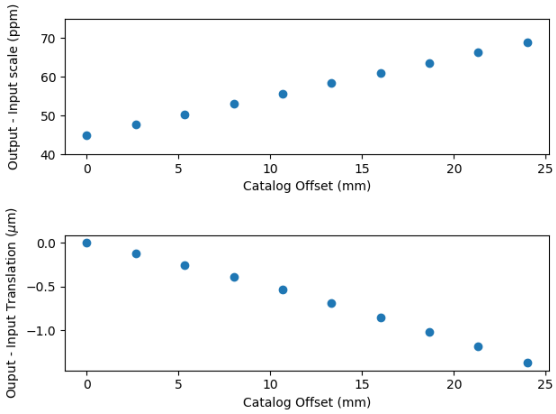


Figure 3.13 Recovery errors for the linear transformations between each catalog ($a_n$ and $b_n$ respectively). Using a fixed scale is a way to break the degeneracy between mask and camera distortion, however, this places more stringent requirements on the optical system.

# References


Anderson, J. & King, I. R. 2003, PASP, 115, 113

Best, W. M. J., Liu, M. C., Dupuy, T. J., & Magnier, E. A. 2017, ApJ, 843, L4

Brito, J. H., Angst, R., Köser, K., & Pollefeys, M. 2013, in 2013 IEEE Conference on Computer Vision and Pattern Recognition, 1368–1375

Cameron, P. B. & Kulkarni, S. R. 2007, in Bulletin of the American Astronomical Society, Vol. 39, American Astronomical Society Meeting Abstracts, 996

Diolaiti, E., Bendinelli, O., Bonaccini, D., Close, L. M., Currie, D. G., & Parmeggiani, G. 2000, StarFinder: A code for stellar field analysis, Astrophysics Source Code Library

Dupuy, T. J., Liu, M. C., Allers, K. N., Biller, B. A., Kratter, K. M., Mann, A. W., Shkolnik, E. L., Kraus, A. L., & Best, W. M. J. 2018, AJ, 156, 57

Ghez, A. M., Salim, S., Weinberg, N. N., Lu, J. R., Do, T., Dunn, J. K., Matthews, K., Morris, M. R., Yelda, S., Becklin, E. E., Kremenek, T., Milosavljevic, M., & Naiman, J. 2008, ApJ, 689, 1044

Herriot, G., Andersen, D., Atwood, J., Boyer, C., Byrnes, P., Caputa, K., Ellerbroek, B., Gilles, L., Hill, A., Ljusic, Z., Pazder, J., Rosensteiner, M., Smith, M., Spano, P., Szeto, K., Véran, J.-P., Wevers, I., Wang, L., & Wooff, R. 2014, in Proc. SPIE, Vol. 9148, Adaptive Optics Systems IV, 914810

Hosek, Jr., M. W., Lu, J. R., Anderson, J., Ghez, A. M., Morris, M. R., & Clarkson, W. I. 2015, ApJ, 813, 27

Konopacky, Q. M., Marois, C., Macintosh, B. A., Galicher, R., Barman, T. S., Metchev, S. A., & Zuckerman, B. 2016, AJ, 152, 28

Konopacky, Q. M., Thomas, S. J., Macintosh, B. A., Dillon, D., Sadakuni, N., Maire, J., Fitzgerald, M., Hinkley, S., Kalas, P., Esposito, T., Marois, C., Ingraham, P. J., Marchis, F., Perrin, M. D., Graham, J. R., Wang, J. J., De Rosa, R. J., Morzinski, K., Pueyo, L., Chilcote, J. K., Larkin, J. E., Fabrycky, D., Goodsell, S. J., Oppenheimer, B. R., Patience, J., Saddlemyer, L., & Sivaramakrishnan, A. 2014, in Proc. SPIE, Vol. 9147, Ground-based and Airborne Instrumentation for Astronomy V, 914784

Lindegren, L., Hernández, J., Bombrun, A., Klioner, S., Bastian, U., Ramos-Lerate, M., de Torres, A., Steidelmüller, H., Stephenson, C., Hobbs, D., Lammers, U., Biermann, M., Geyer, R., Hilger, T., Michalik, D., Stampa, U., McMillan, P. J., Castañeda, J., Clotet, M., Comoretto, G., Davidson, M., Fabricius, C., Gracia, G., Hambly, N. C., Hutton, A., Mora, A., Portell, J., van Leeuwen, F., Abbas, U., Abreu, A., Altmann, M., Andrei, A., Anglada, E., Balaguer-Núñez, L., Barache, C., Becciani, U., Bertone, S., Bianchi, L., Bouquillon, S., Bourda, G., Brüsemeister, T., Bucciarelli, B., Busonero, D., Buzzi, R., Cancelliere, R., Carlucci, T., Charlot, P., Cheek, N., Crosta, M., Crowley, C., de Bruijne, J., de Felice, F., Drimmel, R., Esquej, P., Fienga, A., Fraile, E., Gai, M., Garralda, N., González-Vidal, J. J., Guerra, R., Hauser, M., Hofmann, W., Holl, B., Jordan, S., Lattanzi, M. G., Lenhardt, H., Liao, S., Licata, E., Lister, T., Löffler, W., Marchant, J., Martin-Fleitas, J.-M., Messineo, R., Mignard, F., Morbidelli, R., Poggio, E., Riva, A., Rowell, N., Salguero, E., Sarasso, M., Sciacca, E., Siddiqui, H., Smart, R. L., Spagna, A., Steele, I., Taris, F., Torra, J., van Elteren, A., van Reeven, W., & Vecchiato, A. 2018, A&A, 616, A2

Lu, J. R., Ghez, A. M., Hornstein, S. D., Morris, M. R., Becklin, E. E., & Matthews, K. 2009, ApJ, 690, 1463

Maire, A.-L., Langlois, M., Dohlen, K., Lagrange, A.-M., Gratton, R., Chauvin, G., Desidera, S., Girard, J. H., Milli, J., Vigan, A., Zins, G., Delorme, P., Beuzit, J.-L., Claudi, R. U., Feldt, M., Mouillet, D., Puget, P., Turatto, M., & Wildi, F. 2016, in Proc. SPIE, Vol. 9908, Ground-based and Airborne Instrumentation for Astronomy VI, 990834

Massari, D., Dalessandro, E., Ferraro, F. R., Miocchi, P., Bellini, A., Origlia, L., Lanzoni, B., Rich, R. M., & Mucciarelli, A. 2015, ApJ, 810, 69

Massari, D., Fiorentino, G., Tolstoy, E., McConnachie, A., Stuik, R., Schreiber, L., Andersen, D., Clénet, Y., Davies, R., Gratadour, D., Kuijken, K., Navarro, R., Pott, J.-U., Rodeghiero, G., Turri, P., & Verdoes Kleijn, G. 2016, in Proc. SPIE, Vol. 9909, Adaptive Optics Systems V, 99091G

Patti, M. & Fiorentino, G. 2019, MNRAS, 485, 3470

Platais, I., Lennon, D. J., van der Marel, R. P., Bellini, A., Sabbi, E., Watkins, L. L., Sohn, S. T., Walborn, N. R., Bedin, L. R., Evans, C. J., de Mink, S. E., Sana, H., Herrero, A., Langer, N., & Crowther, P. 2018, AJ, 156, 98

Rodeghiero, G., Sawczuck, M., Pott, J.-U., Glück, M., Biancalani, E., Häberle, M., Riechert, H., Pernechele, C., Naranjo, V., Moreno-Ventas, J., Bizenberger, P., Perera, S., & Lessio, L. 2019, PASP, 131, 054503

Rodet, L., Bonnefoy, M., Durkan, S., Beust, H., Lagrange, A.-M., Schlieder, J. E., Janson, M., Grandjean, A., Chauvin, G., Messina, S., Maire, A.-L., Brandner, W., Girard, J., Delorme, P., Biller, B., Bergfors, C., Lacour, S., Feldt, M., Henning, T., Boccaletti, A., Le Bouquin, J.-B., Berger, J.-P., Monin, J.-L., Udry, S., Peretti, S., Segransan, D., Allard, F., Homeier, D., Vigan, A., Langlois, M., Hagelberg, J., Menard, F., Bazzon, A., Beuzit, J.-L., Delboulbé, A., Desidera, S., Gratton, R., Lannier, J., Ligi, R., Maurel, D., Mesa, D., Meyer, M., Pavlov, A., Ramos, J., Rigal, R., Roelfsema, R., Salter, G., Samland, M., Schmidt, T., Stadler, E., & Weber, L. 2018, A&A, 618, A23

Service, M., Lu, J. R., Campbell, R., Sitarski, B. N., Ghez, A. M., & Anderson, J. 2016, PASP, 128, 095004

Service, M., Lu, J. R., Chun, M., Suzuki, R., Schoeck, M., Atwood, J., Andersen, D., & Herriot, G. 2019, Journal of Astronomical Telescopes, Instruments, and Systems, 5, 039005

Sturm, P. 2000, IEEE Transactions on Pattern Analysis and Machine Intelligence, 22, 1199

Wertz, O., Absil, O., Gómez González, C. A., Milli, J., Girard, J. H., Mawet, D., & Pueyo, L. 2017, A&A, 598, A83

Wu, C. 2014, in 2014 IEEE Conference on Computer Vision and Pattern Recognition, 25–32

Yelda, S., Lu, J. R., Ghez, A. M., Clarkson, W., Anderson, J., Do, T., & Matthews, K. 2010, ApJ, 725, 331

# Chapter 4

# Imaka

## 4.1 Introduction

Turbulence in the Earth's atmosphere distorts the light traveling through it and degrades the image quality. These distortions can be measured and corrected n real time using Adaptive Optics (AO) systems, which measure the delivered wavefront and apply a correction using a deformable mirror. Imaka is a pathfinder instrument with the goal of demonstrating the gains from a ground layer adaptive optics (GLAO) correction specifically at Maunakea over a $11' \times 11'$ science field of view. GLAO is an advanced adaptive optics technique where the which provides a larger corrected field of view (10-100$\times$) for a reduced level of correction. This is achieved by correcting the distortions due to the turbulence close to the ground, which is common for light paths coming from a wider angle to the telescope. The major drawback of this approach is that the turbulence in the upper atmosphere creates a hard floor in the optical performance.

The degree of improvement is highly dependent on the turbulence profile at the sight in question and previous studies at Maunakea have found that the turbulence in the lowest 500 meters closest to the ground can account for $\sim 2/3$ of the power in the total atmosphere (Chun et al. 2009, 2014) Imaka is a pathfinder in two important ways, it pushes to a field of view more than twice as large as any previous systems (Baranec et al. 2009; Hart et al.

2010; Meyer et al. 2011; Tokovinin 2013; Madec et al. 2018) and demonstrates the achievable GLAO improvement at Maunakea over a statistically significant number of nights.

Imaka's design uses 3-5 natural guide stars spread over a field of view that is $18' \times 24'$ to measure the wavefront distortions due to the ground layer of the atmosphere. The ground layer turbulence is estimated by combining the signals from the wavefront sensors and correcting the common component using a deformable mirror conjugate to the pupil. The optical design optimizes the delivered image quality for the science field of view ($11' \times 11'$) while allowing a larger area for guide star acquisition and wavefront sensing (Chun et al. 2014). The design is quite different from typical narrow field AO relays, which generally utilize matched off-axis parabolic (OAP) mirrors to create a low distortion pupil and maintain the image quality. OAP relays are ideal for narrow field of view, however, for the larger field of views that Imaka required we utilized a broken Offner relay design. In a normal Offner relay, the pupil image is on the second mirror, however altering the design slightly to change the f-ratio of the beam from 13.3 to 10 also moves the pupil off of mirror. This allows for the installation of a flat deformable mirror at that location to act as the correcting element. For Imaka we re-use the CILAS bimorph mirror and electronics that was first used in the AO36 system at the Subaru Telescope. The design achieves this using a series of spherical mirrors, where the tightest tolerances on the tilt for any mirror is $\sim$1 arcminute for the two concave powered elements (Figure 4.1 Chun et al. (2016)

## 4.2 Alignment

Here I describe the general alignment procedure we used to align the mirrors in the imaka optical relay. The goal of Imaka's optical alignment is to deliver a static image quality which does not limit This is because typically the optical mounts are machined to high precision out of aluminium ($<$ 5-10 thousandths of an inch), which means that the optics all start close to their design positions along the optical axis. Most alignment approaches then have to deal primarily with correctly tilting and centering the optics as well as precisely placing

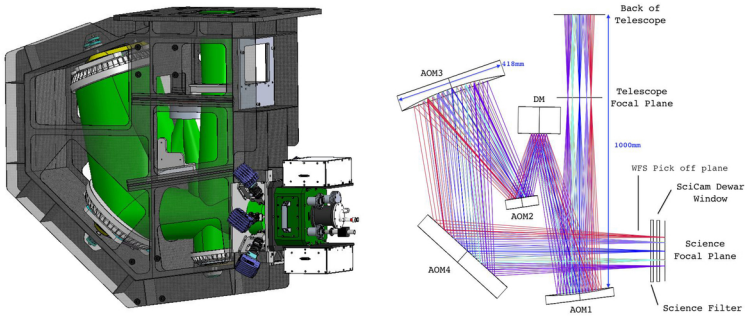


Figure 4.1 Right:3d model of the imaka optical relay. The overall structure has dimensions of 1m × 1m × 0.5m Left:Optical layout of the imaka relay, which reformats the f/10 beam from the Cassegrain focus of the telescope to an f/13.3 beam as well as allowing for the application of an AO correction. Reproduced from Chun et al. (2016).

it along the optical path. Imaka's structure is made out of a carbon fiber structure in order to make the weight budget. Our financial budget limited our options for fabrication of the carbon fiber structure, and the decision was made to utilize a lower precision methodology ($\sim$ 0.030 inches) with the idea that we would precisely measure the structure after delivery. This in turn meant that we were required to verify the actual as built location for each of the mounting surfaces prior to installation of the mirrors; In addition the mirror mounts themselves were not precise, so we also had to verify where the optical surface was with respect to the mounting legs on the mirror. Both of these problems were solved using a coordinate measuring machine (CMM) Romer arm to verify the as built dimensions, as shown in Figure 4.2. The Romer arm allows for the precision measurement of locations within its range with an accuracy of 0.11 mm. In order to entirely verify the structure we need to measure the mounting interfaces for all 4 mirrors and the surface that is mated to the output of the UH88 telescope. Unfortunately, the romer arm did not have sufficient range to simultaneously measure all of those locations, so we instead had to use two mounting points for the arm to reach all the surfaces. We then use the measurements in common to align the measurements to a common coordinate frame. The original plan for this alignment was to use 3 reference positions defined by metal tabs with conical holes which were permanently attached to the outer bulkhead of imaka which were separated by $\sim$ 750 mm. The separation

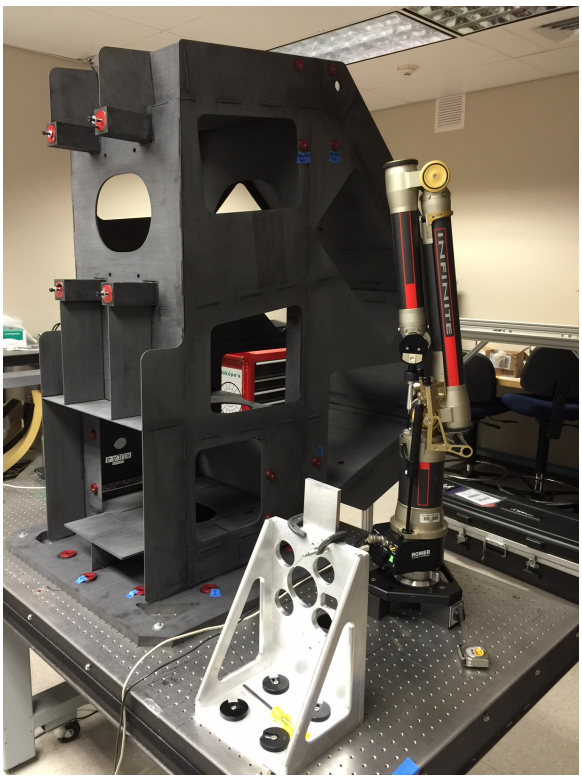


Figure 4.2 Image of the Romer arm and the imaka in one of the configurations used. Here the structure is upside down, with the input port resting flush to the table. This position of the arm and imaka allowed for measurement of optical mounts for AOM2, AOM3 and AOM4. The original approach was to use reference position that were separated by 750 mm, and one important lesson we learned is that the reference sources need a much larger baseline to limit transformation errors when combining measurements from different positions of the arm.

was too small, which means that small errors in the measurements lead to large errors in the reference frame alignment for optics which are more than 1 meter apart. To rectify this, measurements of the optical mounts for AOM2 and the DM were used to define the alignment transformation.

Due to the non-precision nature (RMS variation >200 $\mu$m) of the top of input focal plane , we fit a plane to >200 points spread over the imaka bulkhead which mounts to the telescope and used the best fit plane to define this bulkhead. We then used that surface to mate the catalog of measured position with the CAD mechanical model to compare the measured mount locations to the model mount locations for each of the mirrors. The differences were used to estimate the initial location of the mirror to place it at the correct distance along the optical axis with respect to the previous mirror. This process started with the first mirror (AOM1) and proceeded through the system from the entrance focus to the output. The final adjustment for each mirror is to fix the tilt, which is done in the following way.

We started by placing an alignment telescope at the center of the input port where light enters the system from the telescope. We centered the alignment telescope on the entrance port and then defined its location as the optical axis of the optical relay. The alignment telescope was mounted to be normal to the entrance focal plane, which then defined the alignment of the whole system. The centering of the alignment telescope on the input port was measured using the CMM, and it was within 0.05 mm of the centered on the bolt circle. One issue in the measurements is that we were unable to measure the calibration focal plane to check that it was parallel to the input port, which means we do not know for sure that our calibration unit actually matches the input beam from the telescope. Then the tilt of the mirror would be adjusted to point the beam to the center of the next optical surface using the alignment telescope to verify that the tilt was acceptable. Due to the low initial precision, the mechanical mounts for the mirrors had to be able to move by several millimeters in any direction. This requirement was fulfilled by a ball joint for each of the 3 mirror mount legs, where the tilt and translation of the mirror could be changed by

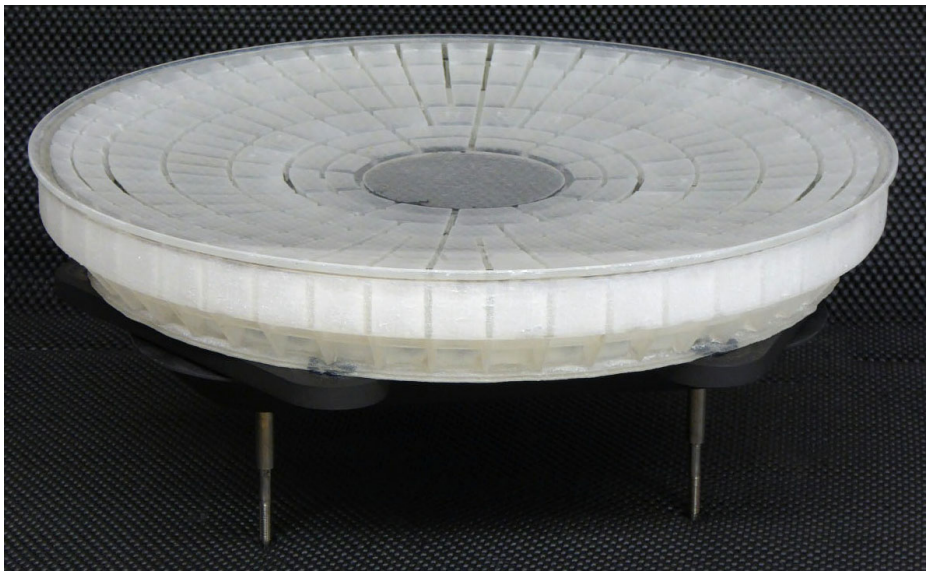

Figure 4.3 An image of AOM1 prior to coating the mirror. The honeycomb pattern seen here is due that material being removed to decrease the total mass of the mirror.

adding precision shims. These mounts can freely rotate about the three ball joints which then define the plane of the mirror. Each mount point could be moved by placing precision shims which shifts the mirror closer to the bulkhead of the instrument enclosure. It was important that the joints were all allowed to rotate when any single mount point was moved, in order to avoid excessively torquing the optics. The 3 concave mirrors are all adapted to be light weight, which is why we were concerned about applying torques to the individual mirrors (an example is shown in Figure 4.3). This process also ensured that the moves were repeatable, which decreased the number of necessary iterations to align the optic. This is a concern, as leaving the mounts in a non-relaxed state the could introduce motion on long time scales. Additionally, it was important for repeatability as the original offset estimated was based on the mirror mounts in their relaxed state. This coarse alignment had reasonably good results, and got the alignment close enough that we could do the final alignment by only adjusting the tilt of AOM3. We used this mirror for the final alignment because its tilt has the largest affect on the final image quality . This is because it is the mirror with the highest curvature and the accuracy with which we match the tilt angle of

the final mirror with respect to the other mirrors is the leading alignment term in the error budget of the final image quality.

To verify the image quality we used a small format CCD camera (Chameleon3) and a laser source in the entrance focal plane. We confirmed that the output PSF qualitatively matched the PSFs expected from the Zemax optical model, and stopped the pre-installation alignment. This comparison was done by comparing the image spots at 5 locations within 12 mm of the center of the exit focal plane and found that the imaeg size was small enough it should not be a signficant factor in the image quality compared to the atmospheric effects. This is a stage where we would have been better served by taking more careful measurements of the image quality, however, we decided on focusing on getting the instrument to the summit in lieu of further lab testing.

At this stage we made a mistake in that we did not correctly test if the output focal plane was tilted with respect to the entrance focal plane. We also attempted to test the tilt of the output focal plane. The test we did was to place a flat mirror at the output port to retro-reflect the beam through the system and then confirmed that the beam came back to the same point at the entrance focus. Unfortunately, this test will not be sensitive to a tilted focal plane, as the light beam experiences the opposite tilt on the path back through the system so the spot will come back to the same location at the front focal plane. The correct way to perform this test would have been to examine the beam footprint on intermediate optics (e.g. AOM4) for the input and retroreflected beams. The consequence of this mistake is that there was measurable image quality degradation due to tilt of the final focal plane which was measurable in the science images of stellar field, which we eventually corrected in early 2018.

### 4.2.1 Post Installation Alignment

Carbon fiber expands when it absorbs moisture, which raises an obvious concern when the alignment was performed at $\sim$ 100% humidity at sea-level in Hilo, and then 'imaka was moved to the summit of Maunakea with $\sim$ 0% humidity for use. This is only an

issue for our experiment one time, as we left the instrument at the summit after the initial installation. This humidity change corresponds to a length change in the transverse direction to the carbon fiber of $\sim 10^{-4}$ Our tests of the image quality after installation did not show obvious degradation in the delivered image and as such we did not attempt to re-align the instrument to improve the image quality. However, we did change the tilt of the final fold mirror (AOM4) to fix an observed tilt in the output focal plane. We noticed the issue in science images as a change in the focus over the field of view. To measure the actual tilt in the focal plane, we once again retro-reflected a laser source that was placed in the entrance focal plane. The test was to align the beam footprint at AOM4 such that the initial and reflected footprint matched.

## 4.3 Imaka Operations

Imaka is an imaging system with one primary goal; to demonstrate the gains from ground later adaptive optics (GLAO) in the specific context of Maunakea. We use a constellation of natural guide stars to achieve the correction, which means that for a single night we can only target a single field. From an operational point of view, this significantly simplifies some of the logistics, as we do not switch objects during a single observation. The nature of the experiment requires saving of the wavefront sensor telemetry, as we eventually need to estimate the turbulence profile for each of our images to give context to the image quality in that frame. The telemetry is contained in a memory buffer associated with the loop process, which continuously overwrites the oldest data (a circular buffer). Saving the telemetry requires writing that memory buffer out to disk, This need means that the basic requirement of the control software is to save synchronous focal plane images and AO telemetry while ensuring that the associated files are organized together. In addition, it is useful to add some flexibility to allow for various other experiments in a reasonably concise way.

The goal of the design of the python control software was to be as simple as possible while still allowing for control without requiring constant oversight. To achieve this, there is a single python object which tracks the current state of observations (e.g. how many images have been take), which has bound methods which can perform basic observations tasks which either change the loop state (e.g. gain on the controller), take and save science data, or send pointing offsets to the telescope. This approach allows for a control approach where the python observation object (called a *night* object for the rest of this text) can be instantiated in a interactive python session and then the bound methods can be called in real time to observe. For experiments that are repetitive, a separate python script can be written which takes the *night* object as an argument and loops through a sequence of commands. At the lowest level, these codes work by running commands at on a terminal which can change the AO loop state, query the loop for telemetry data and save science exposures. This modularity allows for upgrades to the science camera, where the only required interface is a new program which waits for a set amount of time, reads out the detector and writes the image to disk.

There are a couple of convenience functions built into the control code which are worth noting. Specifically, the observation object records average voltages to fix the mirror in a static shape for open loop science images. These voltages are saved by default whenever a science frame is taken with the loop gain set to be $> 0.1$ and the exposure time to be at lest 15 seconds. Recording of the average voltages also allow the measurement of the amount of tilt on the deformable mirror. When the tilt in either axis in the average voltages exceeds 1 arcsecond, that tilt is offset to the telescope. This prevents the tilt from building up and saturating the system.

Upgrades to the system would require modest changes to the currently existing code base. The most likely change would be of the science camera, so, to demonstrate the codes modularilty, I will outline how to edit the currently existing code for a new science camera. Currently, the python code takes an image by opening an ssh channel (with a non-blocking call) to the STA control computer and running a series of already compiled

programs which interface with the camera to read out the detector. These commands are hard coded in the take_im method which is bound to the Night object. Changing to a new camera setup simply requires writing equivalent programs which read out the detector and save the outputs in a fits image at a known location and then editing the prompts which point to the IP address of the STA control computer would be changed in the python control code. This has already been done once when we went from the FLI commissioning camera to the STA science camera. See the night.cam keyword, as well as logic associated with this keyword to see how this was done the first time. There is a useful help method which uses ftp to copy the new image from the camera control computer to the machine that the python commands are being run from. This code also adds extra information to the header of the science frame, and the arguments to it would have to be altered to match the new conventions if they are changed for a new camera.

## 4.4 Astrometric Precision

Here I describe tests performed to measure the astrometric accuracy of ‘imaka. These tests seek to demonstrate the current single epoch precision we achieved with ‘imaka; note that this is an important step towards demonstrating astrometry with a GLAO system at Maunakea, however, ’imaka is likely limited by factors not directly related to the GLAO correction. The astrometric accuracy of a wide field AO imaging system is a critical requirement for achieving the science goals. This is due to the fact that stellar position measurements are typically limited by systematic errors, which can be corrected for with sufficient reference sources in a given field. In general, there are more reference sources available in a larger field, which means that the accuracy limit due to number of reference sources will decrease. Additionally, there are science cases looking at stellar clusters which are many arcminutes in diameter, so wide field of view instruments are required to image the cluster in a reasonable amount of time. For this purpose there are two important considerations, the static geometric optical distortion and the time variable error sources.

In general, the variation between science images can be mitigated after the observations using low order polynomial transformation, however, a good measurement for the static distortion is necessary for comparisons to other instruments. In this section, I describe attempts to directly measure the static optical distortion of the instrument as well as some ideas for the ideal way to calibrate the optical distortion of ‘imaka in the future.

### 4.4.1 Optical Distortion using stellar images

One way to measure the optical distortion of imaka is to compare measured stellar positions to a known distortion free astrometric reference frame. In this case we use one night of imaka observations and compare the positions to the GAIA catalog positions for this field. The major advantage to using on-sky images is that we see the optical distortion from the entire system (including components due to the optics inside the telescope) and with the advent of GAIA there are high accuracy distortion free measurements available for most of the sky.

### 4.4.2 Data

The data used here is 150 30 second images observed on 05-17-2017 with the FLI back illuminated CCD (ML50100) using an I-Band filter. This is the same camera used for the experiment described in Chapter 3. This camera chip has field of view of 35 $''$ $\times$ 45$''$, however it is vignetted by the edges of the filter mount and one of the wavefront sensor pick off mirrors (Figure 4.5. The flat field is generated using 12 twilight flats observed at the beginning of the night. The master flat is produced by first subtracting darks that match the exposure time of the given flat and then normalizing each flat to have a median value if 1.0 The normalized flats are than averaged to create the maser flat, which is applied to each image prior to source extraction. The sources are extracted using *StarFinder* where the empirical PSF is defined using the brightest 45 non-saturated sources in the field (Diolaiti et al. 2000). This yields one source catalog per observed image.

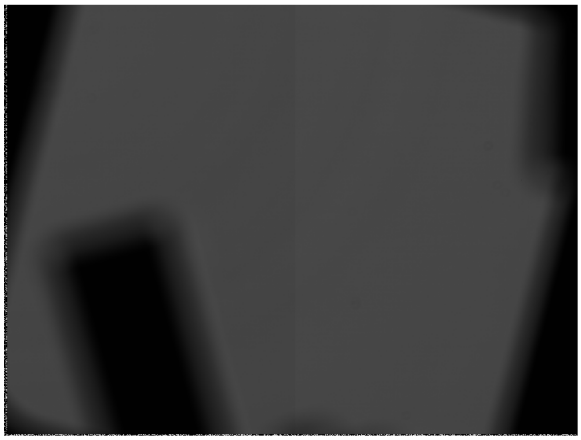

Figure 4.5 Flat field used in the reduction of the FLI images used here to measure the optical distortion. Note that the rectangular vignette in the lower left part of the field is due to a wavefront sensor pick off mirror and the vignette at the edges of the field is due to the edge of the filter. We mask all camera pixels with values $< 0.95$ in the flat field.

### 4.4.3 Internal Alignment

We first average the catalogs together to create a single master catalog before attempting to quantify the absolute optical distortion by comparing to an external frame. As part of this alignment we also need to estimate the amount of variation during the night, as the true variation in the optical distortion is important for understanding the performance of imaka. The matching for each frame is done using the same transformed coordinates from the analysis of the average coordinates. To understand the variation, it is better to simply compare the individual catalogs to the averaged coordinates. This has the advantage of avoiding errors due to residual distortion and proper motion between the GAIA coordinates and the imaka measurements. At the moment, this analysis does not include correction for the achromatic DAR. The errors in the measured positions are computed as follows. First an average of the entire night is created iteratively. The first pass uses the first frame as the reference and only removes the median translation. Then a bivariate Legendre polynomial is fit between each individual catalog and the translation corrected average. After these transformations are applied, the corrected coordinates are averaged to produce the second reference. This process is repeated one additional time to create the final measured stellar

positions ($x_{m,ave}$ and $y_{m,ave}$. We use these average coordinates in 2 ways: (1) we estimate the total amount of optical distortion by comparing them to GAIA measurements and (2) the systematic deviation in the measurements can be measured through the stack. We first present the results for the absolute distortion solution and second present the variability results.

The first issue with the matching is one that is expected in from the imaka optical design. Normally, first pass alignment is done using a 4-parameter transformation (scale, rotation, translation), however, the imaka design has a ∼8% difference in the x and y magnifications, which in turn means that a full linear transformation is necessary to match the imaka averaged coordinates to the distortion free single plate scale reference catalog. The skew terms in the distortion are large enough that the residuals in a 4 parameter transformation of the GAIA cause many mismatches. This means that the matching must be performed using 6 parameter transformations. Although I use the 6 parameter fit to find the matches, the analysis follows the "traditional" distortion measuring approach. That is, I first fit a 4 parameters (scale, rotation, x offset, y offset) to transform the GAIA positions into distortion free reference positions in the camera frame. I then fit a bivariate cubic polynomial to the differences between the measured positions and the distortion free positions as a function of the camera pixel position. For the stacked catalog, this process matches 231/239 stars with an average distortion of 33.15 pixels. The scale is 0.0867 as/pix based on the match to the GAIA, which means the RMS of the measured distortion is 2.88 as. The linear transformation gives an x magnification of 11.46 (pix/as) and a Y magnification of 11.81 (pix/as). If you instead breakdown the magnification along the RA and DEC directions gives magnifications of 10.97 (pix/as) and 11.8 (pix/as). After 3-sigma clipping the distortion solution, the new 3rd order fit has residuals of 9.5 mas in X and 5 mas in Y. Note that this analysis is negatively effected by the small dithers of the telescope during the observations, as the movement averages over the optical distortion

### 4.4.4 Variability

This analysis compares the average coordinates to each individual frame. It does so by matching each individual frame to the average, first with a search radius of 10 pixels. Then the median translations offsets are subtracted and a second matching is performed with a radius of 5 pixels. The data is trimmed as follows. First all stars with correlation values less then 0.8 are discarded from the frame. Second, all stars that are detected within 10 pixels of a vignetted region (flat $< 0.95$) are eliminated by trimming them from the averaged catalog. The last trimming step is iterative sigma clipping on the differences in the transformed coordinates as defined in the following equation.

$$x^{'} = t_{cubic}(x, y) = c_0 + c_1 x + c_2 y + c_3 x^2 + ... \tag{4.1}$$

For each individual catalog a different cubic transformation is fit that minimizes the difference between $x'$ and $x_{m,ave}$, using a linear least squares minimization. This fit is used to evaluate the variation in the linear parameters throughout the night. Specifically the scale and skew are defined separately

The average RMS deviation across all frames is gives a measure of the precision we can achieve with imaka. Figure 4.7 shows the RMS errors remaining after this final alignment. However, achieving accuracy at the 1.9 mas level requires a high quality optical distortion solution.

## 4.5 Static Pinhole Mask Experiment

As previously discussed in Chapter 4, it is possible to calibrate the optical distortion using a pinhole mask with a known pattern quality. As a demonstration of this approach we performed an experiment where installed a pinhole mask in the front focal plane of imaka. There goal of this experiment was two-fold, first to verify that the optical distortion could

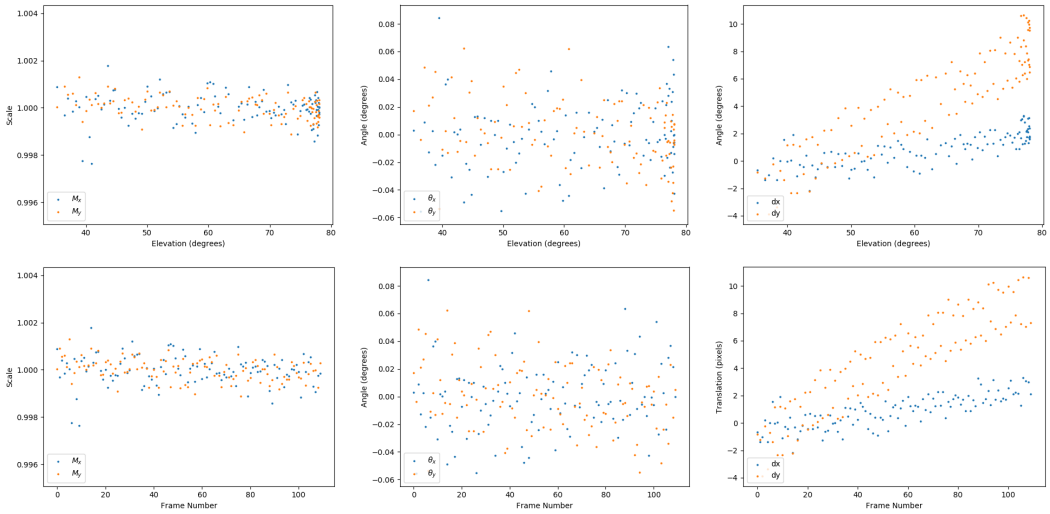


Figure 4.6 Variation in the linear transformation parameters throughout the night. These are the linear coefficients of the cubic polynomial fit between each individual frame and the reference. Here the scale are the defined as $(c_1^2 + c_1^2)^{0.5}$ for x and y respectively. For a transformation that is well described by only scale,rotation and translation the $x$ and $y$ parameters are equal in these plots.

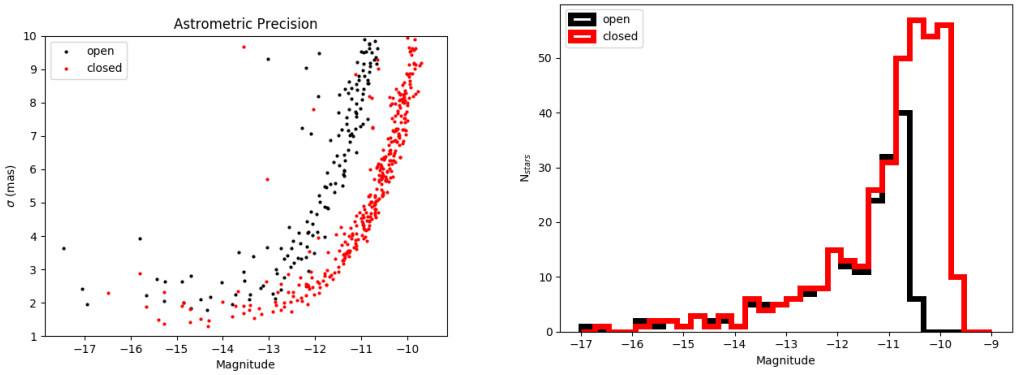


Figure 4.7 Astrometric precision and depth of the observations in this data. The median error for the bright limit ($-13$ <M< $-16$) is 1.9 mas in the closed loop data and 2.5 mas in the open loop. The improvement for stars with middling brightness ($-11$ <M< $-12$) is from 6.9 mas to 3.5 mas.

be measured using this approach on imaka and secondly to estimate the amount of deviation in the optical distortion when the telescope pointing is changed.

### 4.5.1 Experimental Setup

The mask used is the same one used as the object in Chapter 4, so we can expect that the systematic due to the manufacturing error in the pattern is $< 50$ nm. The mask tests were performed during the afternoon of May 18, 2018, with the illuminated pinhole mask installed at the entrance focal plane of imaka. We used the STA camera to image the output focal plane of imaka and held the voltages on the DM constant over the 2 hours of observations. We imaged the 12 micron pinholes which were placed on a 43 $\times$ 43 square pattern with 1 mm spacing. We did not use a shutter on the camera and the detector has 9 $\mu$m pixels with a plate scale of 0.06 as/pixel The first step after installation was to tilt the pinhole mask mount to optimize the image quality at the output focus. Then 30 60 second exposures were taken with the telescope at zenith. This longer dataset is used to estimate the stability of the setup and the random measurement errors. In addition to the zenith dataset, 4 images were taken at $\pm$ 1 hour angles. In total, these observations took two hours from freezing the loop to the final image of the pinhole mask. Its worth noting that even though we use the same mask, it is not in the same mount. As the mount rests in a different way, it is likely that the static component is not the same as the lab setup so we do not attempt to apply a correction based on measured mask deviation from that experiment.

### 4.5.2 Source Extraction and Stability

Before source extraction we subtract an average dark frame derived from the average of 10 exposures with the illumination to the mask turned off. In addition we apply the flat field correction derived from twilight flats the previous night. Source catalogs are extracted from each images using StarFinder (Diolaiti et al. 2000) where the psf model is derived using all the peaks that are between pixel coordinates of 5500 and 7500 in X and 4000 to

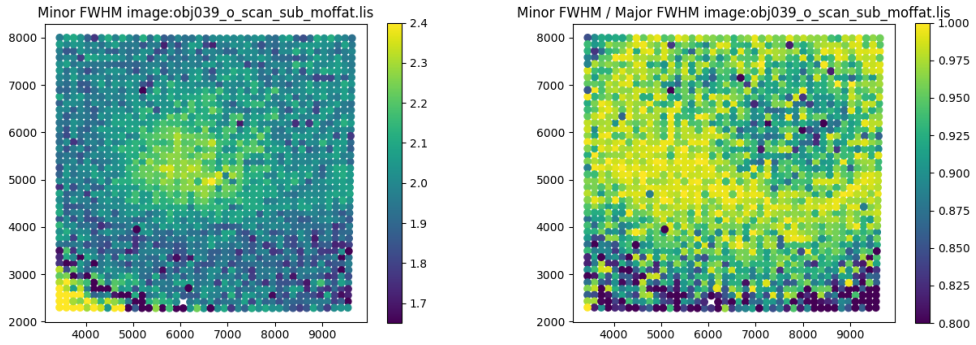


Figure 4.8 Example of the image quality from one image taken at zenith. The FWHM is measured using a 2D Moffat profile fit. The quality is consistent through the stack of data.

6500 in Y. There are a total of 1849 pinholes detected in each frame, which covers $\sim 1/3$ of the field of view of the camera. In general the distortion increases at the edges of the field of view, so area sampled was chosen to be offset towards the North East corner of the camera in order to better sample a high distortion area. Figure 4.8 shows the typical image quality variation over the field. The variation in image size is expected as the pinhole mask was not curved to match the curvature of the focal plane. The next step is to average the catalogs together, which is done using a full linear transformation to match the catalogs to the first catalog. For the zenith data set, the average RMS scatter in these positions is 141 nm for X and 200 nm for Y. For the stack of 30 images the median error on the mean is 25 nm in X and 36 nm in Y, assuming that the scatter is due to random errors. The total scatter values show substantial improvement when a full linear polynomial is used instead of a four parameter fit, which suggests that there is some variation in the ratio between the two scale terms. We will reserve discussion of possible sources for that error until later in this chapter. Additionally, the deviation versus the number of measurements averages at least decreases for the y axis, although less steeply then expected. It is noteworthy that the Allan deviation in X is much smaller for small numbers of measurements, which suggests that there is some source of systematic error varying on minute time scales (Figure 4.9). Allan deviation is a pairwise difference as compared to the RMS difference, where only the difference between points adjacent in time are included. This metric is useful as it is

insensitive to slow changing systematic errors. Note that the polynomial coefficients shown in Figure 4.9 use the following equations:

$$x_n = a_0 + a_1 x + a_2 y \tag{4.2}$$

$$y_n = b_0 + b_1 y + b_2 x \tag{4.3}$$

Here $x$ and $y$ are the original measured coordinates from the catalog, and $x_n$ and $y_n$ are the new transformed coordinates. The alignment here is two pass, for the first pass we use the measured coordinates from catalog 15 as the reference for fitting the $a$ and $b$ coefficients. For the second pass we use the average coordinates as the reference and derive the best fit linear parameters.

### 4.5.3 Distortion Measurement

Even given the large errors indicated in the averaging of the stack,we can still measure the distortion from the averaged positions.To do so, a perfect square grid of reference positions are generated with a spacing of 148 pixels and rotation angle of 0 degrees. These reference positions are matched to the measured positions, and a single 4th order Legendre polynomial is fit to explain the measured deviations. The deviations have RMS values of 7 pixels (.42 as) in X and 12 pixels (0.72 as) in Y. Its worth noting that these sizes are much larger than the measurement errors, which means this measurement of the distortion is quite statistically significant. This fit is done twice, with a single round of 3.5 $\sigma$ clipping on the model residuals in X and Y. The $\sigma$ used for this clipping is iteratively computed with 5 iterations of clipping, and all points that fall outside of the accepted range in either X or Y are eliminated from the fit. For the zenith position data, the RMS scatter in the residuals is 181 nm in X and 114 nm in Y. Figure 4.10 show that there is significant patterning in the residuals, which is currently unexplained.

We repeat the procedure above for the observations taken with the telescope pointed at $\pm$ 1 hour in right ascension. The resulting differences in the distortion solution are $< 2\ \sigma$

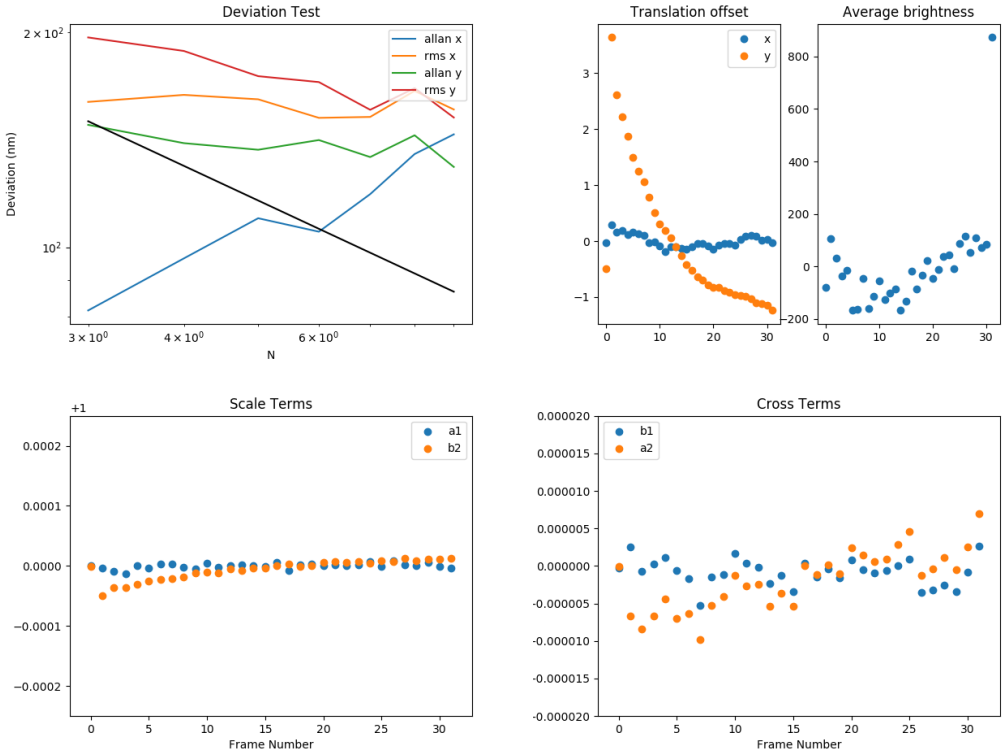


Figure 4.9 *Top*:Plot of the the Allan and RMS variance versus the number of measurements used in the average for the 30 images taken with the telescope at zenith. The behavior of the X allan variance is most puzzling, as it suggests there is systematic errors causing images separated on longer time scales to have much larger variation. Left: The average change in the positions and flux are shown plotted against the frame number with the average value subtracted. There appears to be a large trend in the Y positions, which was most likely caused by actual motion of the mask at the ∼50 micron level.. This is the second pass averaging, so the first frame is actually the first pass average. *Bottom*: Linear terms for the polynomial transformations of each frame number. The clearest trend is in the Y scale.

Table 4.1. Differences in Distortion Models

| Telescope Positions | X RMS (nm)$r_{2700}$ | Y RMS (nm) | X RMS (nm)$r_{2300}$ | Y RMS (nm) | X Model Res | Y Model R |
|---|---|---|---|---|---|---|
| Zenith - -1 hour | 65 | 120 | 38 | 111 | 110 | 108 |
| Zenith - +1 hour | 65 | 138 | 51 | 121 | 109 | 127 |
| -1 hour - +1 hour | 103 | 143 | 76 | 127 | 110 | 126 |

different from each other, where sigma is the size of the model residual (Table 4.1). This puts an upper limit on the amount of distortion variation, and means that we need a more accurate calibration unit to estimate the changes in distortion due to the repointing the telescope.

### 4.5.4 Conclusions

This experiment estimated the optical distortion over a $5.25' \times 5.25'$ with an accuracy of 181 nm. This does not meet the desired goal of knowing the distortion to better than 1 milli-arcsecond (141 nm), however, it does suggest that that goal is achievable with small improvements to the approach. This experiment utilized a static mask with only a coarse tip/tilt and focus alignment to get the object into the entrance focal plane. Additionally, the stability analysis suggests that the mount was not entirely stable.

This crude test demonstrated a few things. Firstly, it is possible to measure the optical distortion with an accuracy consistent with the measurement errors. There are factors this test does not address, such as the fact that the telescope focal plane is curved, while this mask is not, which means that there is focus variation in the output image. Additionally, there is strong evidence for additional noise due to a more subtle detector effect as shown in Figure 4.10, which would need to be addressed before this approach could be successful with this approach.

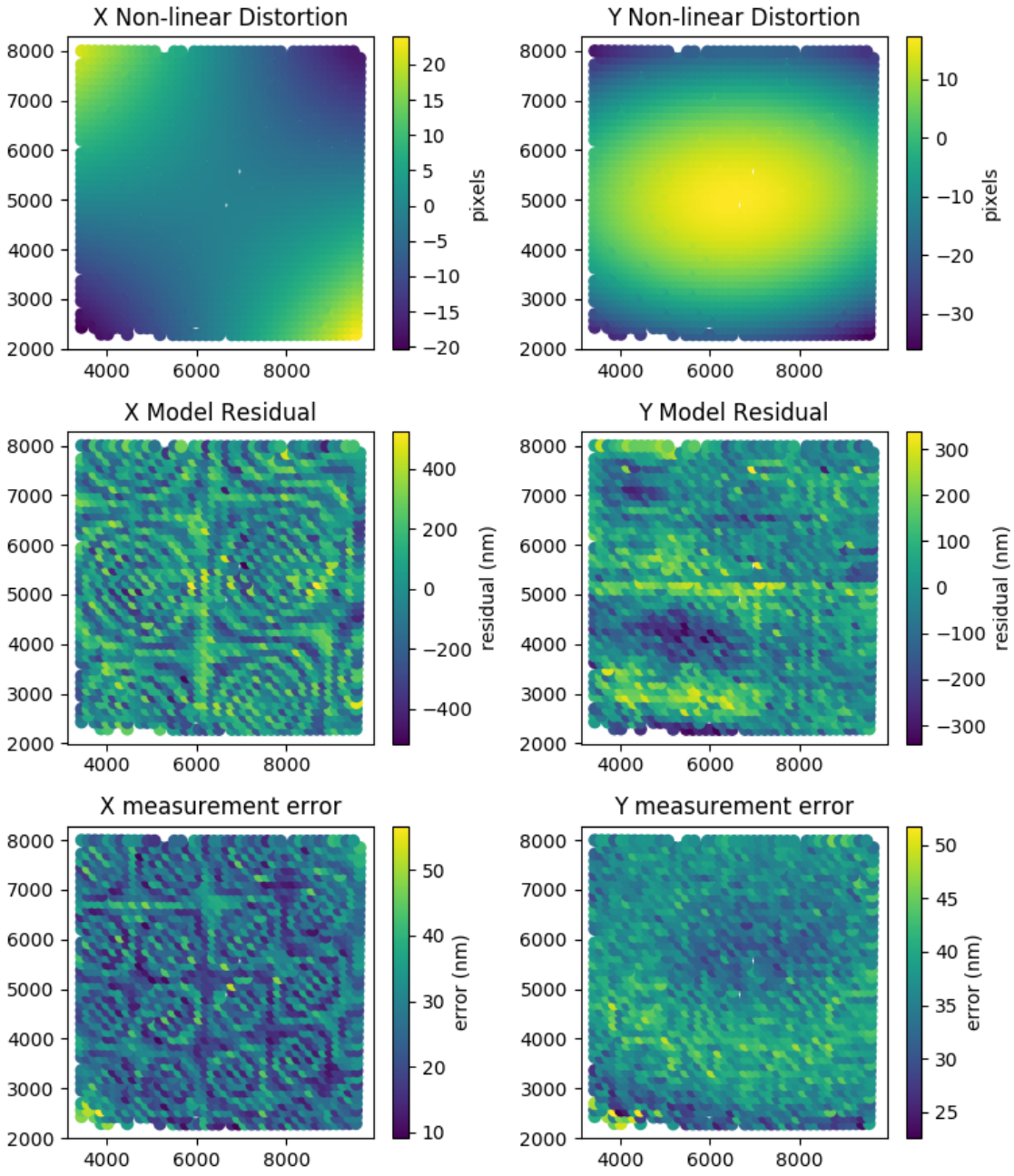


Figure 4.10 *Top*:Measured deviations from a perfect square grid as a function of the measured positions at the zenith position, based on the $4^{th}$ order Legendre Polynomial fit. The linear terms are removed in this plot. *Center*:Residuals to the distortion model plotted against the measured pixel location where each pixel of the STA detector is 9 $\mu$m. The source of the circular residuals is unknown, it could be due to high spatial frequency defects in the detector or on one of the other optics. *Bottom*:Measured errors on the mean from the stacked positions. There is a clear circular pattern in the x axis, which does not seem to obviously match to the residuals in the fit.

# References


Baranec, C., Hart, M., Milton, N. M., Stalcup, T., Powell, K., Snyder, M., Vaitheeswaran, V., McCarthy, D., & Kulesa, C. 2009, ApJ, 693, 1814

Chun, M., Wilson, R., Avila, R., Butterley, T., Aviles, J.-L., Wier, D., & Benigni, S. 2009, MNRAS, 394, 1121

Chun, M. R., Lai, O., Toomey, D., Lu, J. R., Baranec, C., Thibault, S., Brousseau, D., Zhang, H., Hayano, Y., & Oya, S. 2014, in Society of Photo-Optical Instrumentation Engineers (SPIE) Conference Series, Vol. 9148, Proc. SPIE, 91481K

Chun, M. R., Lai, O., Toomey, D., Lu, J. R., Service, M., Baranec, C., Thibault, S., Brousseau, D., Hayano, Y., Oya, S., Santi, S., Kingery, C., Loss, K., Gardiner, J., & Steele, B. 2016, in Society of Photo-Optical Instrumentation Engineers (SPIE) Conference Series, Vol. 9909, Proc. SPIE, 990902

Diolaiti, E., Bendinelli, O., Bonaccini, D., Close, L. M., Currie, D. G., & Parmeggiani, G. 2000, StarFinder: A code for stellar field analysis, Astrophysics Source Code Library

Hart, M., Milton, N. M., Baranec, C., Powell, K., Stalcup, T., McCarthy, D., Kulesa, C., & Bendek, E. 2010, Nature, 466, 727

Madec, P. Y., Arsenault, R., Kuntschner, H., Kolb, J., Pirard, J. F., Paufique, J., La Penna, P., Hackenberg, W., Vernet, E., Suárez Valles, M., & Hubin, N. 2018, in Society of Photo-Optical Instrumentation Engineers (SPIE) Conference Series, Vol. 10703, Proc. SPIE, 1070302

Meyer, E., Kürster, M., Arcidiacono, C., Ragazzoni, R., & Rix, H. W. 2011, A&A, 532, A16

Tokovinin, A. 2013, in Proceedings of the Third AO4ELT Conference, ed. S. Esposito & L. Fini, 12